Sulfur-rich polymer/porous carbon composite as a stable Li–S battery cathode

Zur Erlangung des akademischen Grades eines

DOKTORS DER NATURWISSENSCHAFTEN

(Dr. rer. nat.)

von der KIT-Fakultät für Chemie und Biowissenschaften
des Karlsruher Instituts für Technologie (KIT)

genehmigte

DISSERTATION

von

M. Sc. Bijian Deng

aus Hebei, China

KIT-Dekan: Prof. Dr. Martin Bastmeyer

Referent: Prof. Dr. Helmut Ehrenberg

Korreferent: Prof. Dr. Patrick Théato

Tag der mündlichen Prüfung: 11. 12. 2024

Abstract

Lithium–Sulfur (Li–S) batteries have gained significant attention as promising next-generation rechargeable batteries owing to their high theoretical capacity and low cost. During the discharge process of a Li–S battery, elemental sulfur (S) reacts with lithium to form lithium sulfide (Li_2S). Nevertheless, this reaction does not occur in a single step but rather involves a multistep process, during which lithium polysulfides (LiPS) are generated. These intermediates are highly soluble in ether-based electrolytes, leading to a "shuttle effect" that degrades the cycling performance. To improve cycling stability, this thesis focuses on preparing a sulfur-rich polymer/porous carbon composite as the cathode material for Li–S batteries. Specifically, a hollow porous carbon (HPC) with a rich internal pore structure was synthesized as a micro-reactor to process the inverse vulcanization between S and 1,3-diisopropenylbenzene (DIB). This unique design enables simultaneous copolymerization and distribution of S-DIB. By copolymerizing sulfur with DIB and sterically confining it in the HPC, the resulting S-DIB@HPC cathode exhibited stable cycling performance, maintaining 75% capacity at 1 C over 500 cycles. The redox pathway of S-DIB in the carbon matrix was also investigated using various spectroscopic methods.

High-resolution imaging results are helpful to understand complex redox processes in Li–S batteries which is key to unlocking their full potential. However, the ordinary secondary electron detector in scanning electron microscope (SEM) is inadequate for low-conductivity materials like S/Li_2S. In this work, the energy-selective backscatter (EsB) detector in SEM was employed to visually analyze sulfur distribution in the electrode. This technique was proved can differentiate intermediates during the sulfur redox process, further clarifying the redox pathway. Additionally, this technique was used to investigate the loss of active sulfur material in the electrode during cycling and the structural collapse of the cathode. Moreover, a relationship between electrochemical impedance and cathode structure degradation during cycling could also be established.

The efficient conversion of LiPS to Li_2S is crucial to mitigate the shuttle effect and improve the sulfur utilization. Therefore, the prepared HPC was modified with functionalized pyrenes through non-destructive π-π adsorption. The introduced functionalized pyrene was shown to further

accelerate the kinetic conversion of LiPS to Li_2S, as evidenced by electrochemical and *operando* XRD results. Benefiting from these modifications, the S-DIB@pyrene-modified HPC composite demonstrated higher initial capacity and better rate capacities compared to S-DIB@HPC. The superior confinement of the shuttle effect by functionalized pyrene was confirmed using EsB techniques.

Zusammenfassung

Lithium-Schwefel-Batterien (Li–S) haben aufgrund ihrer hohen theoretischen Kapazität sowie niedriger Kosten große Aufmerksamkeit als vielversprechende wiederaufladbare Batterien der nächsten Generation erfahren. Während des Entladeprozesses einer Li-S-Batterie reagiert elementarer Schwefel (S) mit Lithium zu Lithiumsulfid (Li_2S). Diese Reaktion erfolgt jedoch nicht in einem einzigen Schritt, sondern in einem mehrstufigen Prozess, bei dem Lithiumpolysulfide (LiPS) entstehen. Diese Zwischenprodukte sind in etherbasierten Elektrolyten sehr gut löslich, was zu einem „Shuttle-Effekt“ führt, der die Zyklenleistung beeinträchtigt. Um die Zyklenstabilität zu verbessern, beschäftigt sich diese Arbeit mit der Herstellung eines schwefelreichen Polymer/porösen Kohlenstoffkomposits als Kathodenmaterial für Li-S-Batterien. Kern der Arbeit war die Synthese eines hohlen, porösen Kohlenstoffes (HPC), welcher durch seine erhöhte innere Porenstruktur die inverse Vulkanisation zwischen Schwefel (S) und 1,3-Diisopropenylbenzol (DIB) ermöglicht. Die erhaltene S-DIB@HPC-Kathode wies eine verbesserte Zyklenstabilität auf, unter Aufrechterhaltung einer Kapazität von 75 % bei 1 C über 500 Zyklen. Verschiedene spektroskopische und mikroskopische Methoden wurden zur Untersuchung der Redoxreaktionen von S-DIB an der Kohlenstoffmatrix eingesetzt.

Hochauflösende Bildgebungsergebnisse sind hilfreich, um komplexe Redoxprozesse in Li-S-Batterien zu verstehen, was für die Erschließung ihres vollen Potenzials von entscheidender Bedeutung ist. Der gewöhnliche Sekundärelektronendetektor im Rasterelektronenmikroskop (REM) ist jedoch für Materialien mit geringer Leitfähigkeit wie S/Li_2S ungeeignet. Aufgrund ihrer nichtleitenden Eigenschaften wird zur visuellen Bestimmung der Verteilung von Schwefel und Lithiumsulfid in der Elektrode ein energiedispersive Rückstreudetektor in der Rasterelektronenmikroskopie eingesetzt. Der energiedispersive Rückstreudetektor ermöglicht die Unterscheidung von verschiedenen Zwischenprodukten der Schwefel-Redoxreaktionen, was zu einem tieferem Verständnis der Redox-Prozesse beigetragen hat. Des weiteren konnte sowohl der Verlust von aktivem Schwefelmaterial in der Elektrode während des Zyklisierens, als auch der Verlust von Struktureigenschaften der Kathode beobachtet werden. Ebenfalls konnte eine Beziehung zwischen elektrochemischer Impedanz und fortschreitendem Abbau der

Kathodenstruktur während des Zyklisierens hergestellt werden.

Die effiziente Umwandlung von LiPS in Li_2S ist entscheidend, um den Shuttle-Effekt zu mildern und den Anteil des elektochemisch aktiven Schwefels zu verbessern. Das synthetisierte HPC wurde durch eine nicht-destruktive π-π-Adsorption mit funktionalisierten Pyrenen modifiziert. Mithilfe von elektrochemischen sowie *in operando* XRD- Messungen konnte gezeigt werden, dass das eingeführte, funktionaliserte Pyren die kinetische Umwandlung der Lithiumpolysulfide zu Li_2S beschleunigt. Ebenfalls zeigte sich für das S-DIB/pyrenmodifizierte HPC-Komposit eine höhere Anfangskapazität, sowie eine erhöhte Ratenkapazität im Vergleich zu S-DIB@HPC. Eine verbesserte Unterdrückung der Shuttle-Effekte durch die funktionalisierten Pyrene konnten durch den EsB-Detektor beobachtet werden.

Contents

List of Abbreviations and Symbols

Technique

BSE	Back-scattered electrons
CV	Cyclic voltammetry
DOD	Depth of discharge
DSC	Differential scanning calorimetry
EDX	Energy-dispersive X-ray spectroscopy
EIS	Electrochemical impedance spectroscopy
EsB	Energy selective Backscattered
GCPL	Galvanostatic cycling with potential limitation
GITT	Galvanostatic intermittent titration technique
LiBs	Lithium-ion batteries
LiSBs	Lithium-sulfur batteries
NMR	Nuclear magnetic resonance
OCV	Open circuit voltage
SEM	Scanning electron microscopy
SE	Secondary electrons
SOC	State of charge
TEM	Transmission electron microscopy
TGA	Thermogravimetric analysis
UV-VIS	Ultraviolet–visible spectroscopy
XPS	X-ray photoelectron spectroscopy
XRD	X-ray diffraction

Elements and compounds

DME	1,2-dimethoxyethane
DMSO	Dimethyl sulfoxide
DOL	1,3-dioxolane

DIB	1,3-Diisopropenylbenzene
EZIF-8	Etched zeolitic imidazolate frameworks-8
HOPG	Highly oriented pyrolytic graphite
HPC	Hollow porous carbon
Li	Lithium
LiPS	Lithium polysulfides
Li_2S	Lithium sulfide
Li_2S_2	Lithium disulfide
S	Sulfur
S-DIB	Polymerized sulfur with 1,3-Diisopropenylbenzene
S_B^0	Bridging sulfur
S_T^{-1}	Terminal sulfur
py	Pyrene
MoFs	Metal-organic frameworks
ZIF-8	Zeolitic imidazolate frameworks-8

List of Figures

1 Fundamentals of Lithium−Sulfur (Li−S) batteries

1.1 Prospects for Li−S batteries

Lithium-ion batteries (LiBs) have played a crucial role in advancing various applications, particularly in communication equipment and electric vehicles. However, the growing demand for larger storage grids and longer-range electric vehicles necessitates the development of new secondary batteries. Li−S batteries, with their higher theoretical specific capacity and energy density, emerge as a promising candidate for the next-generation high-performance energy storage systems. In particular, the theoretical specific capacity of Li−S batteries can reach up to 1675 mAh g^{-1}, which is significantly higher than that of LiBs (approximately 200−300 mAh g^{-1}). The theoretical energy density of Li−S batteries also has the potential to reach an impressive 2600 Wh kg^{-1}, which is as much as ten times the current energy density of LiBs.[1, 2] In addition, sulfur is abundant and environmentally friendly. The advancement of Li−S batteries is expected to significantly enhance energy density, thereby accelerating the development and adoption of clean energy solutions.

1.2 Operating principles of Li−S batteries

In a conventional Li−S battery, sulfur acts as the cathode and lithium metal acts directly as the anode. The electrolyte used in Li−S system typically consists of lithium salts dissolved in mixed ether/ester organic solvents, allowing the flow of electrical charge between the two terminals. Unlike the intercalation of Li^+ into layered graphite in LiBs, the enhanced capacity in Li−S batteries relies on a Li conversion reaction with S, which can be expressed as:

$$S_8 + 16\ Li \leftrightharpoons 8\ Li_2S \tag{1-1}$$

As illustrated in **Figure 1-1**, during the discharge process, Li metal at the negative electrode releases electrons to form Li^+ ions, while sulfur at the positive electrode undergoes reduction with migrated Li^+ to produce Li_2S. Conversely, during the charging process, Li_2S at the positive electrode is oxidized to elemental sulfur, and Li^+ at the negative electrode gain electrons, resulting in the reduction of lithium.[3, 4] However, the redox reaction from S to Li_2S is not a one-step reaction rather involves multiple steps.[5-7]

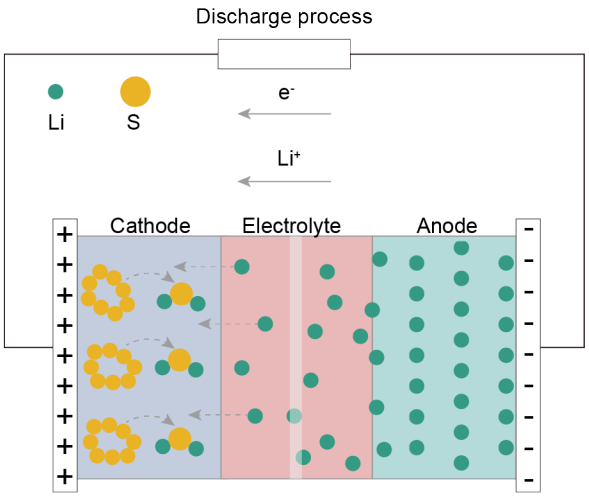

Figure 1-1 Schematic working principle of Li–S batteries, a discharge process is depicted.

According to the voltage plateau of the discharge curve shown in **Figure 1-2**, the discharge process of Li–S batteries can be divided into three stages. Initially, at the voltage plateau of 2.4 V–2.3 V, solid sulfur with a ring structure reacts with Li^+ to form long chain lithium polysulfides (LiPS), specifically, Li_2S_8:

$$S_8 + 2\,Li^+ + 2\,e^- \leftrightharpoons Li_2S_8 \qquad (1\text{-}2)$$

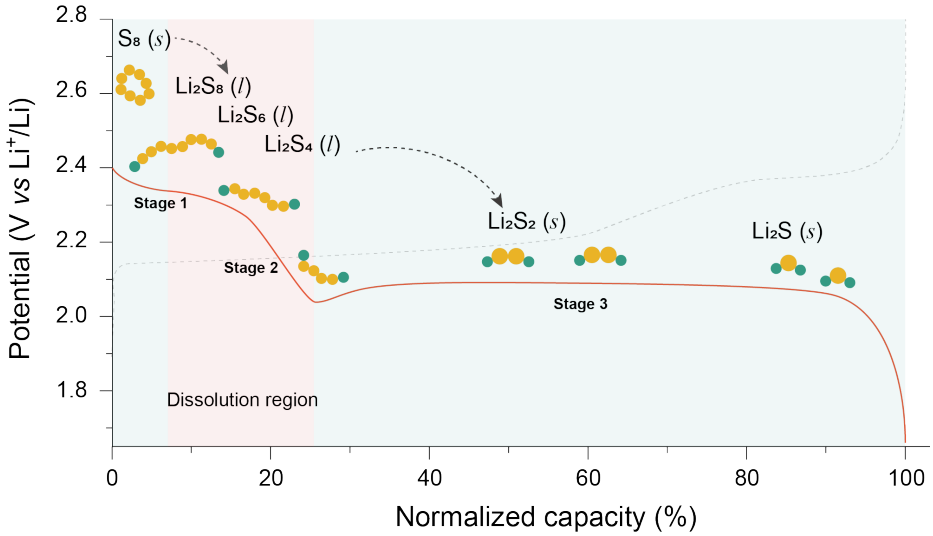

Figure 1-2 A typical discharge curve of Li–S batteries along with the reduced species at each stage.

In the second stage, Li_2S_8 is further reduced to Li_2S_6 and Li_2S_4, with the combined first and second stages contributing a quarter of the overall reaction with 0.5 electron transfer per sulfur atom.

$$3Li_2S_8 + 2\,Li^+ + 2\,e^- \leftrightharpoons 4\,Li_2S_6 \qquad (1\text{-}3)$$

$$3Li_2S_6 + 2\ Li^+ + 2\ e^- \leftrightharpoons\ 4\ Li_2S_4 \quad (1\text{-}4)$$

As the reduction process continues and the voltage declines to approximately 2.1 V, the medium-chain LiPS are reduced to short-chain LiPS and eventually Li_2S. In the third step, a theoretical transfer of 1.5 electrons per sulfur atom is proposed, which accounts for 75% of the overall theoretical specific capacity.[8, 9]

$$Li_2S_4 + 2\ Li^+ + 2\ e^- \leftrightharpoons\ 2\ Li_2S_2 \quad (1\text{-}5)$$

$$Li_2S_4 + 6\ Li^+ + 6\ e^- \leftrightharpoons\ 4\ Li_2S \quad (1\text{-}6)$$

$$Li_2S_2 + 2\ Li^+ + 2\ e^- \leftrightharpoons\ 2\ Li_2S \quad (1\text{-}7)$$

During the charging process, the Li_2S formed during discharge is first converted to LiPS at a voltage plateau of 2.2 V to 2.4 V, then ultimately converted to S at a voltage plateau of 2.4 V to 2.7 V. The operation of Li−S batteries hinges on the successful completion of each reaction step. It should be noted that LiPS as the intermediates that facilitate the conversion between the insoluble sulfur and Li_2S are soluble in conventional ether-based electrolytes.[10, 11] This indicates that the S redox process is also accompanied by solid-liquid-solid phase transitions. The three steps of reactions correspond to the phase transition reactions of solid-liquid, liquid-liquid, and liquid-solid, respectively.[12] Additionally, a solid single-phase conversion from Li_2S_2 to Li_2S occurs in the third stage.[13] Given the intricate mechanisms at operation, a comprehensive understanding of the multi-step phase transitions and reaction kinetics of redox processes in Li−S batteries remains elusive.

1.3 Challenges in Li−S batteries

Despite the typical solid-liquid-solid conversion in Li−S batteries providing high electrochemical storage performance, yet it also presents considerable challenges simultaneously. The main challenges including the inconductivity of sulfur and Li_2S, the shuttle effect and the sluggish kinetics of the phase transition, are discussed in this section.

1.3.1 Inconductivity of S and Li_2S

The electronic conductivities of sulfur and Li_2S at room temperature are only $5 * 10^{-30}$ S cm^{-1} and $3.6 * 10^{-7}$ S cm^{-1}, respectively, making them naturally typical electronic insulators.[14, 15] The

insulating characteristics of sulfur and Li_2S undoubtedly restrict electron transfer during cell operation. This impedes electrochemical reactions and intensifies polarization, particularly during discharge and charge at higher currents. The poor conductivity of sulfur and Li_2S also most likely lead to an incomplete utilization of the active material, resulting in a large difference between the actual capacity and the theoretical capacity.[14, 15] To date, no Li−S battery has been reported to achieve its theoretical capacity in the initial cycle. The poor conductivity of sulfur and the soon-to-be-discussed shuttle effect are the main reasons for this.

1.3.2 Shuttle effect and unexpected side reactions

As previously stated, the intermediates Li_2S_x ($4 \leq x \leq 8$), which facilitate the double electron transfer reaction, possess high solubility in ether-base electrolytes during battery operation. These unstable LiPS intermediates are susceptible to disproportionation reactions, leading to the formation of shorter chain LiPS and elemental sulfur, which can subsequently be redeposited on the cathode side. More critically, driven by the forces of the concentration gradient and the electric field, the dissolved LiPS in the electrolyte will diffuse through the separator to the lithium negative anode and react with it forming Li_2S_2 and Li_2S on its surface (**Figure 1-3**). The deposited Li_2S_2/Li_2S results in a reduction of the electrical conductivity and induces passivation of the lithium metal.

$$Li_2S_m + 2\ Li^+ \leftrightharpoons Li_2S + Li_2S_{m-1} \quad (1\text{-}8)$$

$$Li_2S_m + 2\ Li^+ \leftrightharpoons Li_2S_2 + Li_2S_{m-2} \quad (1\text{-}9)$$

During the charging process, the generated LiPS diffuse back to the sulfur cathode and undergoes oxidation to form long-chain LiPS. This phenomenon, characterized by the soluble LiPS shuttling between the cathode and anode during the charge and discharge cycles, is defined as “shuttle effect”.[16, 17] The continuous shuttle effect results in a continual depletion of the active material sulfur, constant corrosion of lithium metal and a decrease of coulombic efficiency throughout the cycling process. To date, this remains the largest and most insurmountable problem in Li−S batteries and other sulfur-based electrochemical batteries.

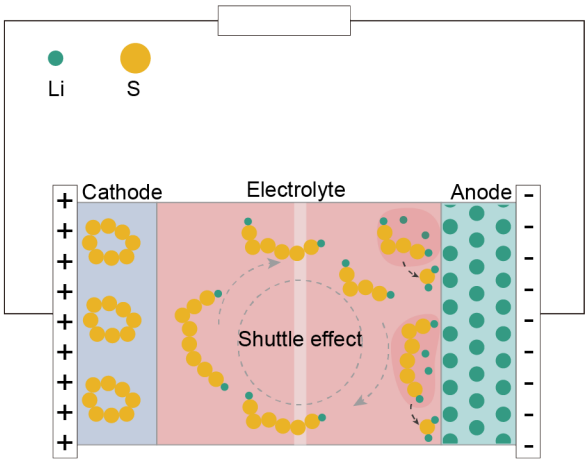

Figure 1-3 The scheme of shuttle effect happened during the operation of Li−S batteries.

1.3.3 Sluggish phase transition kinetics

The sluggish phase transition during discharge and charge process cannot be ignored. This is particularly the case regarding the liquid-solid transition process, which accounts for 3/4 of the total capacity (reaction 1-5 and 1-6). The sluggish kinetics of this process can result in the accumulation of soluble LiPS in the electrolyte, exacerbating shuttle effects. Furthermore, the increased concentration of LiPS also increases the viscosity of the electrolyte, thereby slowing the transportation of Li^+.[18] Simultaneously, LiPS often causes irregular deposition of Li_2S on the lithium metal's surface. This can lead to the formation of large solid particles, which are challenging to reuse during future charging and discharging cycles, ultimately leading to a swift decline in capacity.[19, 20] In addition, the conversion between the solid phases is also very contact limited, resulting in the product of the discharge being a mixture of Li_2S_2 and Li_2S rather than pure Li_2S.[21] This also leads to the capacity not reaching the theoretical capacity.

1.3.4 Volume expansion

Owing to the substantial difference in density between elemental sulfur and the final discharge product Li_2S, specifically 2 and 1.7 g cm^{-3} respectively, the sulfur cathode experiences a significant volume expansion (approximately 80%) before and after discharge process.[22] A volume change of approximately 50% also occurs in the lithium metal anode. Repeated volume changes during cycling lead to disruption of the cathode structure, loss of effective contact between the active material and the conductive carbon, and difficulty in sustaining the stable electrochemical reaction and eventual

battery failure. This ultimately leads to the deterioration of the battery and its eventual failure.[23, 24]

1.4 Conventional physical processing of elemental sulfur for sulfur cathodes

To address the challenges in Li−S batteries and thereby improve their practical energy density and cycle life, researchers have proposed various solutions in terms of the sulfur cathode, lithium metal, electrolyte development and separator modification.[25-30] These strategies mainly focus on improving the electrode conductivity, mitigating the shuttle effect, promoting the phase conversion kinetic and protecting the lithium anode. As this thesis work focused on the sulfur cathode, a brief review of recent design strategies for sulfur cathodes is provided herewith.

1.4.1 Melting diffusion process

At the molecular level, α-sulfur is composed of eight-membered rings of sulfur atoms arranged in a crown-like conformation, known as cyclooctasulfur. As the temperature increases, the viscosity of sulfur significantly decreases, reaching as low as 0.01 Pa·s at T = 159 ℃.[31] Taking the thermal behavior of sulfur, the most common physical methods for synthesizing sulfur composites are the melt diffusion process. In this process, a mixture of solid sulfur and the host material is heated to about 155 ℃ to facilitate the diffusion of sulfur into the host matrix, resulting in the preparation of composites with uniform sulfur distribution. Porous carbon, due to its porosity and large specific surface area, is able to effectively accommodate sulfur. The carbon scaffolds in sulfur/carbon composite system with good electronic conductivity and mechanical stability not only boost active material's effective utilization but also mitigate the shuttle effect via physisorption.

This physically confined strategy was first reported by Nazar et al. in 2009, as is shown in **Figure 1-4**.[32] In particular, mesoporous carbon CMK-3 was combined with an appropriate quantity of sulfur and subsequently heated at 155 °C. The obtained CMK-3/S exhibited an initial capacity of 1005 mAh g^{-1} at a current density of 168 mA g^{-1}, with a coulombic efficiency of 99.94%, significantly higher than that obtained by direct mechanical mixing of CMK-3 with sulfur. Nazar's group for the first time, demonstrated that using highly ordered mesoporous carbon can significantly improve the capacity and cycling stability of Li−S batteries by physically confining the active sulfur.

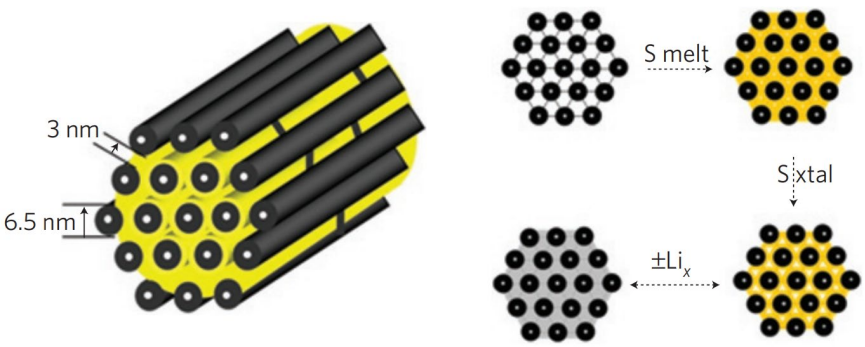

Figure 1-4 Pore structure of mesoporous carbon, CMK-3 and the schematic diagram of composite synthesis by impregnation of molten sulfur. Adapted from [32].

Following this, various carbon materials with porous morphology, including microporous carbon,[33] mesoporous carbon,[34-36] and hierarchically porous carbon[37-39] were used as sulfur hosts to achieve high capacity and stable cycling performance in Li−S batteries. For instance, Stefan Kaskel's group reported a hierarchical porous carbon, whose pore size can be adjusted by ZnO template size and reach from 20nm to 200nm.[37] When this novel carbon was used as a host for sulfur, the prepared sulfur cathode can achieve a high capacity of 1246 mAh g^{-1} with a high sulfur loading of > 3 mg cm^{-2}. In addition to the porous carbon materials mentioned above, a series of carbon materials such as carbon nanotubes,[40-42] graphene, [43-45] conductive carbon black[46] and carbon nanofibres,[47, 48] and composite carbon materials[49-52] are also widely used as sulfur host materials.

1.4.2 Carbon materials derived from metal-organic frameworks for sulfur host

Metal-organic frameworks (MOFs), which are crystalline coordination compounds composed of metal ions and organic ligands, have been widely used in various research fields due to their unique porous and functional structures.[53] Recent studies have demonstrated that carbon materials derived MOFs as precursors can inherit the distinctive structural characteristics of MOFs, including a large specific surface area and a unique and regular pore structure. The synthesis of carbon materials from MOFs is mainly reliant on the high-temperature pyrolysis of MOFs. During carbonization, organic molecules are converted into porous graphitic carbon matrix and metal molecules can be converted into metal nanoparticles, metal compound nanoparticles or doped with atomic metals in carbon materials. Metal-free carbon materials can be obtained from MOFs by using low boiling point metals or by purification after pyrolysis. [54, 55] Additionally, the composition and morphology of the resulting carbon products can be readily modified by selecting appropriate MOF precursors. In this

regard, MOFs based hollow porous carbon materials have become an excellent choice to accommodate sulfur because of their potential to trap LiPS in Li−S batteries. Pan's group has reported a porous carbon nanocage with nitrogen doping and uniform dispersed cobalt catalyst as a host structure for sulfur.[56] It was shown that the fabricated host structure has high conductivity, effective stress relief, as well as good contact at the interface between sulfur and carbon. Therefore, it enables a long cycle life (86% capacity retention over 500 cycles), and high capacity of 600 mAh g^{-1} at a high current density of 7.5 A g^{-1} for Li−S batteries.

LiPS have a polar molecular structure and therefore purely non-polar carbon materials can only physically adsorb LiPS due to the weak interaction between polar and non-polar molecules. It has been demonstrated that doping carbon materials with heteroatoms can enhance the polarity of non-polar carbon materials at the interface, thereby improving the electrical conductivity and reaction kinetics and facilitating the physiosorbed of LiPS. Andrey L. Rogach and co-workers synthesized a novel N, S doped porous carbon host with 3D tubular holes through calcinating Zn-based MOF with 2,5-thiophenedicarboxylic acid and 1,4-bis(pyrid-4-yl) benzene as ligands.[57] During carbonization, sulfur powder was introduced upstream of an Ar flow and converted to S_6, S_4 and S_2 and dispersed on the carbon surface. S and N dopants were verified that they increased the polarity of the carbon host to restrict diffusion of sulfur thus making the obtained carbon/sulfur composite achieve a stable cycling performance. In recent years, different metals,[58, 59] transition metal oxides[60, 61] and metal phosphides[62, 63] have been introduced into highly conductive carbon skeletons obtained by calcining MOF for sulfur host materials to study their adsorption and catalysis of LiPS. Nevertheless, the catalytic effect non-metals on sulfur redox-kinetics remains insufficiently explored.

1.5 Chemical processing of elemental sulfur for sulfur cathodes

1.5.1 Inverse vulcanization

Although these carbon/sulfur composites have shown superior electrochemical performance during initial charge/discharge cycles, their performance tends to decline rapidly in subsequent cycles because physical confinement alone is insufficient to overcome the LiPS shuttle problem. This prompted another important strategy of chemical confinements by synthesizing sulfur-rich polymer through inverse vulcanization. [64, 65]

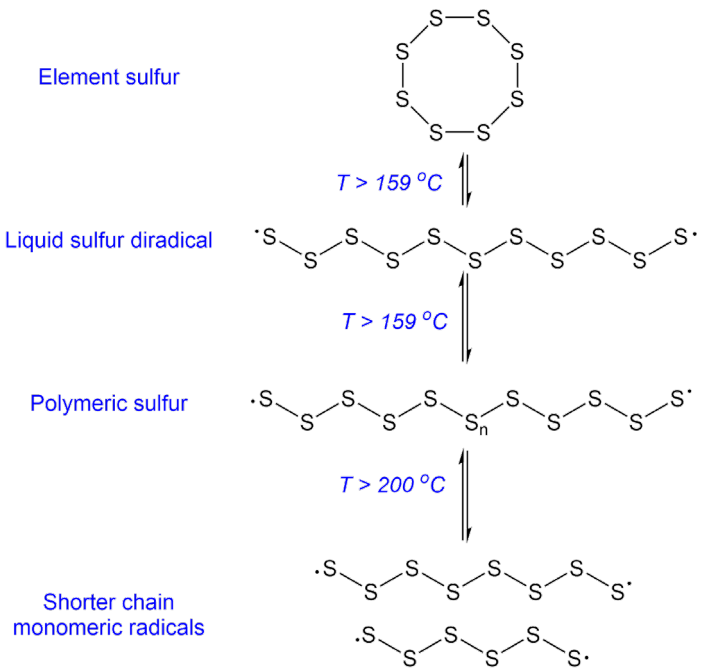

Figure 1-5 Structure transformation of elemental sulfur at various temperatures.

As is shown in **Figure 1-5**, when sulfur is heated to above 159 °C, ring-opening polymerization occurs, generating a linear polysulfane with diradical chain ends from S_8 monomer randomly.[31, 66, 67] The polysulfane is later polymerized to high molecule weight polymerized sulfur. This semi-crystalline polymerized sulfur has poor mechanical properties and is insoluble in solvents. Stabilization of the diradical polymeric sulfur can be achieved by quenching radical chain ends via copolymerization with dienes, such as dicyclopentadiene, commonly used in rubber vulcanization. With this background, Pyun and co-workers have proposed a bulk free radical copolymerization between S_8 and 1,3-diisopropylbenzene (DIB) without the usage of organic solvent.[67] The reaction known as inverse vulcanization and the scheme of which is shown in **Figure 1-6**.

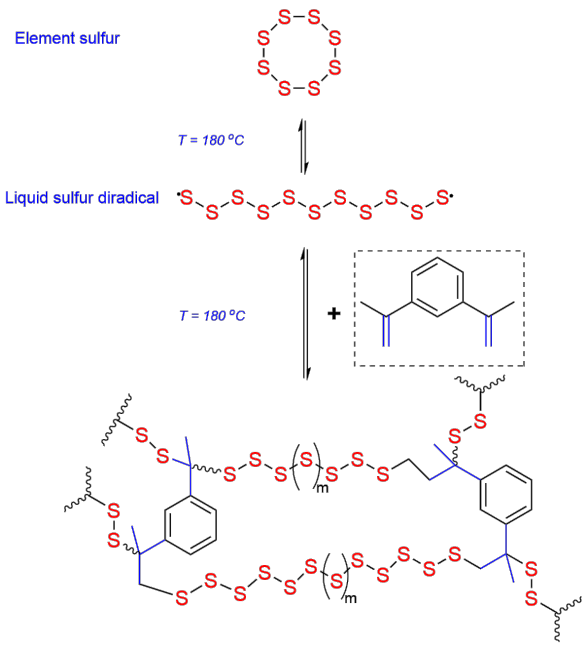

Figure 1-6 Schematic process of inverse vulcanization between sulfur and DIB. Modified from [67].

During the heating process above 159 °C, a linear polysulfane with diradical chain ends produced by S_8 can trigger a double-bond addition to DIB, extracting isopropenyl hydrogen atoms from the DIB molecule to form isopropenyl radicals. The active isopropenyl radical then reacts with the S−S bond in linear polysulfhane to form a C−S bond attached to the sulfur chain. Likewise, the reaction occurs at the other interstitial alkene bond in DIB. Repeating this process in the polymerization reaction eventually forms a cross-linked sulfur chain structure with the DIB molecule at the center.[67] It was found that the microstructure of the copolymers varies with the feed ratio of S_8 to DIB during inverse vulcanization. Incorporating DIB into the polymer sulfur creates branched sites that inhibit the reversible depolymerization process by facilitating the formation of polysulfide rings and thiol end groups. Copolymers with lower DIB content (0 to 15 wt%) exhibit semi-crystalline properties, while those with higher DIB content (20 to 65 wt%) display amorphous characteristics. Calculating the sulfur content based on molar feed ratios revealed that copolymers with DIB contents ranging from 10 to 50 wt% contained an average of 44 to 10 sulfur units per DIB unit. This highlights the significant role of DIB content in influencing the structural properties of the copolymers. When S-DIB serves as cathode and fabricated in a Li−S coin cell, it delivers an initial capacity of 1225 mAh/g with minimal capacity loss, a capacity of 1005 mAh g^{-1} after 100 cycles and 817 mAh g^{-1} after 300 cycles. Despite this decrease in capacity, the batteries maintain a coulombic efficiency of 99%.[68]

Following this inverse vulcanization reaction, a variety of monomers have been used to synthesize different sulfur-rich polymers, including unsaturated carbon bonds, sulfhydryl groups, benzoxazine, cyano groups, halogen atoms, unsaturated sulfur bonds, and epoxy groups. The sulfur content and electrochemical properties of sulfur copolymers through inverse vulcanization by S_8 with small-molecule monomers are summarized in **Table 1**. Some of these functional groups can be incorporated into an organic compound to exert synergistic effects, further increasing the sulfur content of the product. For instance, a vinyl functionalized UiO-66 was synthesized to copolymerized sulfur chains by Huang's research group.[69] They also synthesized a UiO-66/S composite through the conventional sulfur melt diffusion method as a reference to verify the advantages of chemical confinement. Systematic electrochemical experiments and in situ Raman spectroscopic analyses demonstrated that the polymerized sulfur anode exhibited a more reactive mechanism, greatly accelerating the conversion of LiPS and inhibiting the growth of lithium dendrites. These findings indicate that sulfur chains grafted through copolymerization demonstrate accelerated kinetics in charging and discharging processes compared to sulfur melt in carbon pores.

Table 1 Summary of reported sulfur copolymers through inverse vulcanization reaction and the battery performance of corresponding electrodes

Copolymerization linker	Sulfur content in copolymer (wt%)	Conductive material content (wt%) in the electrode	Initial capacity (mA h g^{-1})	Capacity (mA h g^{-1}) at high C-rate	Cycling retention (mA h g^{-1}) after X cycles at C rate	REF
1,3-diisopropenylbenzene	90	20	1225	430 at 2 C	817 after 300 cycles at 0.1 C	[68]
tetra(allyloxy)-1,4-benzoquinone	75	30	1346	833 at 10 C	791 after 500 cycles at 1 C	[70]
1,4-diphenylbutadiyne	90	--	1080	~ 400 at 2 C	400 after 850 cycles at 0.2 C	[71]
1,3-diethynylbenzene	80	80	1143	700 at 0.5 C	396 after 500 cycles at 1 C	[72]
trithiocyanuric acid	75	30	1210	730 at 5 C	945 after 100 cycles at 0.2 C	[73]
allyl-terminated poly(3-hexylthiophene-2,5-diyl)	80	25	1260	739 at 1 C	799 after 100 cycles at 0.5 C	[74]
poly(3-oligo(ethylene oxide)4-thiophene)	90	85	1132	826 at 1 C	898 after 100 cycles at 0.1 C	[75]
thiol-functionalized benzoxazine	83	30	1149	576 at 2 C	630 after 1000 cycles at 1 C	[76]
1,4-dicyanobenzene	62	30	670	400 at 2 C	482 after 300 cycles at 1 C	[77]
4-vinyl-1,2-epoxycyclohexane (VE)	50	10	1248	773 at 2 C	831 after 100 cycles at 0.5 C	[78]
vinyl trimethoxysilane	--	10	1184.3	1019 at 0.5 A g^{-1}	450 after 500 cycles at 0.5 A g^{-1}	[79]
ethylene glycol dimethacrylate and dicyclopentadiene	80	30	1206	385 at 2 C	710 after 200 cycles at 0.2 C	[80]
1-vinyl-3-allylimidazolium bromide	70	20	1108	603 at 5 C	573 after 900 cycles at 2 C	[81]
poly(*m*-aminothiophenol)	86	10	1240	600 at 5 C	495 after 1000 cycles at 2 C	[82]

1.5.2 Application for S-DIB based on its physical properties

In the pursuit of enhancing the cycling stability of S-DIB and other sulfur rich polymers in Li−S batteries, several improvement strategies have been put forth. These strategies can be broadly classified into two categories. The first category leverages the intrinsic physical characteristics of S-DIB and viscosity change during the synthesis. Techniques such as imprint lithography,[67] 3D printing,[83] and spraying[84] are employed to alter the physical appearance of the synthesized S-DIB. For example, when proposing the inverse vulcanization, Pyun and co-workers pointed out that micropatterned S-DIB films can be prepared through imprint lithography on polydimethyl-siloxane (PDMS) moulds. This was done by pouring the viscous prepolymers formed into PDMS moulds when the batch polymerization conversion of S_8 and DIB was low. The morphological results indicated that the height of the S-DIB columns could be controlled in the range of 1-5 um and the periodicities in the range of 10-20 um by using PDMS moulds with varying feature size and spatial arrangement. Shubin also reported a sulfur copolymer-graphene architectures with well-designed periodic micro lattices by means of 3D printing technique.[83] In this study, an appropriate ink comprising sulfur particles, DIB, and condensed graphene oxide dispersion was initially prepared and subsequently printed on a substrate with micro-lattices. The printed architectures were subsequently thermally treated to allow S_8 to react with DIB, during which the viscosity changing would also facilitate greater interconnectivity. The 3D-printed sulfur copolymer-graphene architecture displayed a high reversible capacity of 812.8 mA h g^{-1} and satisfactory cycle performance. Of particular significance is the potential of this straightforward 3D printing method to create intricate architectures for diverse energy storage devices.

1.5.3 Sulfur-rich polymer/carbon materials composite

The second approach is to constrain S-DIB by covalently bonding it to nanostructured conductive carbon materials. This method is becoming increasingly popular as the incorporation of carbon materials increases electrical conductivity by providing a conductive framework for the intrinsically non-conductive S-DIB. At the same time, the covalent bonding of linear sulfur chains to carbon effectively limits the detrimental dissolution of LiPS. For this purpose, Yung-Eun's group used oleylamine modified reduced graphene oxide as a conductive medium to covalently bond copolymer,

where linear sulfur was first capped with DIB (**Figure 1-7**).[85] Owing to the innovative design featuring homogeneous sulfur distribution and combined chemical and covalent confinement to LiPS, the electrode preserved 81.7% of its initial capacity following 500 cycles at 0.5 C. Their systematic electrochemical analyses further elucidated the facilitating role within each reaction regime during discharge process, particularly during the conversion of low-order LiPS to Li_2S. Similarly, vinyl group-functionalized reduced graphene oxide sheets were synthesized by Chi-Hao Chang to increase the dispersibility of polysulfur.[84] In the synthesis, the abundant terminal vinyl groups can undergo in situ diradical copolymerization with sulfur and DIB through facial inverse vulcanization. Benefiting from this interconnected structure, the enhanced electrochemical utilization, which has increased from approximately 38% to 60%, can be attributed to the existence of infinite conductive pathways throughout the sulfur polymer matrix. The reported sulfur-rich polymer/carbon composites and their electrochemical performance are summarized in **Table 2**.

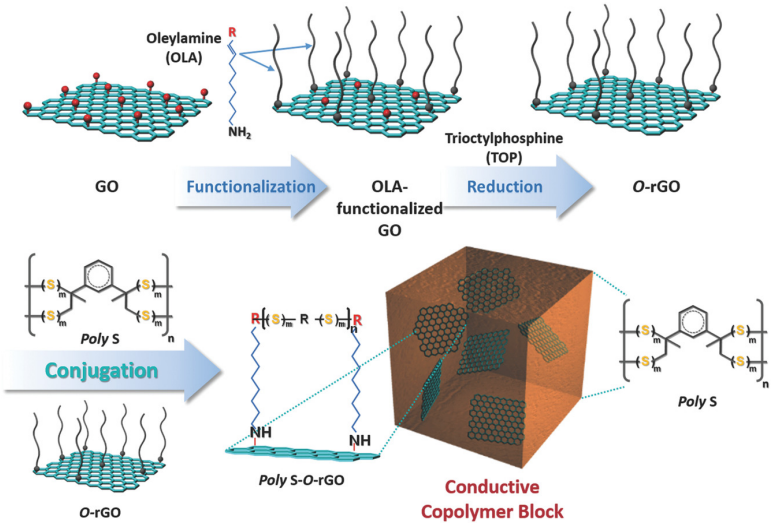

Figure 1-7 Schematic reaction from graphene oxide (GO) to the final nanocomposite (Poly S-O-rGO) where linear sulfur chains are uniformly distributed via the termination with DIB and subsequent covalent linking to oleylamine. Adapted from [85].

In summary, the carbon/sulfur composites can be prepared via a conventional sulfur melt diffusion process or by an inverse vulcanization between functionalized carbon and organic monomer so far, respectively. Both routes aim to achieve a uniform distribution of sulfur within the conductive carbon network, thereby improving sulfur utilization. Compared to the sulfur melting diffusion

process, which is typically conducted under 155 ℃ for 4 hours, the synthesis via chemical processes is relatively time-efficient. Furthermore, the presence of polymerization centers in the sulfur-rich polymer enables superior confinement of LiPS.

Table 2 Summary of reported sulfur copolymers/carbon composites and corresponding electrochemical performance

Copolymerization linker	Sulfur content in copolymer (wt%)	Conductive material content (wt%) in the electrode	Initial capacity (mA h g^{-1})	Capacity (mA h g^{-1}) at high C-rate	Cycling retention (mA h g^{-1}) after X cycles at C rate	REF
3-isopropenyl-α, α-dimethylbenzyl isocyanate afforded CNTs	76	10	1434	601 at 1 C	465 after 500 cycles at 1 C	[86]
CNTs	63.5	--	1300	700 at 2 C	647 after 450 cycles at 1 C	[87]
oleylamine (OLA)-functionalized reduced graphene oxide	80	15	1289	~ 879 at 1 C	1040 after 500 cycles at 0.5 C	[85]
vinyl functionalized MOF/CNTs composite	71.4	10	1130	748 at 3 C	609 after 1000 cycles at 1 C 960 after 100 cycles at 0.2 C	[69]
carbon sphere/limonene	75	5	1160	510 at 5 C	880 after 200 cycles at 0.5 C	[88]
sulfydryl functionalized reduced graphene oxide	75	20	1108	985 at 2 C	858 after 450 cycles at 0.5 C	[89]

1.6 Review of visualization characterization techniques for Li−S batteries

The key to fully unlocking the potential of Li−S batteries lies in a comprehensive understanding of the intricate processes that occur during the discharge and charge process. Several spectroscopic techniques have been used to determine species within the Li–S system including Raman Spectroscopy,[90-92] UV–vis Spectroscopy, [89, 93-96] X-ray Absorption Spectroscopy.[96-102] Concurrently, novel spatial imaging techniques are being developed to distinguish between sulfur, LiPS and Li_2S, while also demonstrating their spatial distribution.[7, 13, 103-109] These technologies are of great value in elucidating comprehensive reaction mechanisms and kinetics of sulfur redox processes, due to their capacity to demonstrate the spatial distribution of the products, the internal morphology of the electrodes and the structural changes. This thesis work also provides a feasible technique for characterizing the spatial distribution of sulfur and intermediates during discharging/charging process. Consequently, the subsequent section will offer a brief overview of the fundamental principles underlying the reported visualization techniques, along with a discussion of their respective outcomes.

Operando confocal Raman microscopy: The Raman technique is a powerful tool for the study of Li–S batteries due to the high Raman activity of sulfur and LiPS. Furthermore, it is convenient for carrying out operando studies. To simultaneously track, identify, and quantify sulfur and LiPS with different lengths in real time during the discharge and charge process, operando confocal Raman microscopy visualization technique was used.[7] The visualization is based on the peak position and intensity of the Raman peaks at each point in the region explored. By visualizing the potential-dependent reactants and intermediates, quantifying the changes in their intensities, the first-order reaction kinetics of sulfur reduction and LiPS redox processes were put forward. The nucleation and its later growth mechanisms of electrodeposited Li_2S was also detailed investigated.

X-ray ptychographic microscopy. X-ray absorption spectroscopy is element-specific and sensitive to the local bonding chemistry and solvent environment. This enables the electronic charge state of sulfur to be determined by means of S K-edge XAS in Li–S batteries. In light of these findings, X-ray spectroscopic ptychography was put forward as an extension of XAS, allowing the acquisition of spatially resolved absorption and phase spectra and facilitating chemical state analysis with a

resolution of better than several tens of nanometers.[106] This is one of the few systems capable of imaging the chemical state of sulfur inside bulk samples with higher spatial resolution.

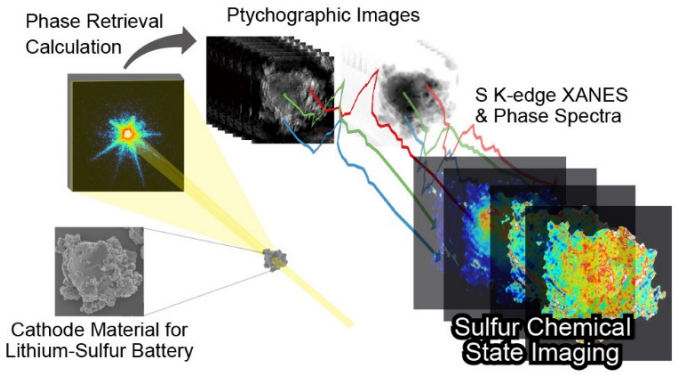

Figure 1-8 Scheme of the working principle of the X-ray spectroscopic ptychography. Adapted from [106].

Their visualization results indicated that the discharge reaction started at the surface of the sulfur particles and the sulfur inside the particles does not play much of a role because of the inconductivity of sulfur and the slow electronic transportation. A comparison of the distribution of the sulfur chemical state in electrodes before and after the discharge and charging processes reveals that LiPS is dissolved from the active material into the electrolyte. In contrast, sulfur oxides accumulate in the voids between the particles of the active material.

Electrochemical transmission electron microscopy: The high temporal and spatial resolution of in situ transmission electron microscopy (TEM) enables the observation of dynamic reactions at the atomic and single-molecule levels. However, the sublimation of sulfur is difficult to avoid under a high-vacuum environment of the open-configuration in TEM. In response to this problem, a Li–S nanobattery within a liquid cell, and combined with electrochemical transmission electron microscopy was constructed, which was used to achieve high-resolution and real-time observation of the evolution of LiPSs at electrode surfaces in an ether-based electrolyte. The findings also indicated that active centers were responsible for the aggregation of soluble LiPSs into a droplet-like dense phase, which in turn resulted in the immediate deposition of nonequilibrium nanocrystalline/amorphous Li_2S, rather than the conventional step-by-step transformation.[13]

In summary, there are essentially two types of techniques to visualize the distribution of sulfur, Li_2S, and the intermediates during cycling. The first method strives to achieve mapping results by utilizing

spectroscopic techniques, which can identify the valence states or species of sulfur. The other method initially employs an electron microscope to capture an image, followed by identifying the objects present within the observed region. For instance, the lattices in TEM results can be utilized to distinguish different crystals. SEM, another common type of electron microscope, heavily relies on the electrical conductivity of the sample and is not extensively used for analyzing sulfur distribution. To address this limitation in visualizing all products generated during the operation of a Li–S battery through SEM, this thesis work has undertaken a series of explorations.

1.7 Outline of this thesis

Given the challenges associated with Li−S batteries and the existing contributions in this field, this dissertation presents a comprehensive series of research on the synthesis of sulfur-rich polymer/porous carbon composite cathode materials and their electrochemical behaviors. Chapter 2 opens the thesis by providing an overview of the fundamental principles of the characterization method employed in this thesis, emphasizing their specific application to Li−S batteries.

In Chapter 3, the synthesis of hollow porous carbon (HPC) with abundant hierarchical pores is achieved through the calcination of etched zeolitic imidazolate framework-8 (ZIF-8). The HPC is utilized as a reactor for the direct conduct of the inverse reaction between sulfur and DIB. As a result, the S-DIB@HPC can be synthesized in a single step, offering a potentially universal method to prepare S-rich polymer/carbon composites. The S-DIB confined within a carbon matrix exhibits superior electrochemical performance compared to the S/HPC composite prepared by the melt diffusion process. Furthermore, this chapter introduces the use of the EsB detector in SEM and establishes its parameters, for the first time, for characterizing the distribution of sulfur and Li_2S, as well as the intermediates. The combination of EsB images with *operando* Raman spectra, NMR spectra, and XPS results reveal the sulfur redox pathways that occur during the discharging and charging processes, as well as the degradation during long cycling operations.

In Chapter 4, the prepared HPC is modified by functionalized pyrene to further enhance the surface polarity. This non-destructive modification can introduce polar groups as required without altering the intrinsic properties of carbon. The effect of the introduced polar groups, especially on the

deposition of Li_2S, is explored in detail. Benefiting from polar groups, the initial capacity, rate performance, and cycling stability of the sulfur-rich polymer/carbon composite are further improved. Chapter 5 provides a brief summary and general outlook of the research and identifies issues for further exploration in the future.

2 Characterizations

This chapter outlines the fundamental working mechanisms of the characterizations used in this thesis, focusing on their specific applications in Li–S batteries while avoiding complex physical theories.

2.1 Electrochemical measurements

2.1.1 Cyclic voltammetry (CV)

In a CV test, a potential is linearly swept across the electrode at a specific scan rate, causing redox reactions at the electrode-electrolyte interface. These reactions are detected by measuring the resulting current. During the cathodic scan, as the voltage nears the reduction potential, reduction processes are triggered, consuming oxides at the electrode surface. This creates a concentration gradient that initiates diffusion, generating a cathodic current proportional to this gradient.[110] As the voltage becomes more negative and the oxide concentration decreases, the diffusion flux increases until the oxygen surface concentration is depleted, reaching its maximum flux. Each CV peak corresponds to a specific electrochemical reaction, with its intensity and shape providing insights into the kinetics of the underlying processes.

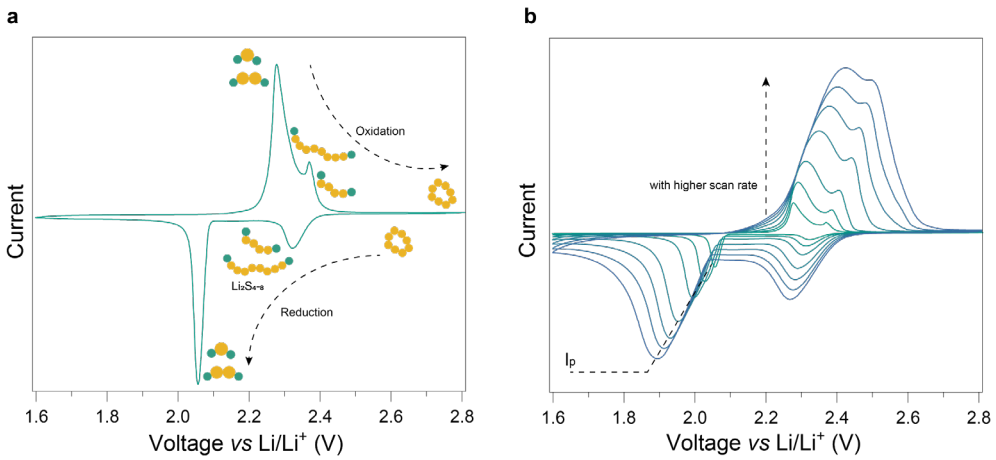

Figure 2-1 (a) The typical CV profile of a Li–S battery (b) CV profiles of a Li–S battery at different scan rates. The peaks can be found shifted low scan rate to high scan rate because of the diffusion limitation.

Figure 2-1a shows a representative CV curve for a typical Li–S battery, along with CV curves at higher scan rates in **Figure 2-1b**. The first reduction peak at 2.3 V corresponds to the reduction of

solid sulfur to soluble LiPS (Li_2S_x, $4 \leq x \leq 8$). The second reduction peak at 2.05 V is associated with the further reduction of LiPS to Li_2S_2/Li_2S. During the anodic scan, peaks may overlap between 2.2 and 2.6 V, corresponding to the oxidation of Li_2S_2/Li_2S to LiPS and elemental sulfur, indicating a different pathway from the reduction.[111] In a reversible electrochemical system, the scan rate and individual current peaks follow the Randles-Sevick equation.[112, 113]

$$I_p = 2.69\times10^5\times n^{3/2}\times A\times D_{Li}^{1/2}\times v^{1/2}\times C_{Li} \quad (2\text{-}1)$$

In the equation 2-1, I_p is the peak current, n is the number of electrons transferred in the reaction, A is the electrode area, D_{Li} is the diffusion coefficient of lithium ions, v is the scan rate, and C_{Li} is the concentration of lithium ions in the electrolyte. Based on the equation, the Li^+ diffusion coefficient can be calculated by linearly fitting the square root of the peak current to the scan rate. However, the accuracy of this equation relies on several assumptions, including the presumption that the system operates under steady-state conditions and that the electrode reactions follow simple electron transfer kinetics. Given the inherent complexity of the Li–S system, this thesis employs this equation primarily for comparing the Li^+ diffusion rates in the similar electrode structure, rather than for precise calculations.

2.1.2 Galvanostatic cycling with potential limitation (GCPL)

GCPL technology allows for the charging and discharging of batteries within a specified voltage range. This study evaluates the rate performance and long-cycling stability of the battery, along with Galvanostatic Intermittent Titration Technique (GITT) curves, using this method. Additionally, electrodes at different charging and discharging states are obtained by setting different cut-off voltages.

GITT involves applying a series of current pulses, each followed by a relaxation period with no current flow. GITT is widely used to more accurately calculate the Li^+ diffusion coefficient in LiBs. However, by-products in Li–S batteries complicate the quantification of Li^+ transport using existing GITT mathematical models. Nonetheless, the technique can still assess polarization and internal resistance during charging and discharging processes to study polarization changes related to phase transitions.[85, 114, 115] As shown in **Figure 2-2**, the polarization voltage difference between the open-

circuit voltage and the closed-circuit voltage consists of an instantaneous voltage jump due to electrical resistance and a voltage relaxation resulting from the concentration gradient.

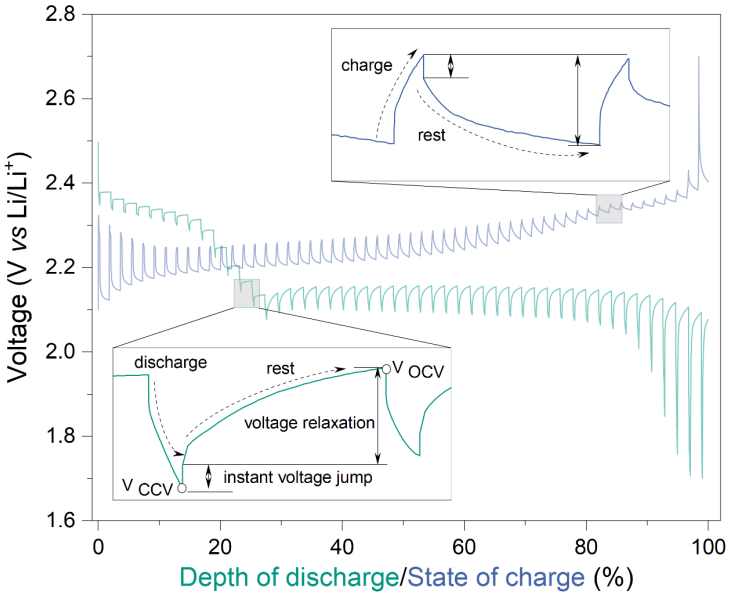

Figure 2-2 The typical GITT curve of a Li–S battery.

2.1.3 Electrochemical impedance spectroscopy (EIS)

EIS involves applying a small sinusoidal perturbation (either a voltage or current) to an electrochemical system at a steady state and measuring the response over a range of frequencies. The system's sinusoidal response (current or voltage) is monitored relative to the applied perturbation. Typically, EIS data are simulated using an equivalent circuit model, which includes components like ideal voltage sources, resistors, and capacitors to represent the behavior of a battery. This model helps in understanding the electrochemical and transport properties of the electrode/electrolyte interface, including interfacial and diffusion impedance. To enhance fitting accuracy, the impedance tests in this thesis were conducted using a three-electrode system, allowing separate analysis of the interfacial impedance for both the positive and negative electrodes.

2.2 Spectroscopy Characterizations

2.2.1 Raman spectroscopy and *operando* Raman spectroscopy

Raman spectroscopy is a non-destructive technique that relies on the scattering of monochromatic light, usually from a laser source. While most light is elastically scattered by molecular vibrations,

a small fraction is inelastically scattered, resulting in energy shifts corresponding to specific vibrational modes. This principle allows Raman spectroscopy to provide detailed information about the molecular structure, dynamics, and interactions of a sample. It is widely used to study defects and the graphite degree of carbon materials by analyzing their D and G peaks.[116, 117] Additionally, Raman spectroscopy is well-suited for examining the products and reaction pathways in Li–S redox processes, as both sulfur and LiPS exhibit high Raman activity.[7, 91, 92] However, definitive evidence for the characteristic Raman peaks of the final products, Li_2S_2 and Li_2S, is lacking. *Operando* characterization involves real-time observation of a system during operation, and Raman spectroscopy is suitable for this purpose as it uses a laser at atmospheric pressure. The *operando* cell can be adapted from a standard cell by drilling a hole in the cell case and sealing it with glass.

2.2.2 X-ray diffraction (XRD) and *operando* XRD

XRD is based on the interference of X-rays scattered by the planes of atoms in a crystal. When a beam of X-rays strikes a crystalline material, it scatters in specific directions depending on the arrangement of atoms. The relationship between the angles at which X-rays are diffracted and the distance between atomic planes in a crystal is described by Bragg's Law:

$$n \times \lambda = 2d \times \sin\theta$$

In the formula, λ is the wavelength of the X-ray, d is the distance between atomic planes in the crystal, θ is the angle of incidence at which diffraction occurs. By analyzing the peak intensity and position in the diffraction pattern, virous crystalline phases can be identified. Both the charging product sulfur and the discharging product Li_2S in a Li–S battery produce high diffraction peaks. However, liquid-phase LiPS cannot be characterized by XRD due to its complex solvation structure with the electrolyte. The *operando* XRD measurements can be used to determine sulfur depletion and Li_2S precipitation, thus studying its redox process.

2.2.3 X-ray photoelectron spectroscopy (XPS)

X-ray Photoelectron Spectroscopy (XPS) is a surface analysis technique used to determine the elemental composition and ionic states of a sample's surface. It operates by emitting X-rays of a specific energy into the sample, which excites electrons in the atom's inner layers and ejects core

electrons. The binding energy of these emitted electrons reveals information about the element's identity and the ionized atomic orbitals. Consequently, the chemical composition of the sample surface can be qualitatively analyzed. Moreover, small shifts in the binding energy can indicate the form and valence state of elements, aiding in the study of their specific valence states. Deconvolution of S 2p XPS peaks differentiates various sulfur chemical environments, enabling the identification of different sulfur-containing species generated during the discharging and charging process.[118, 119] It is also possible to distinguish terminal and bridging sulfur atoms in polysulfides and calculate the average length of LiPS chains from the intensity ratio. However, this method is only applicable to the investigation of the sulfur present on the surface and not to the study of the state of sulfur inside the carbon pores.

2.2.4 Lithium-7 nuclear magnetic resonance spectroscopy (^{7}Li NMR)

^{7}Li NMR spectroscopy is a powerful analytical technique for investigating the local environment of lithium ions in various materials. Due to the weak Raman and XRD signals of Li_2S in the electrode, NMR spectroscopy is employed in this thesis to confirm the presence and quantify the amount of Li_2S in the electrode under different charging and discharging states.

2.2.5 Thermal analysis techniques

Differential scanning calorimetry (DSC) measures the heat flow associated with phase transitions of a material as a function of temperature. This technique provides information about thermal properties such as melting points, glass transition temperatures, and crystallization. It was mainly used to assess the successful synthesis of sulfur rich polymer and its polymerization degree in this work. Thermogravimetric analysis (TGA) measures the change in mass of a material as it is heated, cooled, or held at constant temperature. It is widely used to determine the sulfur amount in the carbon/sulfur composite based on the lower boiling point (445 °C) of sulfur compared to that of carbon.

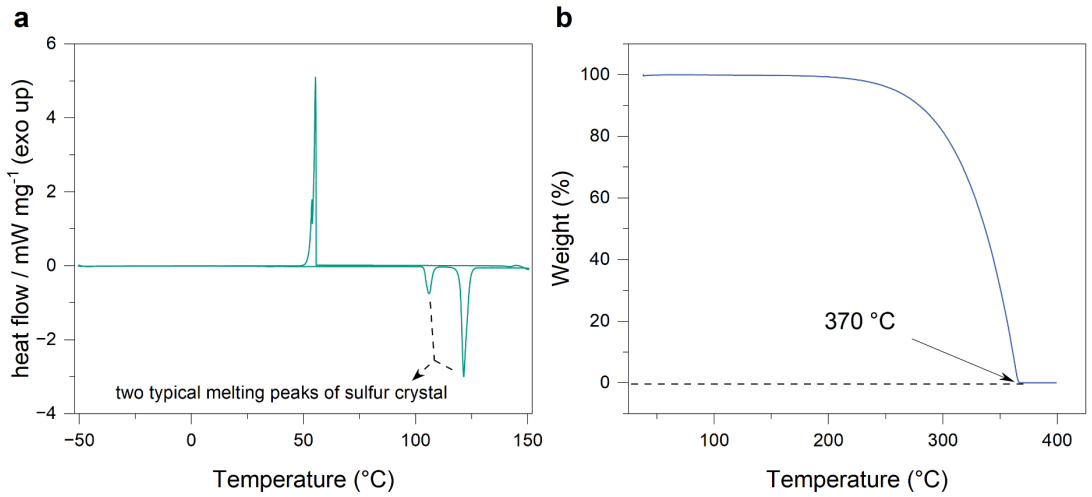

Figure 2-3 (a) The DSC curve and (b) the TGA curve of elemental sulfur.

2.2.6 Specific surface area and pore size distribution analysis

The specific surface area and pore size distribution are critical parameters for characterizing the porous structure of materials. These parameters are typically analyzed using low-temperature nitrogen adsorption techniques. During this process, the sample is exposed to nitrogen gas at the temperature of liquid nitrogen, resulting in physical adsorption on the sample's surface. At a constant temperature, the amount of gas that can adsorb onto the material's surface is dependent on the pressure. By measuring the adsorption at various relative pressures, a nitrogen adsorption isotherm is generated. The specific surface area of the sample is then calculated using the Brunauer-Emmett-Teller (BET) adsorption isotherm equation. The pore size distribution of the material can also be obtained by fitting the N_2 desorption isotherm with different equations.

2.3 Scanning electron microscopy (SEM)

The SEM is a versatile instrument for examining and analyzing microstructure, morphology, and chemical compositions. As illustrated in Figure **2-4a**, electrons are generated at the top of the electron gun column and accelerated through the column at a specified accelerating voltage. After passing through apertures and condensers, scatterer electrons are excluded, and the electron beam diameter is reduced. The objective lens, being the final lens in the column, focuses the electron beam on the sample. All processes are conducted under a high vacuum to ensure the electrons travel without scattering by air. When the electron beam interacts with the atoms in the sample, it produces various signals that provide information about the surface topography and composition, which are

then detected and imaged.

As shown in **Figure 2-4b**, secondary electrons (SE), defined as having an energy of less than 50 eV, are produced due to inelastic scattering near the specimen surface and are widely used to visualize surface texture and roughness.[120] The images obtained by the SE detector exhibit superior resolution due to the relatively small interaction volume, approximately the size of the beam diameter. The quality of the SE image depends on the number of SE that reach the detector, and thus, the conductivity of the sample significantly influences the quality of the obtained SE images.

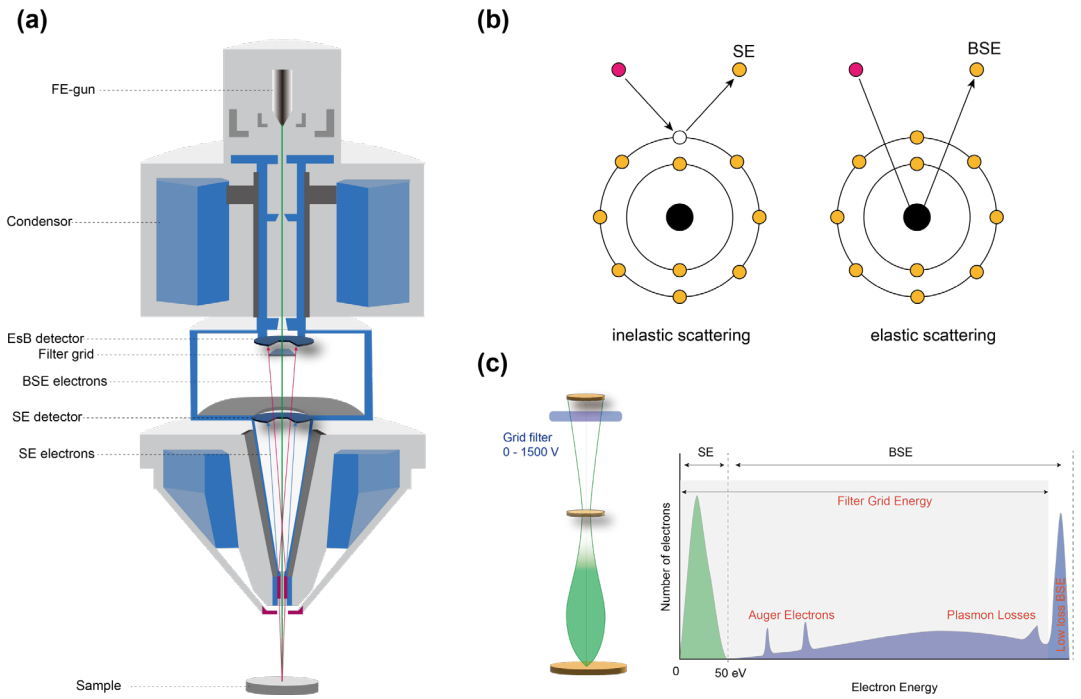

Figure 2-4 (a) The scheme of the column design of the SEM used in this work. (b) Schematic of an electron being emitted from the surface and being backscattered by the interaction with the atom nuclei. (c) The energy spectrum of SE and BSE.

Another effective method for producing an image in SEM involves the detection of backscattered electrons (BSE). BSE are electrons that have undergone either single or multiple elastic scattering events and have subsequently escaped from the surface with an energy greater than 50 eV. The number of positive charges in an element's nucleus, corresponding to its atomic number, influences the number of BSE produced: elements with higher atomic numbers backscatter more electrons, resulting in a stronger backscatter signal. [120] Accordingly, the contrast observed in BSE images offers insight into the surface composition. For classical BSE detection, electrons with high energy

(> 10k eV) penetrate deeply into materials, making this technology unsuitable for imaging nano-compositional differences. However, when the incident energy is lowered to below 5 keV, the BSE coefficient becomes nonlinear.[120, 121]

To enable BSE to reflect compositional information at low incident energy, an energy-selective backscatter (EsB) detector is introduced in the SEM. When this detector is active, the filter grid in front of it only allows BSEs greater than the grid threshold energy. **Figure 2-4c** shows the entire energy spectrum of SE and BSE profiles with increasing energy in a low range of the primary beam energy. By setting an appropriate threshold voltage, the low-loss BSE can be filtered out from the multiple inelastic electron signals and projected directly to the EsB detector. This process amplifies the signal difference of low atomic number elements and restores the contrast lost from the small backscatter coefficients at reduced primary beam electron energies.[122, 123] Consequently, for common elements in the sulfur cathode, such as carbon (acting as a host for sulfur) and sulfur itself (serving as the active material), the EsB detector can distinguish between them and effectively visualize the distribution of sulfur.

3 Sulfur Distribution Analysis in Lithium−Sulfur Cathode via Confined Inverse Vulcanization in Carbon Frameworks

3.1 Introduction

Inverse vulcanization is widely used to create sulfur-rich polymers, allowing sulfur to be modified into processable copolymers with adjustable thermomechanical properties. Chemical confinement in these polymers can more effectively inhibit the shuttle effect by covalently immobilizing sulfur species, compared to physical confinement by carbonaceous materials. To improve the electrical conductivity of the cathode with poly-S as the active material, hollow porous carbon was synthesized to act as a micro-reactor for conducting inverse vulcanization. This design enables simultaneous copolymerization and distribution of S-DIB in the carbon matrix, which is expected to physically and chemically confine LiPS, enhancing the cycling stability in Li−S batteries. Due to the lack of visualization results explaining sulfur redox pathways during de/lithiation, this chapter proposes using EsB assisted SEM technique. The EsB detector helps visualize the distribution of sulfur, Li_2S, and intermediates within the electrode's cross-section at a sub-micrometer scale. The resulting EsB images provide concrete evidence of the sulfur evolution process and offer insights into the discharging/charging mechanisms.

3.2 Synthesis and properties of HPC, S-DIB and S-DID@HPC

3.2.1 Synthesis of ZIF-8 and HPC

To synthesize ZIF-8 with a diameter of 240 nm, 9.35 g of zinc acetate dihydrate was dissolved in 100 mL of deionized water. Separately, 28 g of 2-methylimidazole was dissolved in 150 mL of deionized water. The zinc precursor solution was gradually added to the 2-methylimidazole solution. This mixture was stirred for 5 minutes and left to stand at room temperature for 24 hours. Afterward, the mixture was centrifuged and washed three times to ensure thorough purification. The resulting ZIF-8 precipitate was dried at 80 °C for 12 hours to obtain a white powder.[124] The SEM image of the synthesized ZIF-8, with a diameter of 240 nm, is shown in **Figure 3-1a**, which serves as the

precursor for the hollow porous carbon used in this study.

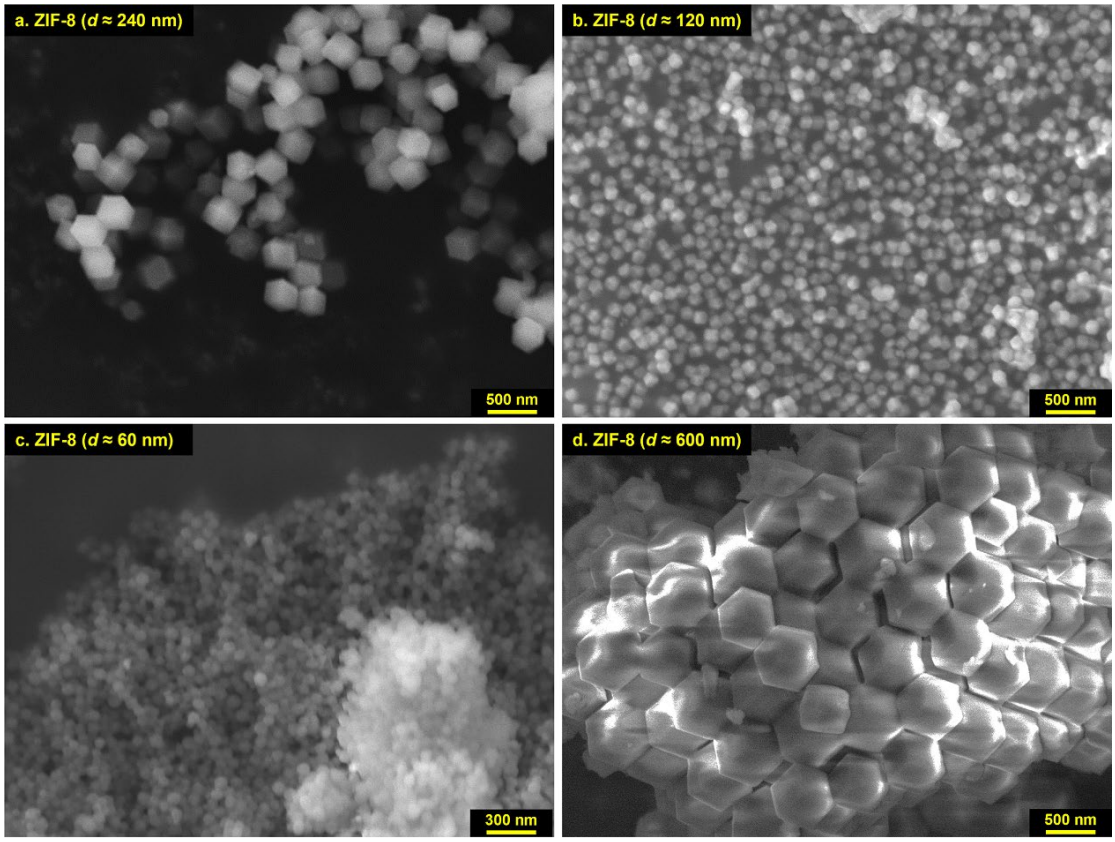

Figure 3-1 SEM images of synthesized ZIF-8 with a diameter of (a) 240 nm, (b) 120 nm, (c) 60 nm and (d) 600 nm.

Increasing the concentration of 2-methylimidazole relative to zinc ions (Zn^{2+}) enhances nucleation rates. This is because a higher abundance of ligand accelerates nucleus formation, resulting in numerous small crystals instead of a few large ones. By adjusting the amount of 2-methylimidazole to 56 g, ZIF-8 with a diameter of approximately 120 nm can be synthesized (**Figure 3-1b**). Methanol, being a smaller and less polar solvent than water, promotes more efficient nucleation and leads to smaller crystal sizes due to the rapid formation of ZIF-8 nuclei.[125] Consequently, performing the procedure in methanol yields ZIF-8 with a diameter of around 60 nm (**Figure 3-1c**). Additionally, the choice of zinc precursor affects the crystal size of ZIF-8. ZIF-8 synthesized using zinc nitrate hexahydrate typically has a larger size (around 600 nm) compared to that synthesized with zinc acetate dihydrate. This difference arises because zinc nitrate fully dissociates in solution, resulting in a higher concentration of free Zn^{2+} ions (**Figure 3-1d**).[126-129]

To obtain hollow ZIF-8, 240 nm ZIF-8 powder was dispersed in water to achieve a concentration of

0.01 g/mL. Then, 200 g of tannic solution (0.025 g/mL) was added to the ZIF-8 suspension. This mixture was stirred for 30 minutes. During this process, tannic acid, as a weak acid, releases free protons that can disrupt the ZIF-8 framework. The relatively large molecular size of tannic acid allows it to block the pores of ZIF-8, preventing complete collapse. After centrifugation, the resulting dry precipitate, tannic acid-etched ZIF-8 (EZIF-8), was obtained. This precipitate was then directly carbonized at 950 °C for 2.5 hours under an argon atmosphere, resulting in the formation of HPC.

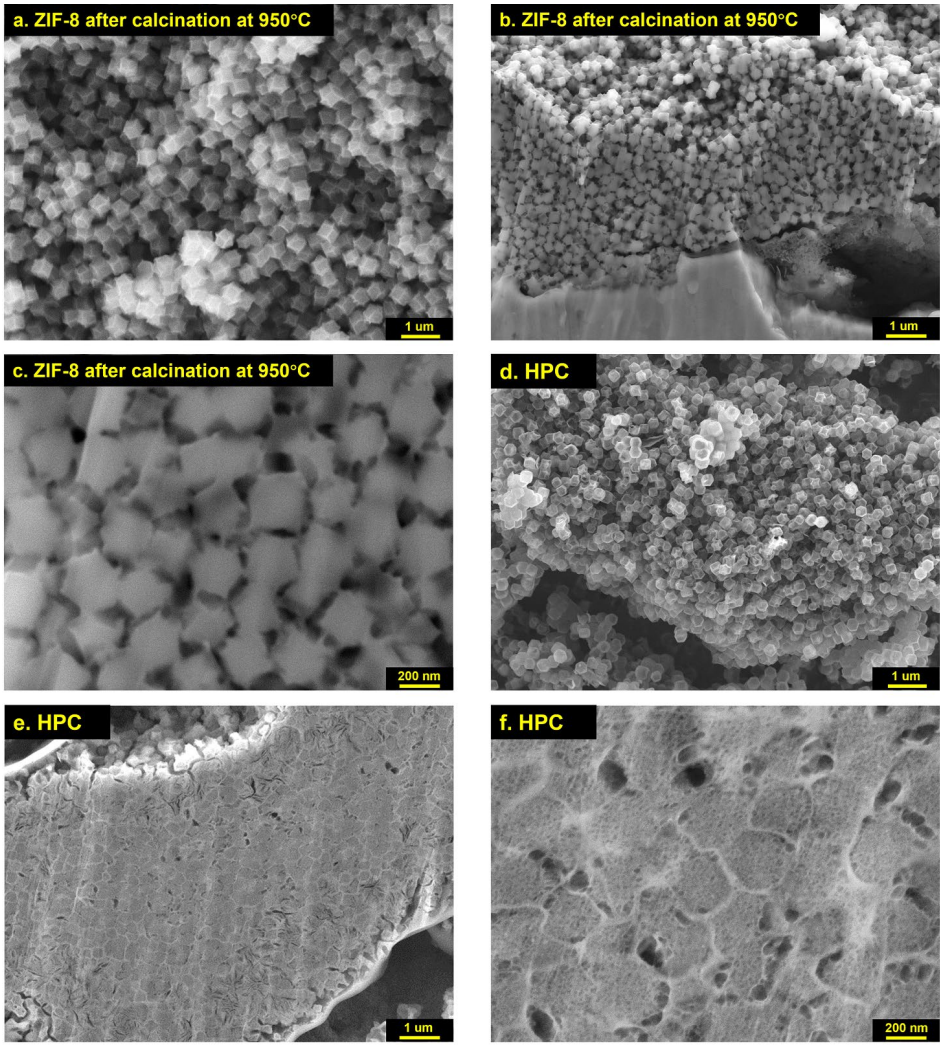

Figure 3-2 (a-c) Topography and cross-section SEM images of the carbon by directly pyrolyzing ZIF-8. (d-f) Topography and cross-section SEM images of HPC by pyrolyzing EZIF-8.

To demonstrate the internal hollow structure, both HPC and the carbon directly carbonized from ZIF-8 were examined using SEM. Unlike the solid hexagonal carbon (**Figure 3-2a−c**), HPC (**Figure 3-2d−f**) show numerous individual hexagonal structures with abundant internal pores. This porous

structure provides ample space to accommodate inverse vulcanization, ensuring uniform distribution of S-DIB in the subsequent synthesis of S-DIB@HPC. To analyze the surface area and porosity of solid carbon and HPC, and to verify changes in porosity after tannic acid etching, N_2 adsorption/desorption isotherms were conducted. Results show that a significant volume of nitrogen molecules adsorbed on the surface of solid carbon and HPC at $P/P_0 < 0.05$, indicating abundant micropores in both samples (**Figure 3-3a**). HPC exhibits a large volume of nitrogen adsorption at P/P_0 from 0.5 to 0.9, attributed to its hollow mesopores as seen in cross-sectional views. The pore size distribution, obtained using the Horvath-Kawazoe (HK) method, reveals changes in the micropore range (0.5–1 nm) between HPC and solid carbon due to the etching process (**Figure 3-3b**). However, HPC showed a significant increase in mesopore volume according to the Barrett–Joyner–Halenda (BJH) distribution results (**Figure 3-3c**). The hollow structure of HPC were further confirmed by high-resolution TEM (**Figure 3-3d−e**). This porous structure also helps maintain the structural integrity of the cathode during the repeated volume expansion and contraction of S/Li_2S during cycling.

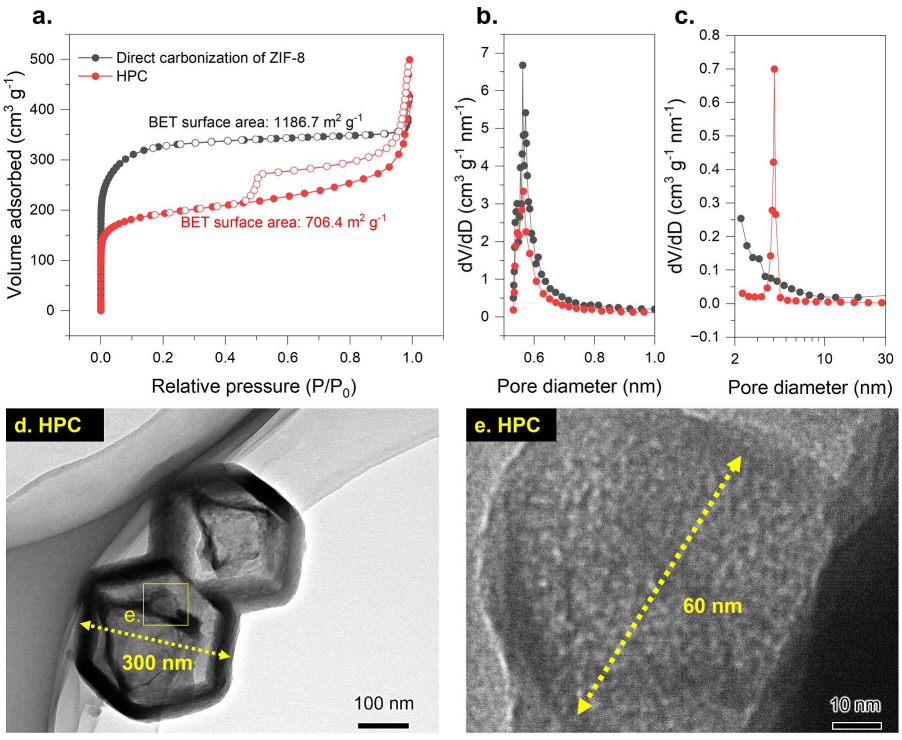

Figure 3-3 N_2 adsorption–desorption isotherms (a) and HK pore size distribution (b) and BJH pore size distribution (c) of direct carbonization of ZIF-8 and HPC, (d–e) HRTEM images of HPC.

The chemical composition and elemental valence of the prepared HPC were further analyzed using XPS. **Figure 3-4a** shows the survey profile of HPC, with three peaks corresponding to the three elements C, N, O. During pyrolysis, some nitrogen atoms from the 2-methylimidazole ligand remain and become incorporated into the carbon framework (3.8 at%). The N 1s peaks were deconvoluted into two main nitrogen species: pyridinic-N (398.1 ± 0.1 eV) and graphitic-N (400.6 ± 0.1 eV) **(Figure 3-4b)**.[130, 131] Graphitic nitrogen is known to improve the conductivity of hollow carbon and enhance electron transfer within the material. Pyridinic nitrogen effectively adsorbs polysulfides and catalyzes battery reactions (**Figure 3-4c**).[131] The deconvoluted C 1s signal in **Figure 3-4d** shows two main peaks at 284.6 and 285.7 eV, corresponding to sp^2-hybridized graphite-like carbon (C–C sp^2) and sp^3-hybridized diamond-like carbon (C–C sp^3), respectively. Peaks at 286.6, 287.6, and 289.1 eV are attributed to surface oxygen and nitrogen groups (designated as C–O/C–N, C=O/C=N, and C=O–O, respectively).[38]

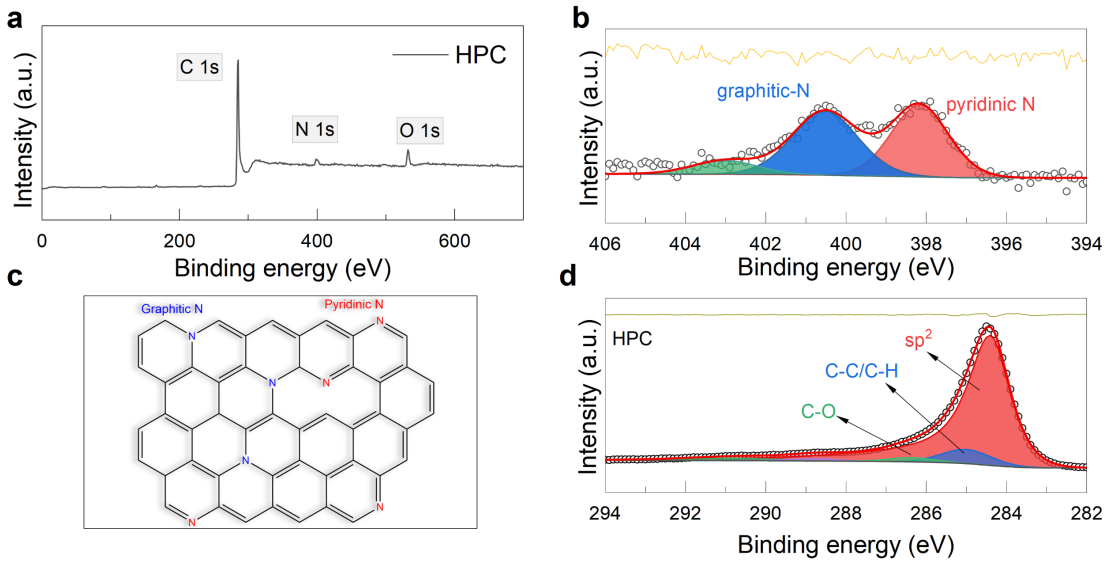

Figure 3-4 (a) The survey scanned XPS of HPC. (b) Deconvoluted N 1s spectrum. (c) The scheme of graphitic N and Pyridinic N. (d) Deconvoluted C 1s peaks of HPC.

3.2.2 Synthesis of S-DIB

For S-DIB synthesis, 4.5 g of sulfur was added to a 20 mL glass vial equipped with a magnetic stirring bar and heated to 185 °C in an oil bath until a clear yellow molten phase formed. Then, 0.5 g of DIB was added to the molten sulfur. The reaction mixture was stirred for 15 minutes until it stopped. The resulting copolymer was cooled and collected by breaking the glass. The completion

of the inverse vulcanization reaction was indicated by a visual color change, to transparent red polymeric glass (**Figure 3-5a**). According to the FTIR results in **Figure 3-5b**, the peaks at 1040 cm^{-1} and 3083 cm^{-1}, representing the C=C stretch and C=C–H bend in the spectrum of DIB, disappear in S-DIB.[132, 133] The peak at 692 cm^{-1} correspond to the C–S bond shows in S-DIB. These changes confirm the connection with sulfur chains after the opening of carbon-carbon double bonds in DIB. The lack of long-range periodicity at the atomic level in S-DIB is demonstrated by its weak XRD peaks (**Figure 3-5c**).

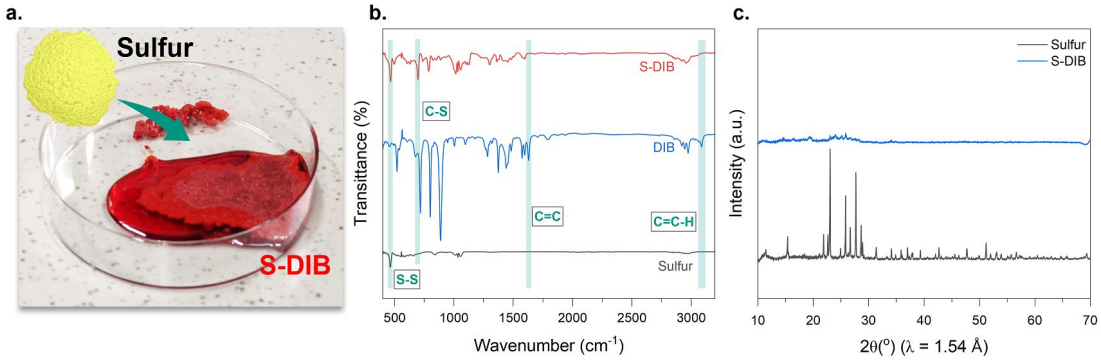

Figure 3-5 (a) The photo of sulfur and synthesized S-DIB. (b) FTIR profiles of sulfur, DIB and S-DIB. (c) The XRD profile of sulfur and S-DIB.

3.2.3 Synthesis of S@HPC and S-DIB@HPC

S@HPC was prepared by heating a pre-mixed sulfur powder (70 wt%) and HPC (30 wt%) at 155 °C for 6 hours in a well-sealed tube filled with argon.

For the synthesis S-DIB@HPC, the procedure is illustrated in **Figure 3-6a**. First, the well mixed HPC and sulfur were sealed in a container and heated at 175 °C for 5 minutes to conduct sulfur-melt diffusion. Then, 10 wt% DIB (relative to the mass of sulfur) was added, and the temperature was increased to 185 °C to promote efficient polymerization initiation. The reaction was complete in about 8 minutes, after which the mixture was allowed to cool to ambient temperature to obtain S-DIB@HPC.

To verify the feasibility of conducting inverse vulcanization directly in HPC, DSC profiles of S@HPC, S-DIB, and S-DIB@HPC were obtained under air conditions. In **Figure 3-6b**, the S@HPC sample exhibits two distinct melting peaks, indicative of the orthorhombic and monoclinic phases

of sulfur, occurring at 21.4 °C and 105.6 °C, respectively. Notably, the melting of sulfur observed in the S-DIB@HPC and S-DIB samples is significantly diminished, suggesting a conversion of crystalline sulfur to S-DIB, accompanied by a glass transition at −13.9 °C (**Figure 3-6c**). The DSC profiles confirm that S_8 was almost entirely converted into S-DIB during the copolymerization process.[67] TGA results show that sulfur loadings of 69 wt% for S-DIB@HPC, 86 wt% for S-DIB, and 70 wt% for S@HPC (**Figure 3-6d**), indicating that S-DIB was formed without sulfur loss through the diffusion of DIB into the porous carbon structure.

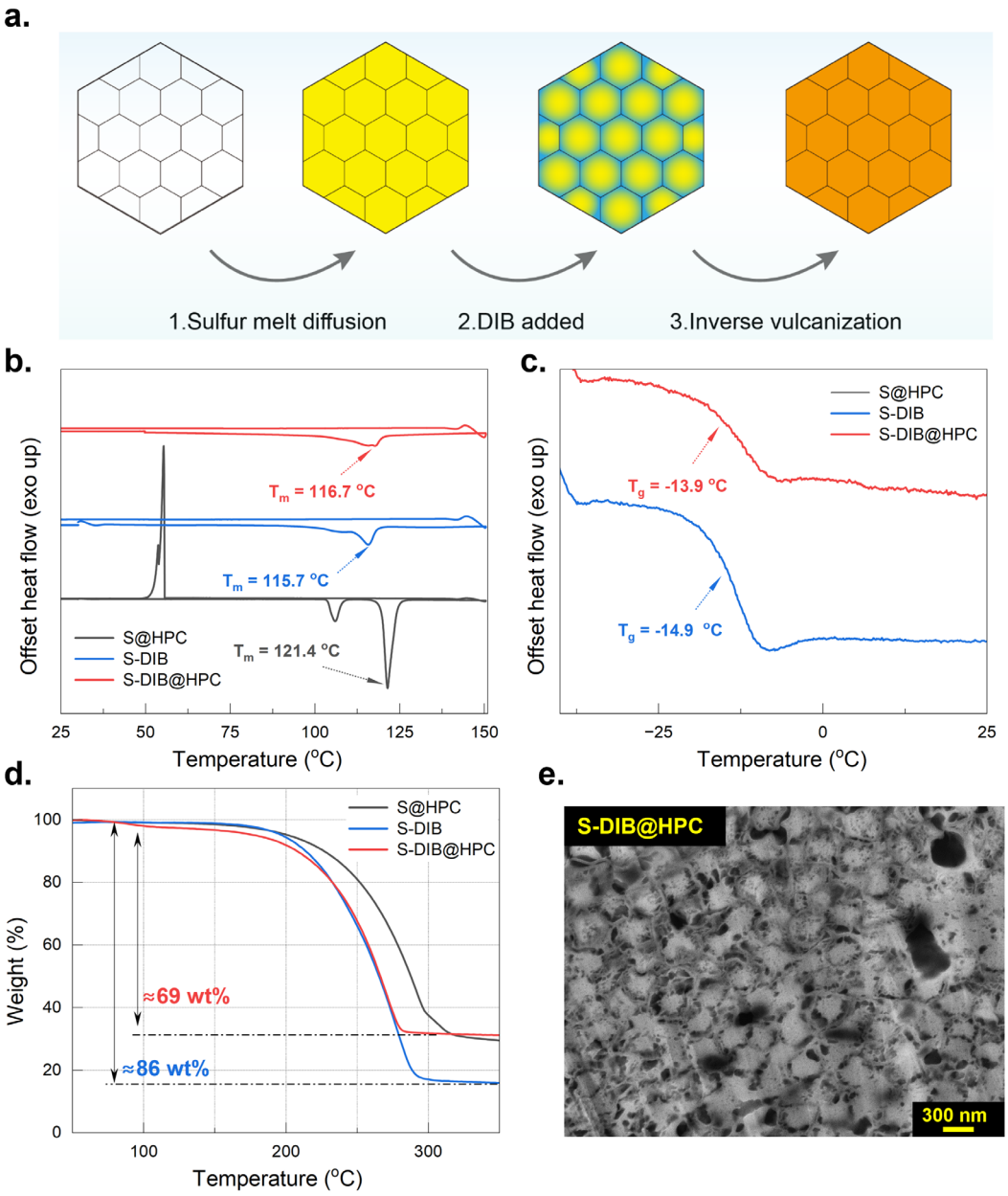

Figure 3-6 (a) Schematic of the synthesis of S-DIB@HPC. (b) DSC results of S@HPC, S-DIB and S-DIB@HPC from 25 °C to 150 °C. (c) DSC results of S@HPC, S-DIB and S-DIB@HPC from −30 °C to 25 °C. (d) TGA curves of S@HPC, S-DIB and S-DIB@HPC. (e) The cross-section SEM image of the S-DIB@HPC.

The ion-polished coating was analyzed using SEM to examine the distribution of S-DIB within HPC. Following polymerization (**Figure 3-6e**), the majority of the internal pores were filled with S-DIB. The uniform distribution of S-DIB across the HPC was confirmed by EDX mapping results (**Figure 3-7**).

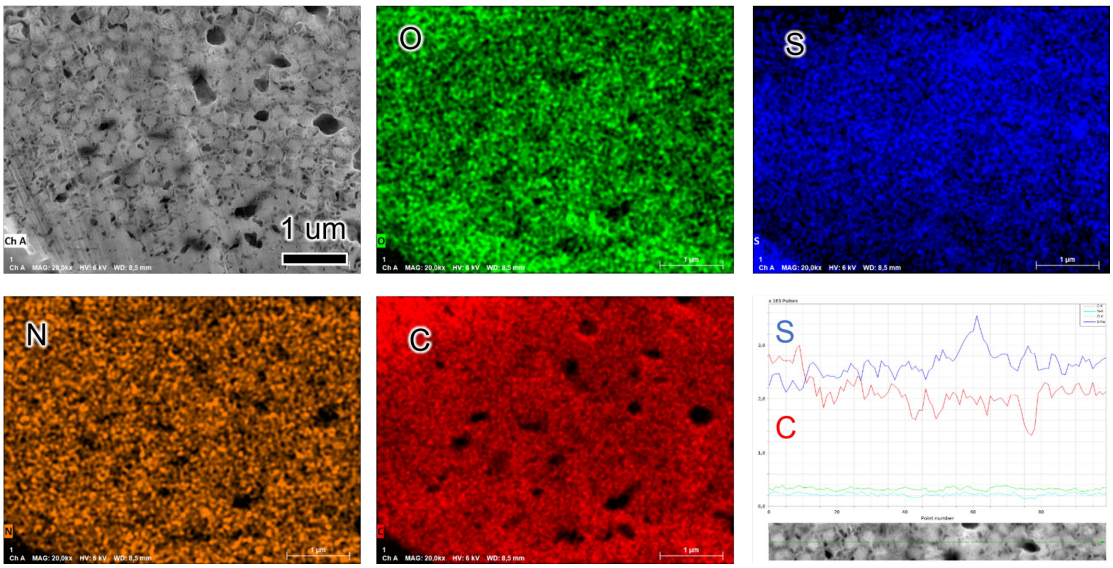

Figure 3-7 EDX mapping images of the S-DIB@HPC.

3.3 Electrochemical performance

3.3.1 Electrochemical measurement details

A slurry was prepared by mixing 75 wt% S-DIB@HPC, S@HPC, 15 wt% Ketjenblack, and 10 wt% LA133 (3%) latex. To ensure comparability of the electrodes, the S-DIB slurry consisted of 60 wt% S-DIB, 30 wt% Ketjenblack, and 10 wt% binder. The slurry was then coated onto Al foils, dried at room temperature overnight, and subsequently at 60 °C under vacuum for 6 hours. The dried electrodes were punched into small disks with a diameter of 12 mm to serve as sulfur cathodes, with an areal sulfur loading of approximately 1.6 mg S cm^{-2}. Electrochemical measurements were conducted using standard 2025-coin-type cells, with a piece of Li foil (14.0 mm diameter) as the anode and Celgard 2500 as the separator. The electrolyte used was 1.0 mol L^{-1} LiTFSI and 1 wt % $LiNO_3$ dissolved in DOL/DME (v/v = 1:1). The E/S ratio was 12 µL electrolyte/mg_{sulfur} for regular condition and 8 µL electrolyte/mgS for lean electrolyte conditions. The cells were galvanostatically cycled between 1.7–2.7 V on the VMP-3 under different C-rates (1 C = 1675 mA g^{-1}). CV curves with a potential window of 1.6–2.8 V and EIS (10 mHz–100 kHz) measurements were performed

using a Biologic VMP-3 multichannel workstation. The same instrument was also used to perform GITT, alternating 20-minute 0.05 C constant current pulses with the 2-hour OCV periods. The *Operando* Raman test was conducted using a coin cell with a quartz window.

3.3.2 Electrochemical results

To evaluate the impact of confined inverse vulcanization on the electrochemical characteristics of a Li−S battery, galvanostatic charge-discharge tests were conducted at various C-rates (1C = 1675 mA g^{-1}) to measure capacity and coulombic efficiency. The S-DIB@HPC electrode demonstrates superior rate capability in comparison to S@HPC and S-DIB (**Figure 3-8a**), achieving capacities of 1091, 846, 771, 698, 583, 529, and 150 mAh g^{-1} at C-rates of 0.1, 0.2, 0.5, 1, 2, 3, and 5 C, respectively. Remarkably, the capacity is almost entirely preserved when the current density is reverted from 5 C back to 0.1 C.

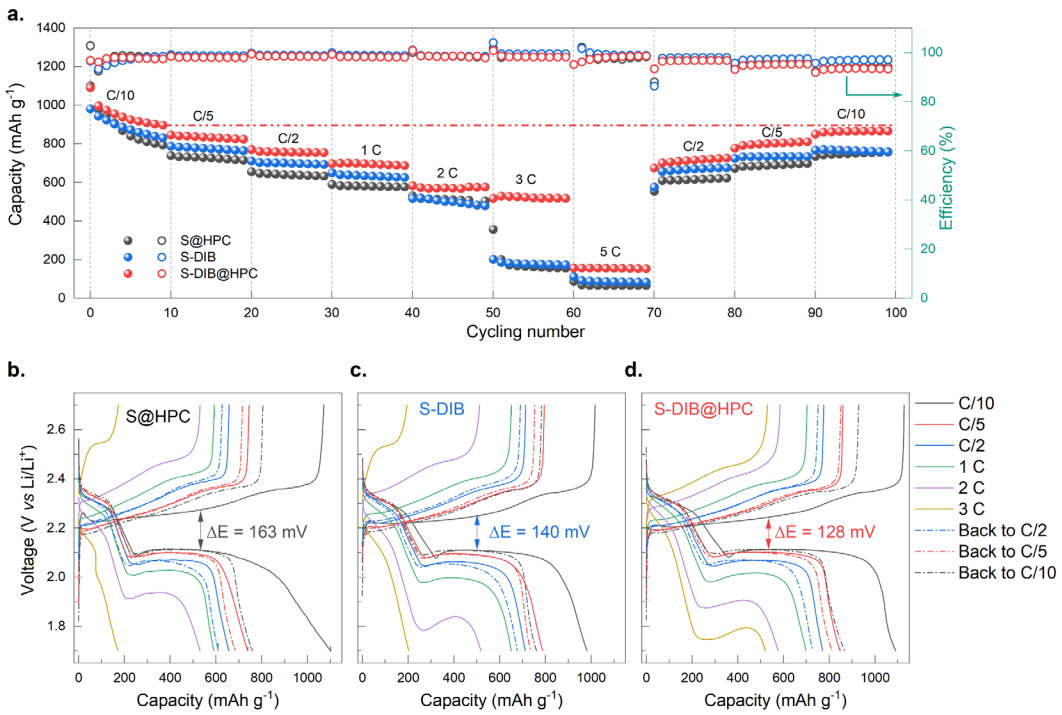

Figure 3-8 (a) C-rate performance of S@HPC, S-DIB and S-DIB@HPC cathodes measured from C/10 to 3 C then back to C/10. Discharge and charge profiles of (a) S@HPC, (b) S-DIB and (c) S-DIB@HPC.

As **Figure 3-8b−d** show, the voltage difference measured from the charge/discharge plateau (ΔE = 128 mV) indicates moderate electrochemical polarization for S-DIB@HPC, compared to 163 mV and 140 mV for S@HPC and S-DIB, respectively. This suggests that the porous carbon structure

facilitates the rapid conversion of soluble LiPS into insoluble Li_2S_2/Li_2S.[134]

S-DIB is electrically insulating, the extensive interfacial contact of HPC helps to reduce ohmic polarization. To further investigate polarization, internal resistance was calculated based on GITT results at a rate of 0.05C (**Figure 3-9a**−**c**). As **Figure 3-9d** shows, the S-DIB and S-DIB@HPC electrodes exhibit smaller ΔR values during Li_2S nucleation compared to the S@HPC electrodes.[78, 85] Additionally, S-DIB@HPC shows the lowest resistance for Li_2S activation during charging. These findings suggest that the polymerized sulfur domains enhance nucleation kinetics in the formation of Li_2S, and a favorable spatial distribution can further accelerate the redox reaction rate.

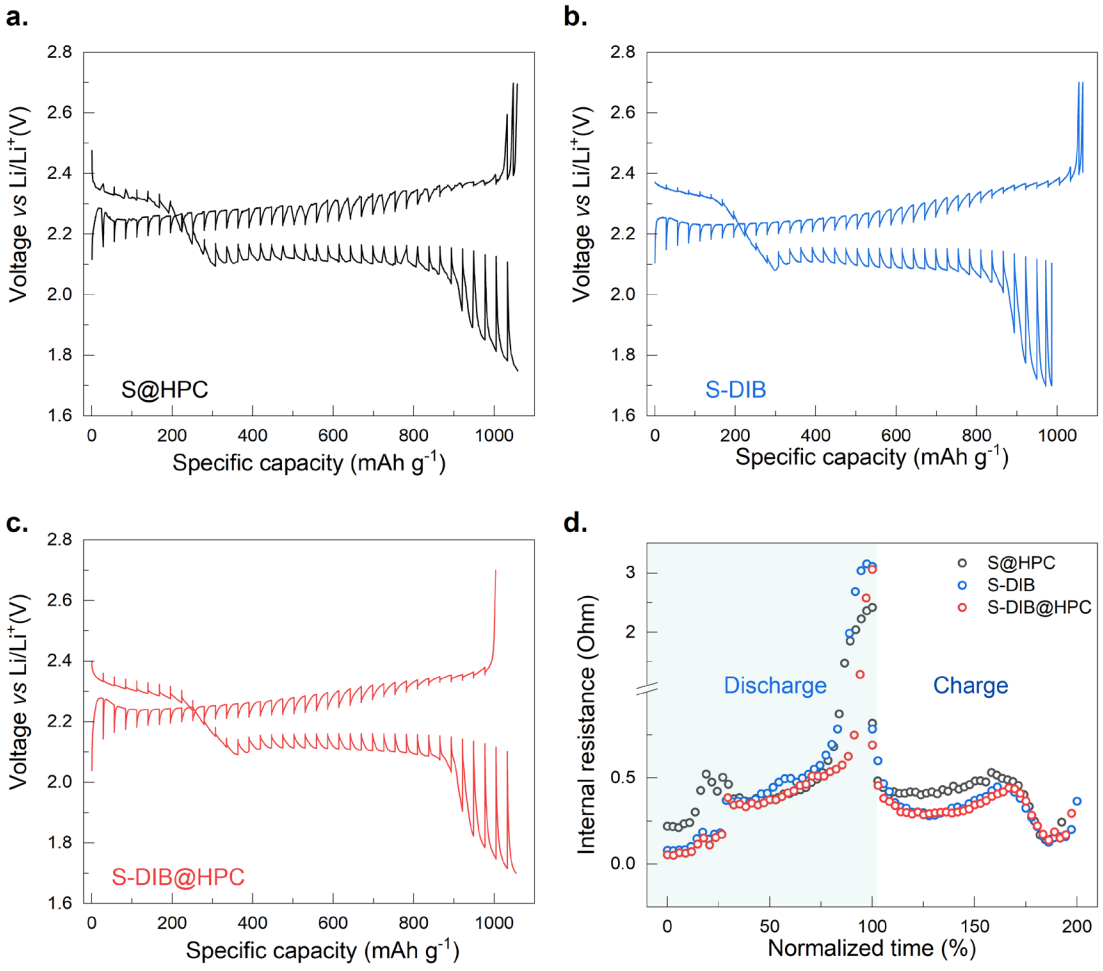

Figure 3-9 GITT plots of (a) S@HPC, (b) S-DIB and (c) S-DIB@HPC electrode. (d) The internal resistance relative to the normalized discharge-charge time.

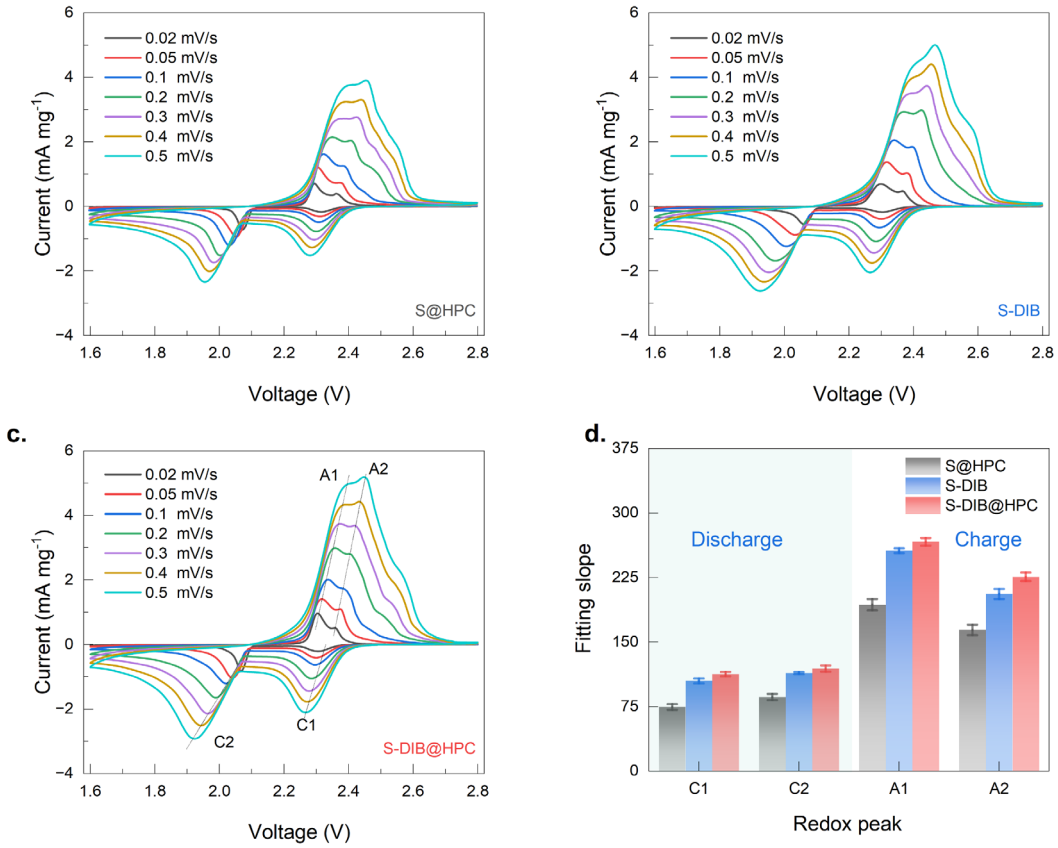

Figure 3-10 CV curves of (a) S@HPC, (b) S-DIB and (c) S-DIB@HPC electrode at different scan rates. (d) Slope of the fitted line between the peak current of the redox peak and the square root scan rate.

To investigate differences in the apparent diffusion coefficient of lithium ions, $D(Li^+)$, CV at varying sweep rates were performed (see **Figure 3-10a**−**c**). All the samples display two broad overlapping cathodic and anodic peaks. The cathodic peak at 2.31 V (C1) and the anodic peak at 2.36 V (A1) correspond to the transition between S-DIB and LiPS, while the cathodic peak at 2.08 V (C2) and the anodic peak at 2.29 V (A2) relate to the conversion between soluble LiPS and insoluble Li_2S_2 or Li_2S. The peak currents for both cathodic and anodic reactions show a linear correlation with the square root of the scanning rate, following the Randles-Sevcik equation. According to this equation, the slope of the curve ($I_p/v^{0.5}$) is related to the apparent $D(Li^+)$ for the specific electrochemical steps.[135] While the Randles-Sevcik equation was initially derived under conditions of semi-infinite diffusion, caution should be taken when interpreting absolute values of the diffusion coefficient determined under confined diffusion. However, given the similar porous structures of S@HPC and S-DIB@HPC, and the fact that both electrodes contain the same active material, the classical Randles-Sevcik equation can be reliably used for qualitative analysis of how the HPC structure and S-DIB influence lithium diffusion in these electrodes. The fitting results shown in **Figure 3-10d**

reveal a higher overall slope for S-DIB@HPC, indicating enhanced lithium-ion diffusivity.

Benefitting from its dual-confinement effect due to the porous carbon material and DIB as a reagent, the S-DIB@HPC electrode shows the highest reversible capacity of ~488 mAh g^{-1} after 500 cycles at 1C (**Figure 3-11a**). In contrast, S@HPC and S-DIB only reach capacities of ~375 and ~102 mAh g^{-1}. It is important to note that, in contrast to the decreasing trends observed in S@HPC and S-DIB@HPC, S-DIB exhibits an initial increase during the first 100 cycles, followed by a subsequent decline. This behavior is likely attributed to the gradual activation of bulk S-DIB within the electrode during the reaction. The capacity for fast charging and discharging is an essential indicator of the efficacy of energy storage materials. **Figure 3-11d** shows the long-cycle performance of S-DIB@HPC at 2 C, demonstrating that the material retains a specific capacity of 419 mAh g^{-1} after 500 cycles. This indicates excellent cycle stability at a higher current. Using a lean electrolyte loading of 8 µl mg^{-1} of sulfur, it maintained 80% capacity after 200 cycles, indicating high sulfur utilization and low sulfur loss (**Figure 3-11c**). The electrochemical measurements confirm that the cross-linked S-DIB confined in the hollow carbon matrix can efficiently facilitate the ion transportation and minimize the “shuttle effect”.

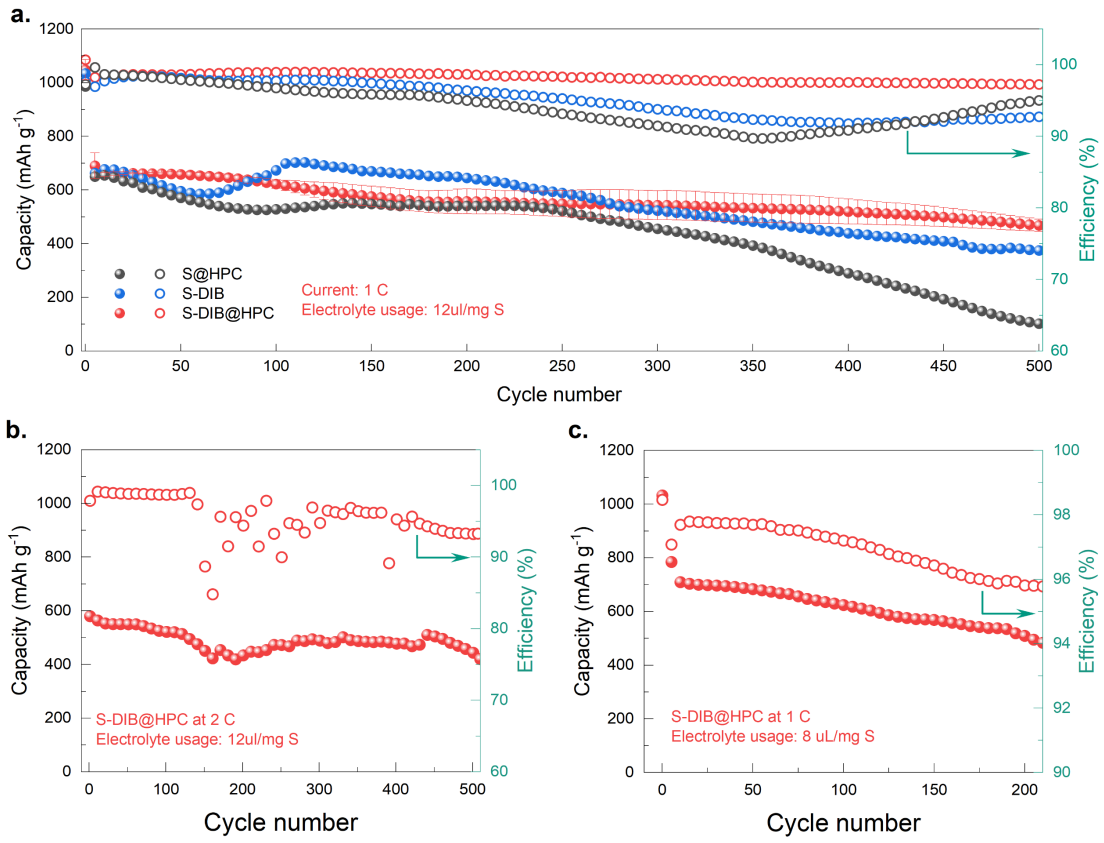

Figure 3-11 (a) Cycling performances of the S@HPC, S-DIB, and S-DIB@HPC electrode at 1 C. (b) The cycling performance of S-DIB@HPC at 2 C. (c) The cycling performance of S-DIB@HPC electrode at 1 C under a lean electrolyte usage of 8 uL/mg S.

3.4 Application of EsB detector in a Li−S system

To better understand how the porous carbon structure influences the reaction kinetics and fundamental de-/lithiation processes of S-DIB, we visualized the conversion process within the material. This was accomplished by combining broad ion beam cross-sectioning with EsB imaging in an electron microscope. In SEM, secondary electrons typically examine the sample's surface topography. While BSE, reflected through elastic scattering, can also be detected. The intensity of the BSE signal is closely linked to the atomic number (Z) of the materials, allowing for the visualization of element distribution based on signal strength variations. However, traditional BSE imaging is limited to elements with high atomic numbers. Using an EsB allows for precise filtration of low-energy (approximately 100−1500 eV) backscattered electrons, enhancing the visualization of light elements involved in the reactions and their intermediates (**Figure 3-12a**).[123]

In Li–S batteries, sulfur acts as an active material, and carbon as the sulfur host and conductive

component, with elastically scattered electrons being reflected with different energies. By gradually increasing the voltage of the EsB filter grid, fewer backscattered electrons from carbon reach the backscatter detector compared to sulfur regions. To verify this, one half of highly oriented pyrolytic graphite (HOPG) was coated with sulfur while the other half was freshly exfoliated and used as a reference to find the best EsB settings. In the SEM image in **Figure 3-12b**, the left part shows a smooth surface of HOPG and the right part shows a thin sulfur film. When switching to the EsB detector (**Figure 3-12c**), elastic electrons from carbon are cut off so that the carbon region appears completely black, while the higher energy back-scattered electrons from the sulfur pass the grid threshold, causing the sulfur region to appear brighter.

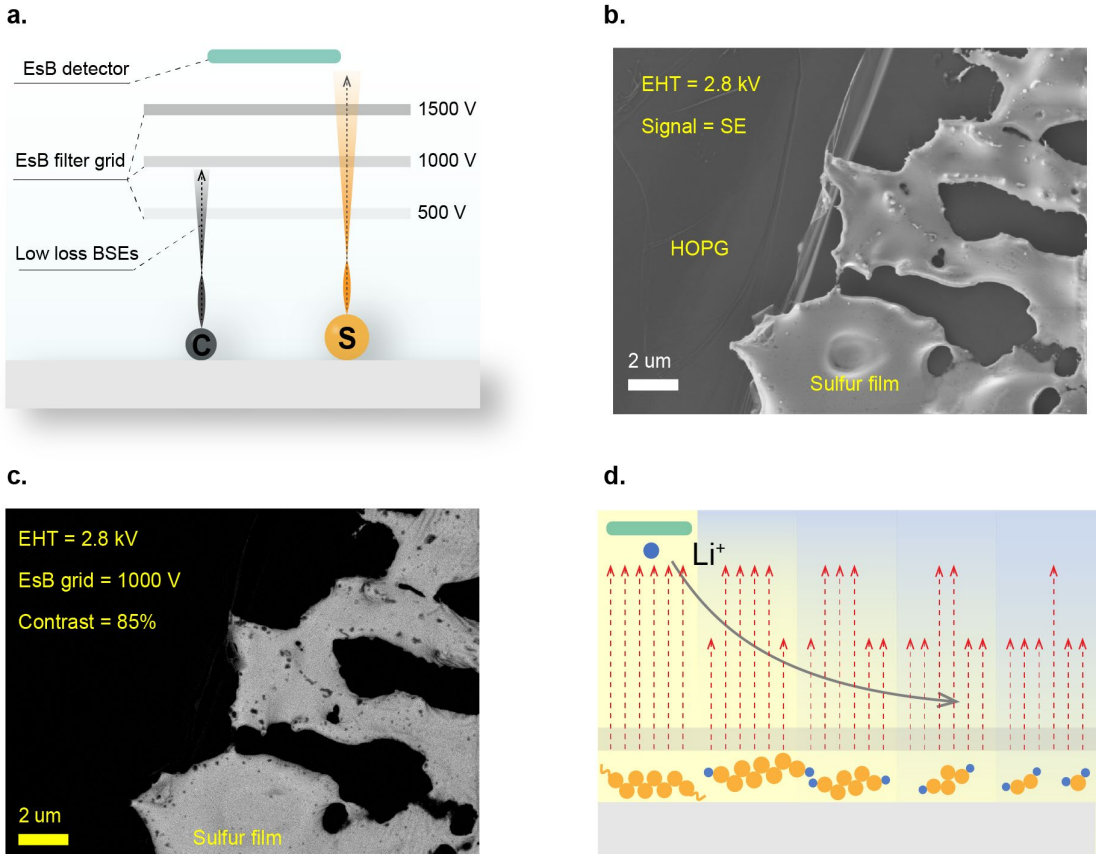

Figure 3-12 (a) Scheme of the working mechanism of EsB detector for detecting C and sulfur. (b) The image of sulfur film on HOPG obtained from SE detector. (c) The image of sulfur film on HOPG obtained from EsB detector, EsB grid is set to 1000 V. (d) Scheme of working mechanism of EsB detector for identifying species from S to Li_2S.

The evolution of sulfur species during the charge-discharge processes of a Li–S battery was further investigated by EsB imaging. Sulfur serves as a typical anion-redox cathode during the discharge process, wherein one sulfur atom combines with two Li^+ to form Li_2S. However, the actual sequence

of reactions is highly complex, with numerous intermediate molecular species likely to be present. As the depth of discharge increases, more lithium ions migrate to the cathode and react with sulfur to produce Li_2S_x. The formation of Li^+ ligands bonded to sulfur results in a contrast difference, as illustrated in the schematic representation in **Figure 3-12d**. Consequently, variations in brightness are expected to indicate different levels of lithiation.

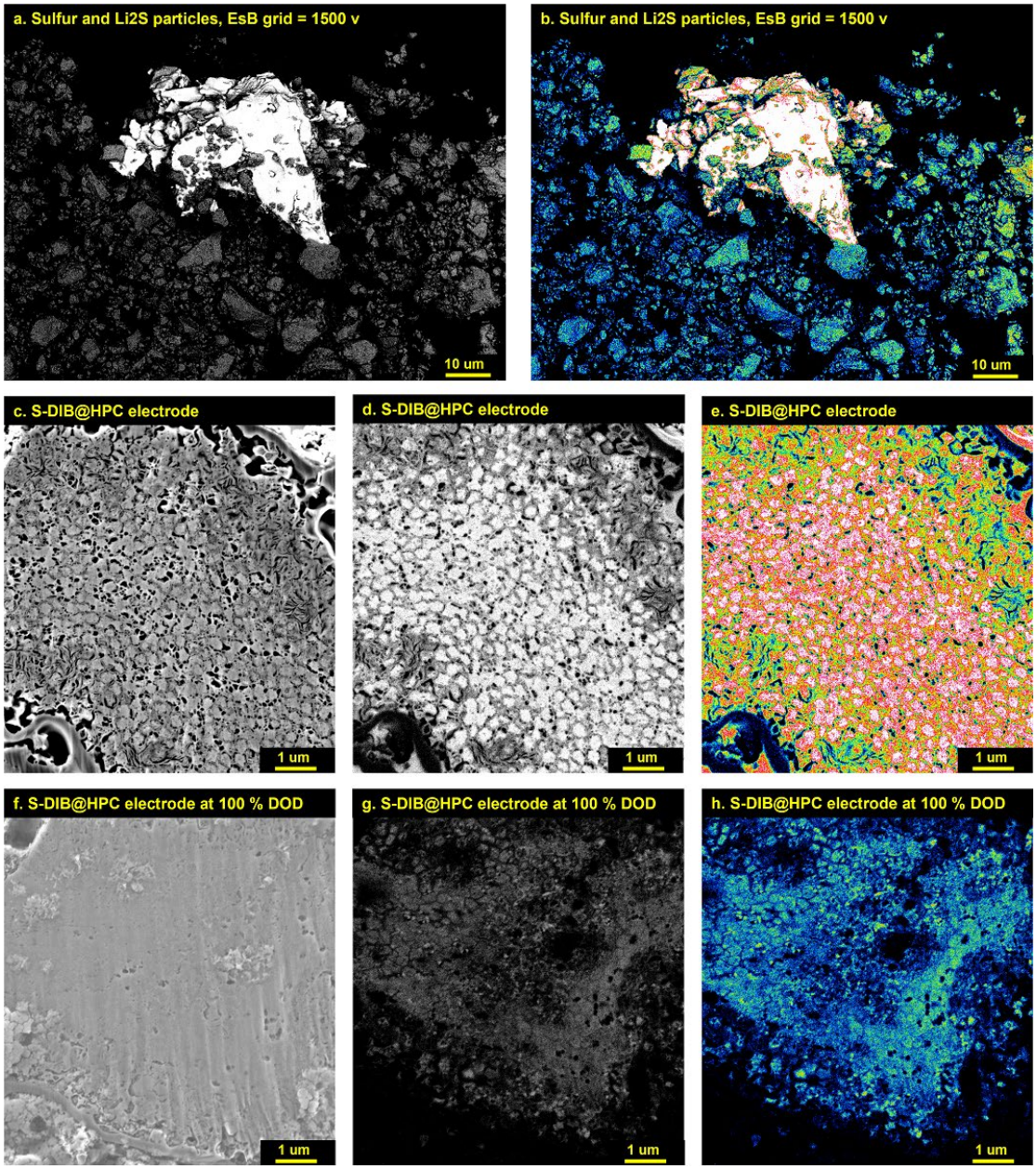

Figure 3-13 (a) EsB and (b) the heat-map processed EsB image of S and Li_2S. The cross-section image of the pristine S-DIB@HPC electrode obtained by (c) SE detector and (d) EsB detector. (e) The heat map processed EsB image. (f–h) The cross-section image of the fully discharged S-DIB@HPC electrode obtained by SE and EsB detector.

For validation, S and Li_2S powders were characterized using the EsB detector. As shown in **Figure**

3-13a and **b**, Li_2S particles appear much darker compared to sulfur because of lower sulfur density and bonding state in Li_2S. The cross-section of polished pristine and fully discharged electrodes was characterized by both SE and EsB detectors, as shown in **Figure 3-13c–h**. The corresponding EsB images show a markedly reduced intensity of backscattered electrons for the discharged electrode, which aligns with the anticipated decrease in BSE signals from Li_2S_2/Li_2S compared to S-DIB. Therefore, intermediates formed during the discharge and charge processes may exhibit noticeable differences in brightness between sulfur and Li_2S.

3.5 The redox pathway of S-DIB

The redox pathway of S-DIB during the discharge and charge process was investigated using *operando* Raman measurements, along with the EsB technique, XPS and NMR spectroscopy for electrodes at 20 %, 40 %, 60 %, 80 % DOD and 30 %, 60 %, 90 % SOC. EsB images were converted into heat-maps to visualize the gradual de/lithiation. Bright pixels correspond to white and red, while dark pixels are mapped to blue and black. Since the intensity of the EsB signal decreases with increasing lithiation of the sulfur-species, different colors represent changes between S-DIB and fully discharged S-DIB, indicating the gradual transition from long-chain to medium-chain and short-chain organic and inorganic LiPS.

Figure 3-14 presents the Raman spectra of an S-DIB@HPC electrode at various states of charge. The initial spectrum, recorded at 14% DOD, reveals prominent characteristic S–S stretching vibrations at 152, 217, and 473 cm^{-1}, along with shoulder peaks at 246 and 438 cm^{-1}, associating with S-DIB and long-chain polysulfides C(Li)-S_x($x \approx 8$)-Li, similar to those found in elemental sulfur (S8). The peak observed at 400 cm^{-1} is attributed to the emergence of medium-chain lithium polysulfides (LiPS), specifically C(Li)-S_x($x \approx 6$)-Li, while the peaks at 200 cm^{-1} and 449 cm^{-1} correspond to short-chain LiPS, identified as C(Li)-S_x($x \approx 4$)-Li.[7, 91, 136]

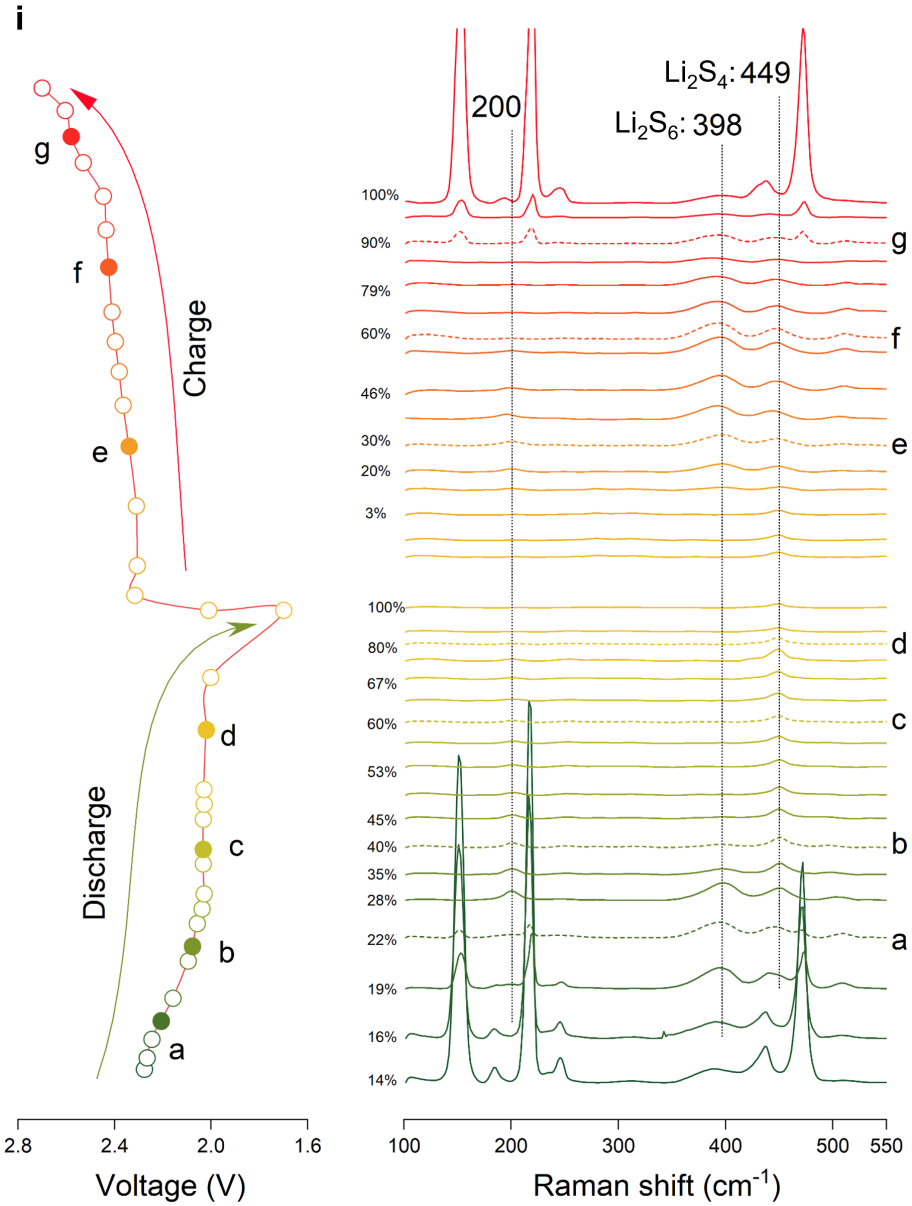

Figure 3-14 *Operando* Raman spectra of S-DIB@HPC, with the charging/discharging curve of the operando cell on the left.

3.5.1 Galvanostatic discharge (lithiation) process

The S-DIB in the hollow porous carbon, on average has one DIB unit per 44 linearly connected sulfur units. At the beginning of discharge, fading characteristic Raman peaks of S-DIB demonstrate rapid consumption and conversion to Li_2S_8 and long-chain organosulfur-DIB units C-S_x-Li (x≈8). At about 22% DOD, the characteristic Raman peaks of the long chain polysulfide start to disappear DOD, while new signals of C-(Li)-S_x-Li (x ≈6) emerge. Consistent with Raman spectra changes, EsB images at 20% DOD show a small amount of long-chain C(Li)-S_x-Li (x ≈8) in the region marked by the dotted line, which is surrounded by medium-chain LiPS. Thus, during the initial 20%

of the discharge process, polymeric S-DIB is broken down to long- and medium-chain LiPS as described by reaction (1), (2) and (3) of the following reaction scheme.

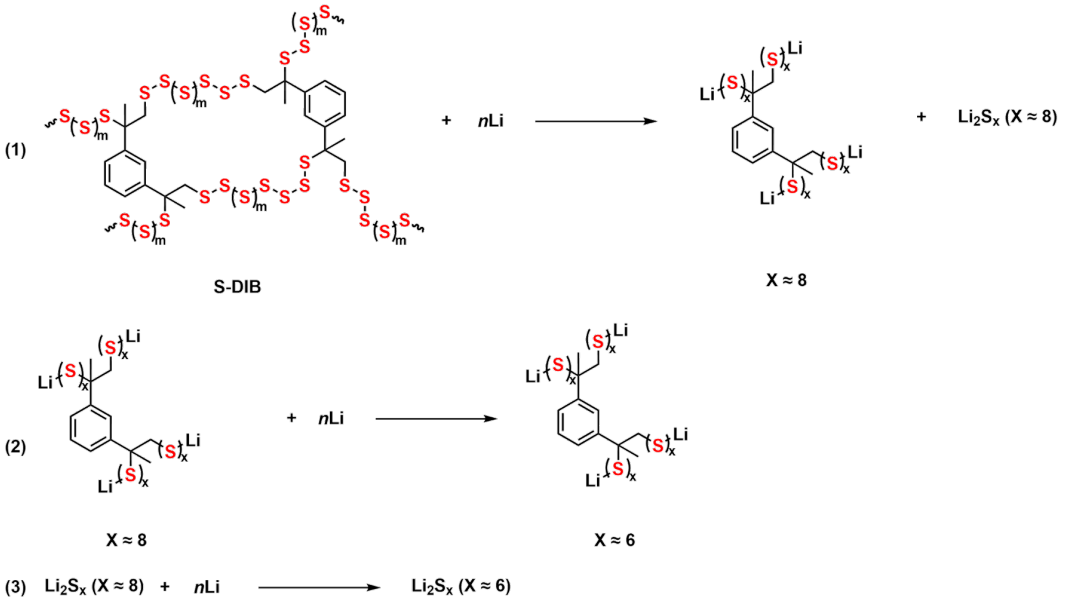

As discharge progresses, the peak of the short-chain LiPS species increases, reaching its maximum at 35 % DOD, accompanied by the gradual disappearance of the medium-chain LiPS. Thus, from 22% DOD to 35% DOD, mainly the conversion of medium-chain LiPS to short-chain LiPS takes place, which ends at 35 to 40% DOD, followed by the consecutive reduction of short-chain LiPS to Li_2S_2/Li_2S. The trend is visible in the EsB image at 40 % DOD, (**Figure 3-15b**) showing Li_2S_2/Li_2S (blue and green) forming mainly near the HPC particle surface, indicating Li-diffusion control. The existence of Li_2S/Li_2S_2 toward the end of discharge was further confirmed by ^{7}Li NMR spectroscopy (**Figure 3-16a**).[135, 137, 138]

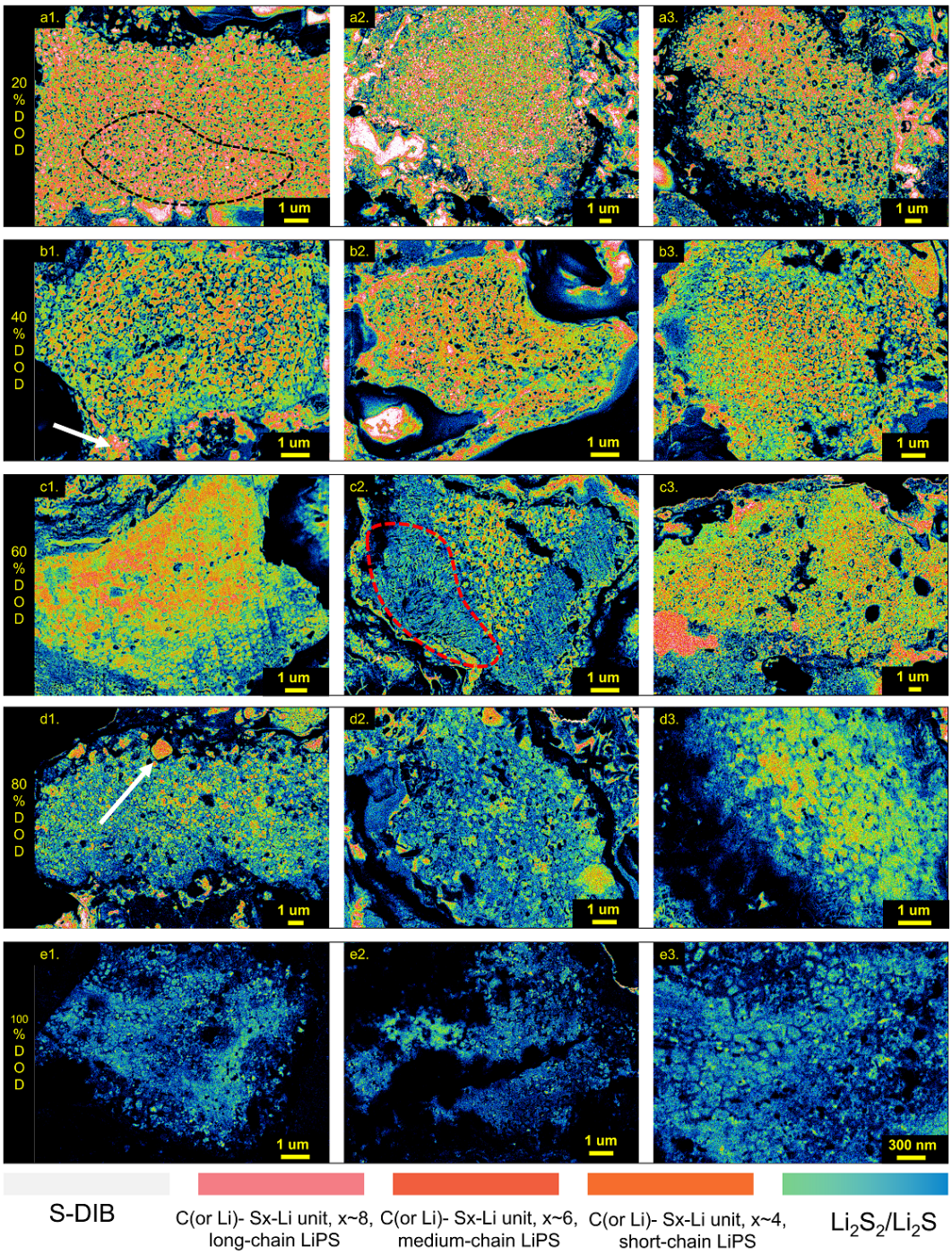

Figure 3-15 Heat map processed EsB image at (a) 20 % DOD (b) 40 % DOD (c) 60 % DOD (d) 80 % DOD (e) 100 % DOD. On the right is the colour gradient and its corresponding species.

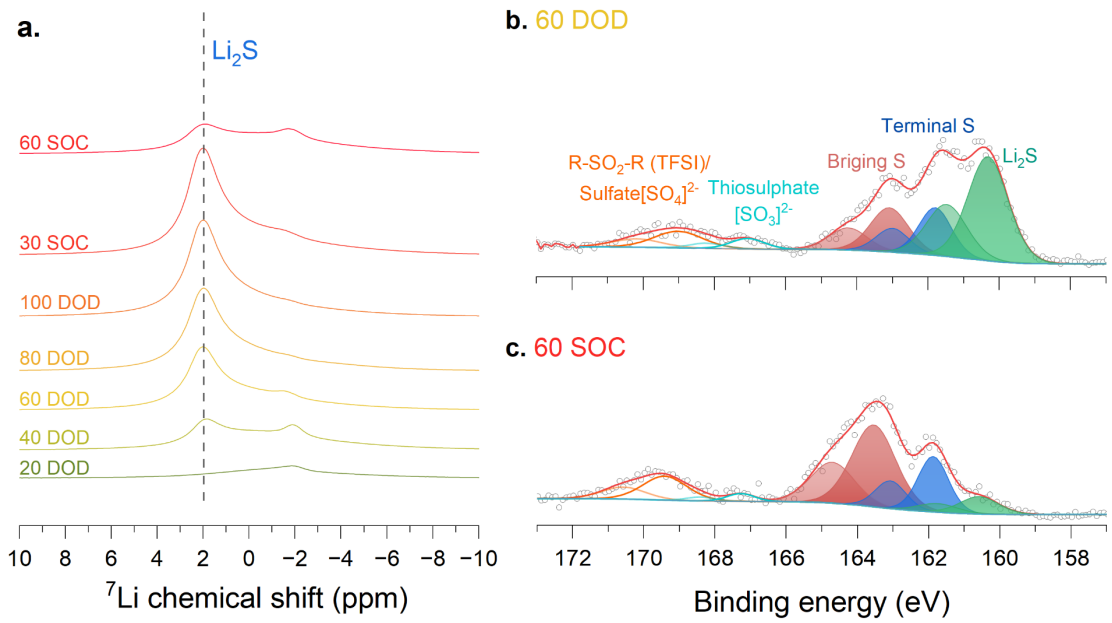

Figure 3-16 (a) ^{7}Li NMR spectrum of the S-DIB@HPC electrode at 20 % DOD, 40 % DOD, 60 % DOD, 80 % DOD, 100 % DOD, 30 % SOC and 90% SOC. The XPS and fitted peaks of the electrode at (b) 60% DOD and (c) 60 % SOC.

Driven by the discharge current and Li^+ concentration gradient, short-chain LiPS progressively occupies less area, while Li_2S_2/Li_2S occupy larger area at 60% DOD shown in **Figure 3-15c**. XPS analysis at 60% DOD (**Figure 3-16b**) shows the S 2p spectrum deconvoluted into five pairs of peaks. Two weak peaks at 167.2 and 169.4 eV are ascribed to thiosulfate and sulfate species. Peaks at 163.1, 161.8 eV and 160.3 eV correspond to bridging sulfur (S_B^0), terminal sulfur (S_T^{-1}) and S^{2-} in Li_2S, respectively.[118, 119] Bridging sulfur corresponds to sulfur connected to other sulfur atoms in a sulfur chain, while the terminal sulfur peak emerges from sulfur at the end of a sulfur chain. The amount of S_B^0 is approximately 1.2 times that of S_T^{-1}. Theoretically the ratio of S_B^0 to S_T^{-1} is 2.5 and 1.5 for Li_2S_6 and Li_2S_4. This proves that at 60% DOD, the reduction reaction to Li_2S_2/Li_2S of Li_2S_4 exist in the cell. The concordance between XPS and EsB results reinforces the precision of sulfur species distribution obtained through the EsB detector. At 80% DOD, short-chain LiPS C-(Li)-S_x-Li ($x \approx 4$) have almost completely converted to Li_2S_2/Li_2S (**Figure 3-15d**). At 100% DOD in **Figure 3-15e**, in the final stage of discharge, residual short chain LiPS is reduced to Li_2S_2/Li_2S, while solid phase Li_2S_2 simultaneously reduces to Li_2S.

During discharge, as shown by white arrows in **Figure 3-15a1** and **a3**, S-DIB formed outside the carbon skeleton converts more slowly and cannot be completely lithiated due to their size. S-DIB

within the carbon skeleton can be lithiated evenly, as the porous carbon network ensures effective electron transport and favors lithium-ion transport. The distribution of long-, medium-, and short-chain intermediates at different discharge depth demonstrates local differences in Li^+. Moreover, as illustrated in **Figure 3-15c2**, partial carbon units at 60% DOD cannot confine LiPS in pores due to the shuttling effect, explaining the discrepancy between the initial capacity and the theoretical capacity. It is noteworthy that all intermediates, Li_2S_8, Li_2S_6, and Li_2S_4, are soluble in the electrolyte. However, the loss of active material is not observed in the electrodes at 20% and 40% DOD as the reaction kinetics of $Li_2S_4 \rightarrow Li_2S_2/Li_2S$ is slower than that $Li_2S_8 \rightarrow Li_2S_6 \rightarrow Li_2S_4$. The prolonged exposure to the electrolyte results in Li_2S_4 becoming the predominant soluble species, as evidenced by the visualization results.

3.5.2 Galvanostatic charge (delithiation) process

During recharge Li_2S undergoes a multi-step reaction to be gradually oxidized back to zerovalent sulfur. The coexistence of Li_2S_x ($x \approx 4$) and Li_2S_x ($x \approx 6$) from 16% to 88% SOC is evidenced by their corresponding Raman signals. These two representative peaks reach their maximum intensity at ~60% SOC and then decay. At the same time, the EsB images at 30% SOC in **Figure 3-16a** show predominantly the presence of Li_2S_2/Li_2S. Minor instances of short and medium chain LiPSs can also be observed.

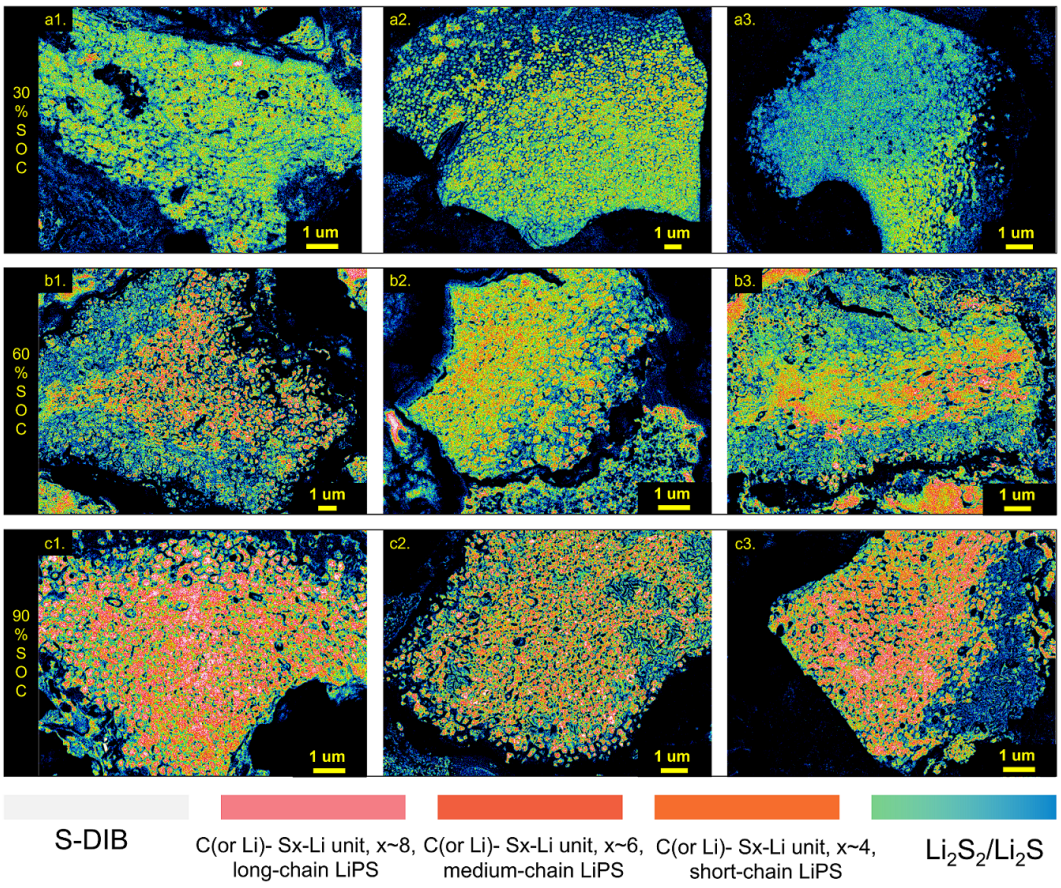

Figure 3-17 Heat map processed EsB image at (a) 30 % SOC (b) 60 % SOC (c) 90 % SOC. On the right is the colour gradient and its corresponding species.

It should be noted that Li_2S_2, as a metastable intermediate phase, plays a significant role in the initial charging.[13] Due to the instability of Li_2S_2, distinguishing between Li_2S_2 and Li_2S using alternative characterization methods is challenging. According to the working mechanism of the EsB detector, Li_2S appears darker than Li_2S_2. Therefore, regions of blue pixels in the heat map may be attributed predominantly to Li_2S, while green areas correspond mainly to Li_2S_2. The sporadic presence of short- and medium-chain LiPS in **Figure 3-17a** indicates that transformation from Li_2S_2 to Li_2S dominates the initial 30% of the charging process. It is reasonable to assume that Li_2S is first converted to Li_2S_2 before it is further oxidized to longer chain LiPS. Therefore, the activation of Li_2S must be considered the rate-limiting step compared to the oxidation of soluble LiPS which has high electrochemical activity and good mobility.

At 60% SOC, **Figure 3-17b** show that the majority of Li_2S/Li_2S_2 has transformed into short- and medium-chain LiPS, as evidenced by the faint ^{7}Li NMR spectra peak and faint S^{2-} XPS peak of Li_2S.

The amount of S_B^0 is approximately 2.1 times the amount of S_T^{-1}, indicating that the Li_2S_x ($x \approx 4$) and Li_2S_x ($x \approx 6$) coexist at 60% SOC. During the range of 30–60% SOC, the transformation of Li_2S_2 to Li_2S and from Li_2S_2/Li_2S to Li_2S_x ($x \approx 4$) and Li_2S_x ($x \approx 6$) still contributes to the capacity. With increasing SOC, bright areas appear again that can be assigned to S-DIB or elemental sulfur as in the section shown in **Figure 3-17c** at 90% SOC. Again, this matches the corresponding Raman spectra. The figures also show that the distribution of S-DIB inside the porous carbon is largely restored after the charging process is completed, and the internal structure of the carbon is preserved. However, in some parts shown in **Figure 3-17c3**, the inevitable loss of active material due to the shuttle effect was observed, explaining the capacity decay of up to 10 percent in the first cycle.

In summary, EsB imaging techniques were used to distinguish the lithiation and delithiation process of S-DIB at different SOCs and to gain new insights into the distribution of reaction intermediates in a porous carbon structure.

3.6 Cycling degradation

To elucidate the gradual capacity decline of S-DIB@HPC throughout the cycling process, EsB images of the electrodes were recorded after 200, 300, and 500 cycles, corresponding to capacity retention rates of 95%, 80%, and 60%, respectively. This analysis also aimed to assess the distribution of S-DIB within HPC and the volume expansion/contraction occurring during (de)lithiation. **Figure 3-18** show that all carbon cells are still filled with S-DIB and the structure of the carbon matrix remains intact after 200 cycles. After 300 cycles (**Figure 3-19**), some empty carbon pores and compressed carbon cells appear. Benefiting from the dual-confinement strategy, some carbon units not only maintain their structural stability, but no significant loss of their internal S-DIBs is observed after 500 cycles. (**Figure 3-20b and c**). However, the number of empty carbon cells continues to increase during cycling and after 500 cycles. **(Figure 3-20d**) More seriously, as shown in **Figure 3-20e−g**, the carbon structure collapses during prolonged cycling, and at these regions the S-DIB can be accommodated is also minimal. In comparison to the 200-cycle electrodes, the 500-cycle electrodes show a slight decrease in darkness in the brightest areas corresponding to regions of high S-DIB. This observation suggests a potential loss of sulfur or the simultaneous presence of inactivated Li_2S/Li_2S_2 in the electrodes.

XPS analysis of the cycled cathodes in **Figure 3-21** also demonstrates the loss of active material and the accumulation of Li_2S/Li_2S_2. The bridging sulfur peak decreases with an increase in the number of cycles. After 500 cycles, two new peaks at 160.2 eV are observed in the spectra of the electrodes, which can be attributed to sulfur in Li_2S_2/Li_2S.[118, 139] Furthermore, significant loss of active material and pronounced structural distortion resulting from the substantial volume expansion during cycling can be observed, as indicated by the arrow marks in **Figure 3-20**. This inevitably affects the charge transfer process at the interface between the HPC and electrolyte.

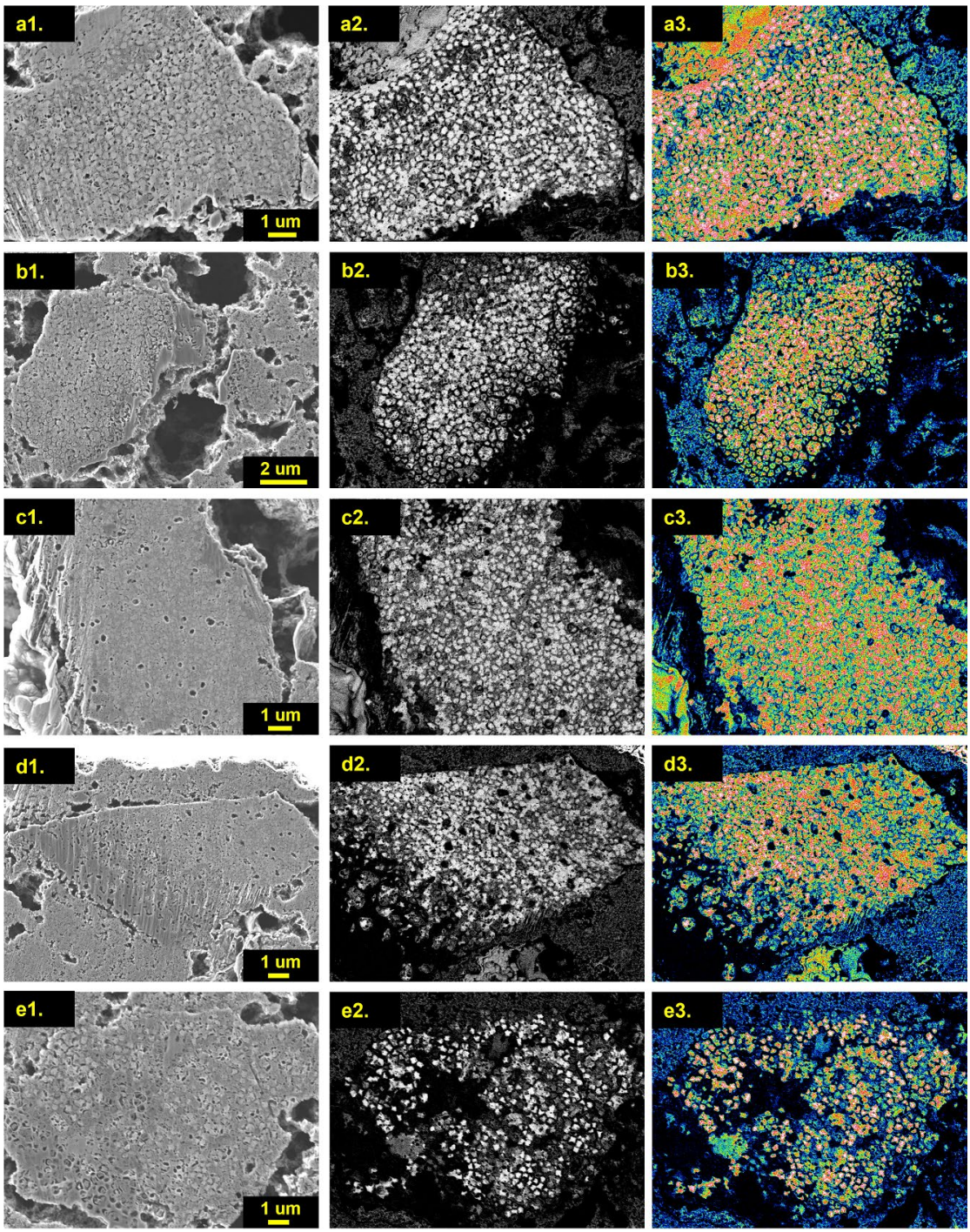

Figure 3-18 SE, EsB and the processed EsB images of the electrode after 200 cycles.

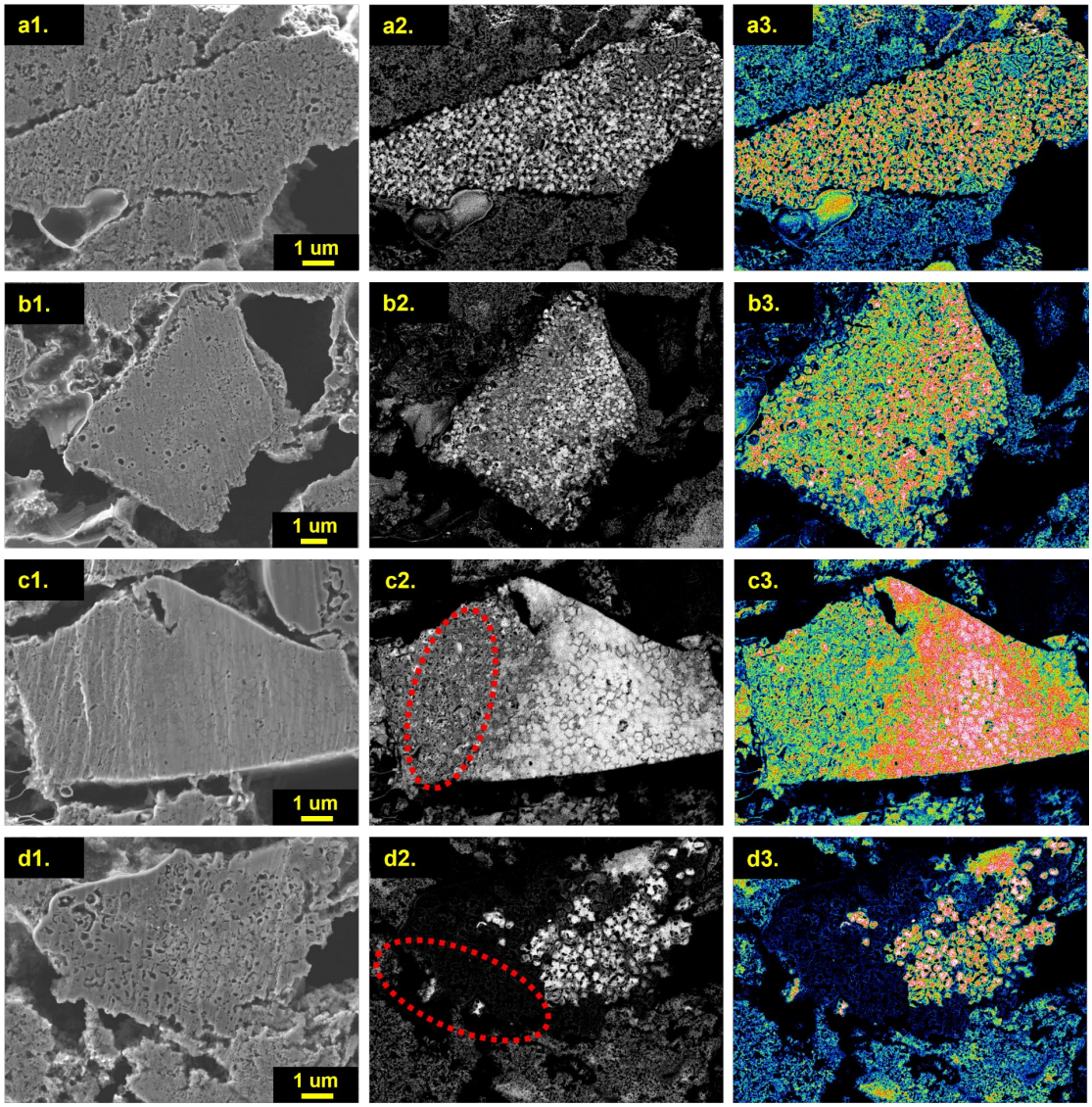

Figure 3-19 SE, EsB and the processed EsB images of the electrode after 300 cycles.

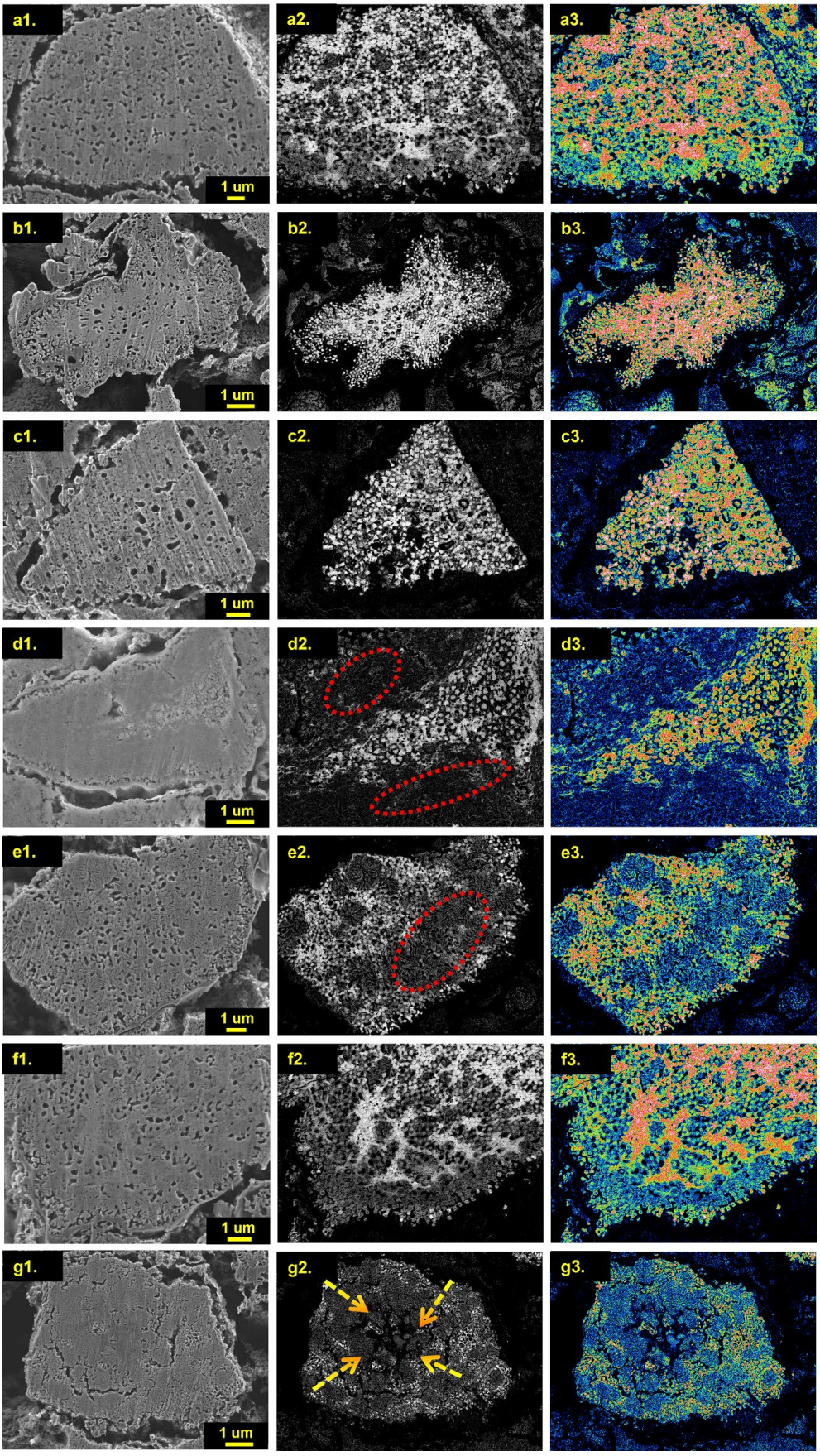

Figure 3-20 SE, EsB and the processed EsB images of the electrode after 500 cycles.

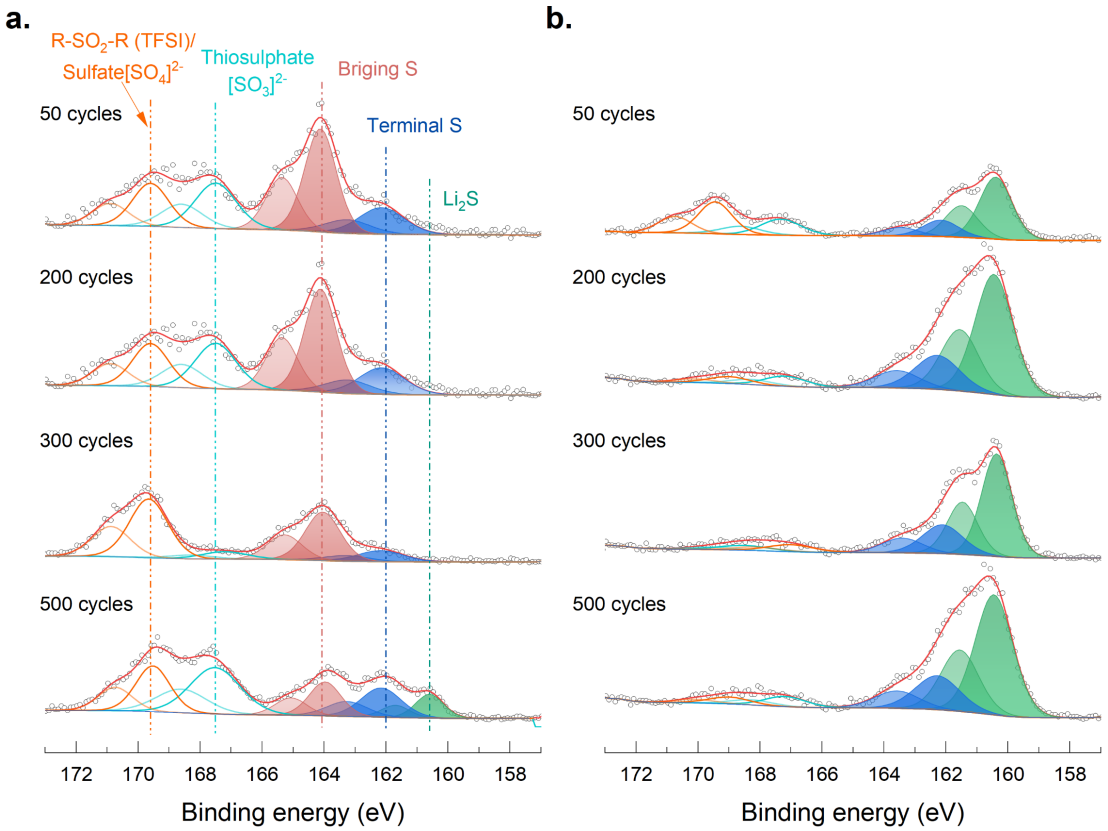

Figure 3-21 XPS of the S-DIB@HPC electrode after 50, 200, 300, and 500 cycles at (a) charged and (b) discharged state.

To establish a connection between the structural deterioration of the electrode and its impedance, electrochemical impedance spectroscopy (EIS) was employed. Data was gathered by measuring cycled electrodes in a three-electrode setup. **Figure 3-22a** depicts the impedance curves of a three-electrode system comprising a cycled cathode and an anode, with a fresh lithium electrode serving as the reference electrode. When the impedance spectra from the anode against the reference and the cathode against the reference are combined, they exhibit a high degree of agreement with the impedance spectra from the anode against the cathode. This indicates that impedance measurements in a three-electrode system can clarify the contribution of cathode and anode impedance to the total impedance. **Figure 3-22c** shows the impedance spectra of sulfur cathodes and anodes following the cycle. These were fitted using an equivalent circuit shown in **Figure 3-22b**.[140-142] The ohmic resistance is reflected in the circuit's resistance component (R_0). R_{int}//CPE_{int} represents the interphase contact resistance and its associated capacitance. It is used to simulate the conduction of electrons from the cathode collector to the reaction site. The charge transfer resistance and its associated capacitance are simulated by R_{ct}//CPE_{dl}. The plots of R_0, R_{int} and R_{ct} as a function of

cycle number are shown in **Figure 3-22d**. The trend observed for R_{ct} indicates its significant role during cycling. With longer cycling, the surface of the active mass becomes increasingly covered by insulating layers of Li_2S_2/Li_2S. Another factor contributing to the increase in R_{ct} is related to the degradation of HPC, since the charge transfer reaction occurs at the interface between the sulfur-containing carbon material and the electrolyte. As a result of the morphological distortions caused by changes and stresses within the cathode matrix, the interaction between the solid sulfur products and the dissolved species within the carbon matrix is no longer as efficient as it was at the beginning of the charging cycle. Despite the continuous degradation, HPC retains its role as an electrically conductive scaffold to some extent. Consequently, the sulfur composite electrode can be cycled for extended periods despite the evident morphological and structural alterations.

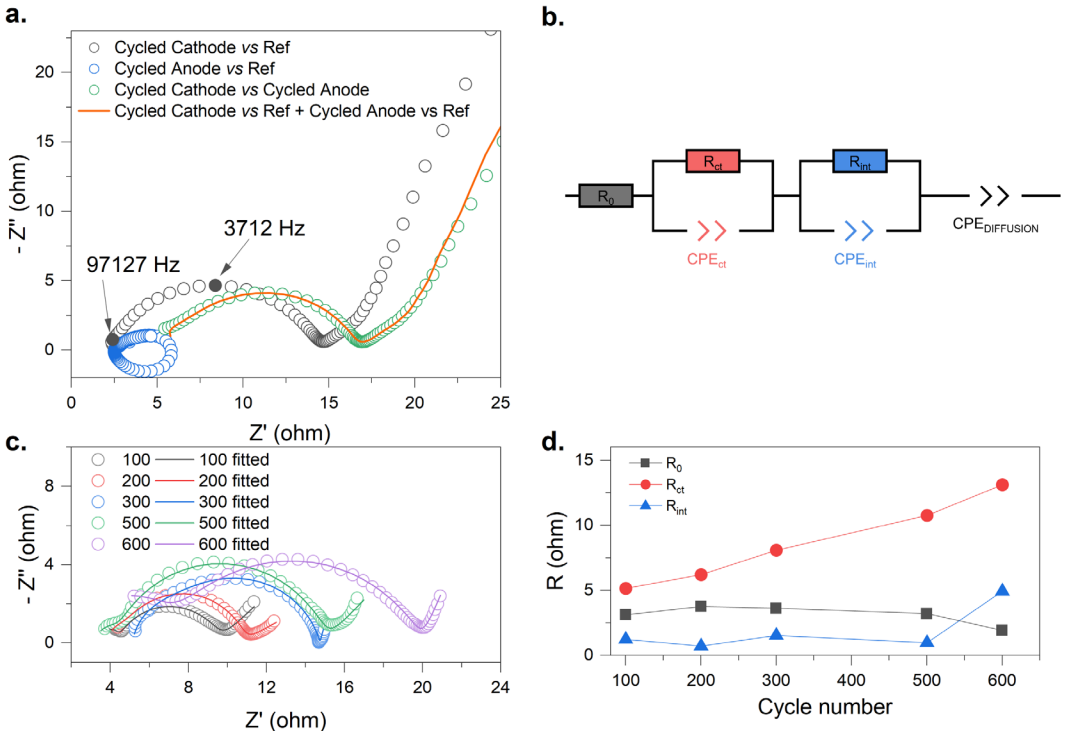

Figure 3-22 (a) Electrochemical impedance spectroscopy measured in a three-electrode system (b) The equivalent circuit which was used to fit EIS results. (c) EIS profiles and fitting profiles of cycled cathodes. (d) The plots of R_0, R_{int}, and R_{ct} as a function of cycle number.

To examine the chemical confinement of DIB and physical confinement of HPC on the shuttle effect, EsB images of S@HPC and S-DIB after cycling were also obtained. It is clear that the sulfur distribution in S@HPC is markedly lower than that of the S-DIB@HPC (**Figure 3-23**). This finding indicates that the porous structure of HPC cannot effectively confine LiPS in cathode. For the S-

DIB electrode, a direct comparation with S@HPC and S-DIB@HPC is not feasible as S-DIB exhibit bulk appearance (**Figure 3-24**). However, the considerable loss of active material before and after cycling can still be visualized, reflecting the beneficial role in the dual-confinement strategy (**Figure 3-25**). The three electrodes after cycling at charged stated were also characterized by XPS. As shown in **Figure 3-26**, in accordance with the findings regarding sulfur distribution in EsB, the peak of bridging S after cycling in S-DIB@HPC is markedly more intense than that of bridging S in the other two electrodes. Additionally, there is a greater concentration of unoxidized dead Li_2S in S@HPC and S-DIB than that in S-DIB@HPC.

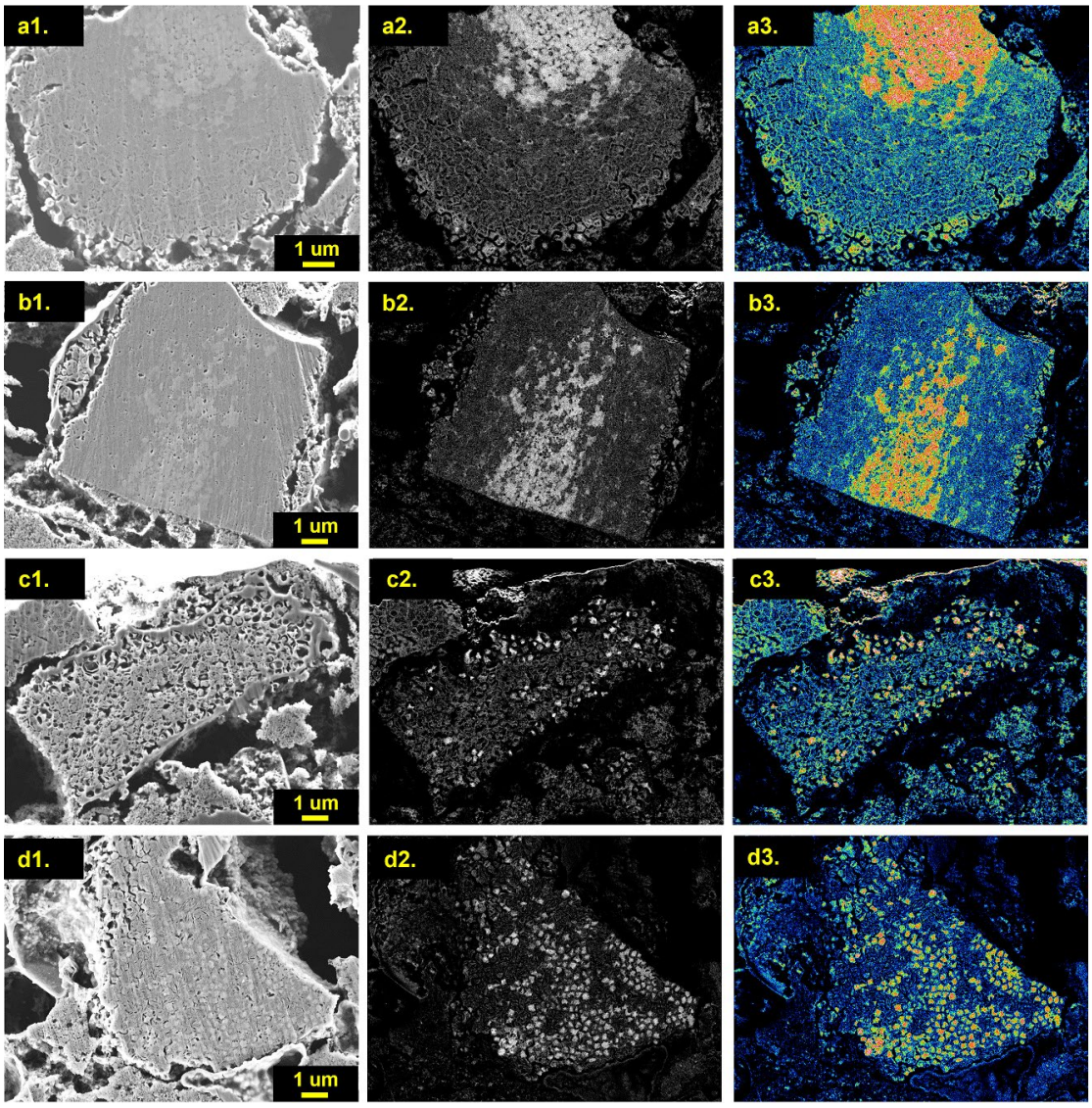

Figure 3-23 SE, EsB and the processed EsB images of the S@HPC electrode after 500 cycles.

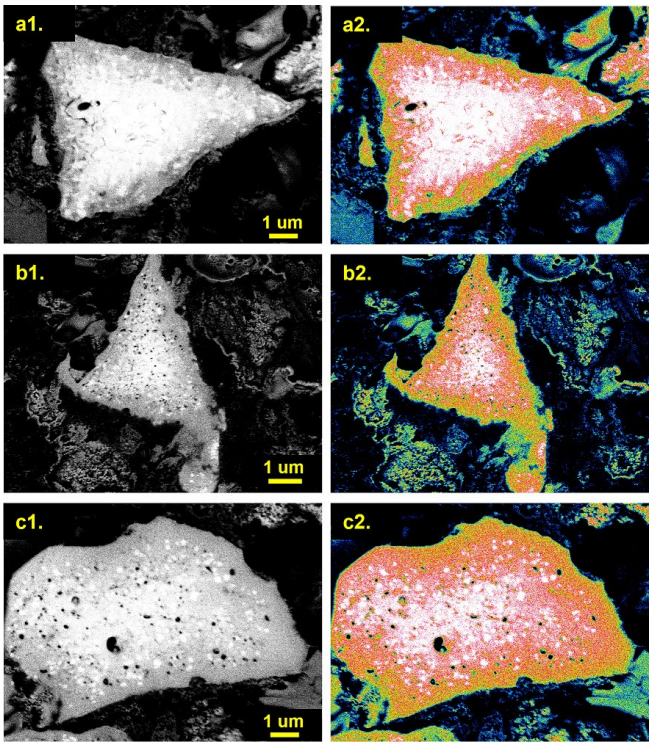

Figure 3-24 EsB and the processed EsB images of the S-DIB electrode.

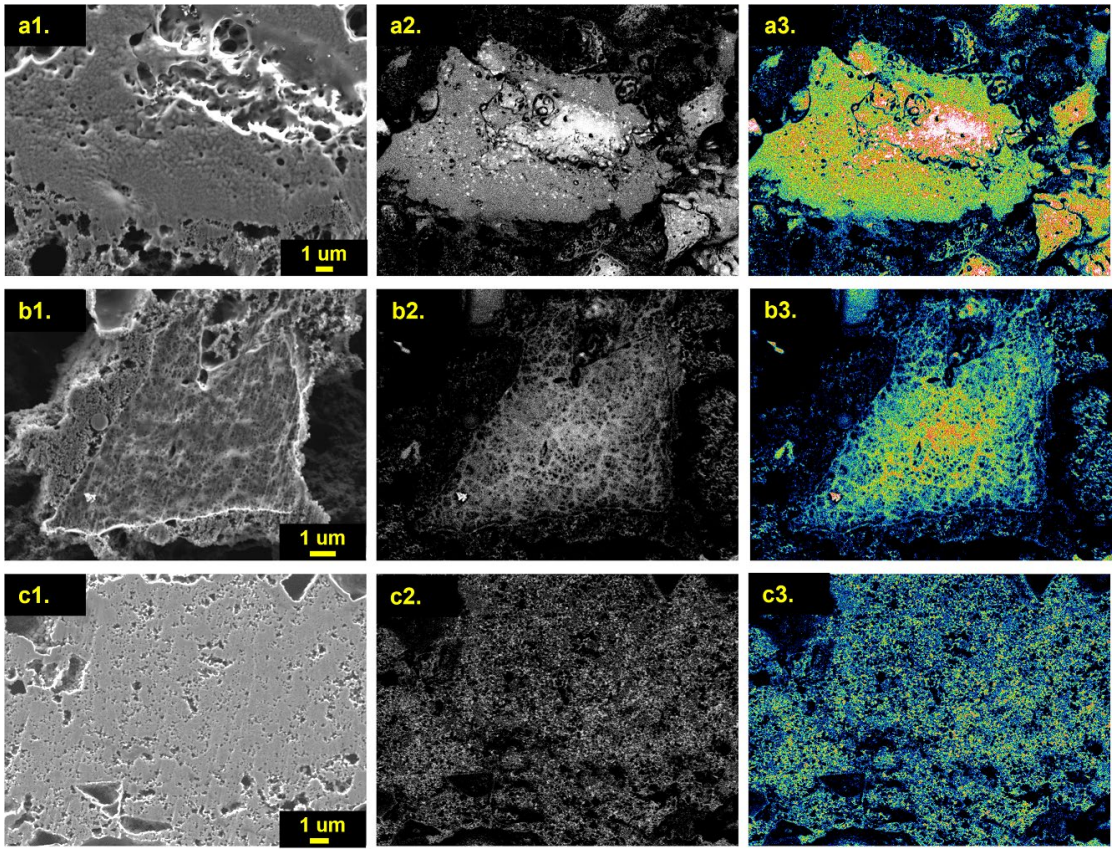

Figure 3-25 SE, EsB and the processed EsB images of the S-DIB electrode after 500 cycles.

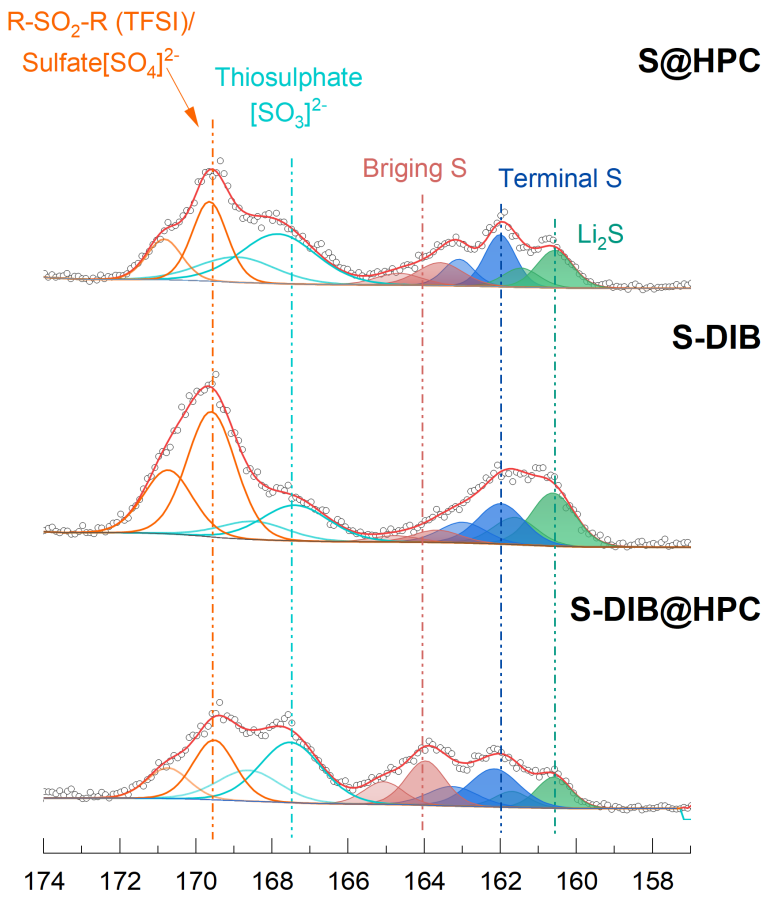

Figure 3-26 XPS of the electrode after 500 cycles at charged state.

In conclusion, EsB imaging was employed for the first time to reveal both the accumulation of lithium sulfide during cycling and the degradation of the carbon scaffold. Furthermore, a correlation with the impedance results of the sulfur cathode has also been established.

3.7 Conclusion

To summarize, we have successfully developed a novel carbon structure that accommodates the IV inverse vulcanization reaction, resulting in a well-distributed S-DIB within an interconnected carbon framework. This system effectively regulates the distribution of S-DIB and suppresses the shuttle effect through both physical and chemical confinement. Consequently, S-DIB@HPC maintains a high capacity after 500 cycles, with a capacity decay of only 0.04% when used as a sulfur cathode. Additionally, the ordered structure provides a beneficial platform for studying the evolution of S-DIB from a cross-sectional perspective.

The EsB detector can capture the morphology and differentiation of sulfur, Li_2S, and intermediates

during the de/lithiation process. Combined with Raman, XPS, and NMR spectroscopy results, we observe a gradual reduction of S-DIB to Li_2S_6, then to Li_2S_4, and subsequently to Li_2S_2/Li_2S during discharge. During charging, Li_2S and Li_2S_2 are oxidized to Li_2S_2 and Li_2S_6, ultimately converting back to S-DIB. The phase transitions from liquid to solid (Li_2S deposition during discharge and the oxidation of LiPS to solid-phase S-DIB during charging) exhibit the slowest kinetics in the entire sulfur redox process.

Both DIB and porous carbon work together to confine the shuttle effect. However, the gradual loss of active materials still leads to a decrease in capacity during cycling. Additionally, the carbon host may degrade and distort due to volumetric changes between S and Li_2S, resulting in increased charge transfer resistance.

3.8 Characterization details

DSC was performed on a 214 Polyma DSC device from NETZSCH (Selb, Germany). Around 5 mg of sample were precisely (Δ = 0.005 mg) weighed in an aluminum pan with a pierced lid for measurement. An aluminum pan filled with air was used as a reference and the heating rate was typically set to 10 K min^{-1} for all measurements. TGA was carried out on an STA 449C Jupiter instrument (NETZSCH, Germany). All TGA measurements were done in argon atmosphere from room temperature to 400 °C with a constant heating rate of 5 K per minute and an argon flow.

EsB-assisted SEM: In this work, cross-sections of electrodes were prepared using the broad argon ion beam slope-cutting and polishing system, GATAN PECS II. Electrodes were ion-polished by Ar beam under an acceleration of 6 kV for 8 h. The modulation was set to “Single”. The whole process was conducted under vacuum or Ar atmosphere to avoid oxidation. The polished electrodes were analyzed in an SEM (Zeiss Gemini 2). The ion-polished electrodes were transferred to the SEM chamber using a shuttle tool under the protection of inert gas. the EsB was set to 1500V = 0.6 Ep (Primary beam energy). Working distance (3.8 mm), beam current (600 pA) and other parameters were kept constant while capturing the images to avoid their influence on the brightness of the images.

XPS was performed using a K-Alpha$^+$ instrument (Thermo Fisher Scientific) with a monochromatic

Al-Kα X-ray source (1486.6 eV). The sample storage and transportation to the spectrometer for XPS characterization were carried out in an airtight transport vessel under Ar. Thermo Avantage software was used to perform data acquisition and processing as described elsewhere.

Raman measurement: A LabRAM HR Evolution spectrometer (HORIBA scientific), equipped with a HeNe laser (λ = 632.8 nm, E_{laser} = 1.9876 eV). A 600 grooves mm^{-1} grating along with a 50× magnification (NA = 0.5) objective was employed, resulting in a spot size of about 2 μm.

^{7}Li magic-angle spinning (MAS) NMR spectroscopy experiments were conducted on a Bruker Avance 200 MHz spectrometer at a magnetic field of 4.7 T. Spectra were acquired at a Larmor frequency of 77.8 MHz with 1.3 mm rotors and spinning at 60 kHz. A rotor-synchronized Hahn-echo pulse sequence (90°-τ–180°-τ-acquisition) was used with a 90° pulse length of 0.9 μs and a recycle delay of 1 s. The ^{7}Li NMR spectrum shifts were referenced using an aqueous 1 M LiCl solution (0 ppm). All spectra were normalized with respect to sample mass and number of scans.

The surface area and pore size distribution were analyzed by N_2 adsorption/desorption isotherms obtained at 77 K with a Micromeritics ASAP 2020 instrument.

4 Functionalized Pyrene Modified HPC Enhances Sulfur Redox Kinetics

In Chapter 3, a composite with evenly distributed S-DIB in the HPC matrix was explored, showcasing its cycling stability. However, there is room for improvement in its initial capacity and rate performance. This issue likely originates from the limited interaction between the rather unpolar surface of the carbon material and the polar LiPS species. This weak interaction hinders the phase transition from liquid to solid (LiPS to Li_2S_2/Li_2S) at the carbon material's surface and limits the suppression of LiPS shuttling to mere physical obstruction.[143, 144]

To address this issue, various methods have been employed to enhance the surface polarity of carbon materials. However, these modifications can degrade the carbon structure. For instance, acid treatments can damage the carbon structure if not carefully controlled,[145, 146] and plasma exposure can create surface roughness or defects, negatively impacting the carbon's mechanical properties.[147, 148] Additionally, these methods often lack precision in introducing specific functional groups, complicating the understanding of their effects on sulfur redox kinetics.

Pyrene and its derivatives, known for being π-electron-rich acceptors, can self-assemble and anchor to carbon through π-π stacking interactions.[149-151] This non-destructive modification preserves the host's conductivity, structure, and porosity.[152, 153] Pyrene also allows for various functionalizations through substitutions. In this chapter, we discuss modifications using functionalized pyrene on the HPC introduced in Chapter 3. The modified carbon was then used as a reactor for inverse vulcanization to improve sulfur utilization and reduce the shuttle effect. The impact of functionalized pyrenes on Li_2S precipitation and the inhibition of the shuttling effect was analyzed using electrochemical results, *operando* XRD, and EsB techniques.

4.1 Experimental details

4.1.1 Synthesis of materials

Synthesis of py-HPC and X-py-HPC (X = Br, OH, NH_2): To synthesize pyrene-modified carbon, 200 mg of HPC was added to a 5 mM solution of the corresponding pyrene in 10 mL of DMSO.

After stirring overnight, the mixture was filtered and thoroughly washed with DMSO and deionized water. The residue was then dried under vacuum to obtain pyrene modified carbon.

Synthesis of S-DIB@HPC, S-DIB@py-HPC, S-DIB@X-py-HPC composites: A mixture of 700 mg and 180 mg of the corresponding carbon was combined and placed in a sealed glass vial. The mixture was heated in an oil bath to 155 °C and then held for 5 minutes and further heated to 185 °C. Subsequently, 120 mg of 1,3-Diisopropenylbenze (DIB) was added while stirring, and the reaction continued for about 15 minutes until completion.

4.1.2 Electrochemical measurements

The assembly process and the CV, GCPL, and GITT measurement details of coin cells are the same as described in Chapter 3.

Assembly and CV measurement of symmetric cells: A Li_2S_6 solution (0.25 mol L^{-1}) was prepared by mixing Li_2S and sulfur (with a molar ratio of 1:5) in 1,3-dioxolane and 1,2-dimethoxyethane containing 1 mol L^{-1} lithium bis(trifluoromethanesulfonyl)imide. The symmetric cell was assembled with pyrene modified carbon electrodes as both cathode and anode and 30 uL Li_2S_6 solution as electrolyte. CV measurements were performed at a scan rate of 10 mV s^{-1} between –1 and 1 V.

Nucleation test of Li_2S: A Li_2S_8 solution (0.25 mol L^{-1}) was prepared by combining sulfur and Li_2S powder at a molar ratio of 7:1 in DOL/DME (1:1 in volume) under vigorous stirring for 24 h. The cell was assembled using a piece of lithium foil as the counter electrode and a pyrene-modified carbon electrode as the cathode. 20 μL Li_2S_8 (0.25 M) solution was dropped on the cathode side, and 20 μL of blank electrolyte was dropped on the anode side. For the nucleation of Li_2S on different carbon cathodes, the cells were firstly galvanostatically discharged at 112 uA to 2.06 V and then kept at 2.05 V until the current was below 10 uA.

4.1.3 Characterizations

XPS Analysis:

XPS were obtained using a Thermo Scientific K-alpha+ spectrometer. Powders were fixed on silicon wafers with adhesive carbon tape and analyzed using a micro-focused, mono-chromated Al Kα X-ray source (1486.6 eV, spot size 400 μm). Spectra were recorded with a concentric hemispherical analyzer at a pass energy of 50 eV for detailed spectra and 200 eV for survey spectra. During analysis, the K-Alpha charge compensation system was employed, using 8 eV electrons and low-energy argon ions to prevent localized charge build-up. Quantification and peak fitting were performed using the Thermo Avantage software package. All detailed spectra used a Shirley background function and were referenced to the sp^2 peak of C 1s at 284.4 eV. The asymmetry of the sp^2 peak was evaluated with a tail mix of 70 to 90% and a tail exponent of 0.04 to 0.06, considering a smaller FWHM of 0.8 to 1.12. Other peaks were fitted using mixed Gaussian-Lorentzian peak shapes with FWHM values between 1.3 and 1.5 for C 1s components (CC/CH, C–O, O=C–O) and 1.96 to 2.3 for O 1s components.

Synchrotron based *operando* XRD experiments

Operando XRD experiments were performed at the MSPD beamline at ALBA synchrotron in Barcelona, Spain, using a photon energy of 30 keV (λ = 0.4130 Å). Diffraction patterns were acquired with a MYTHEN-2 position-sensitive detector, with an exposure time of 60 seconds per pattern. CR2032 coin cells with glass windows (diameter = 5 mm) were assembled and discharged from OCV (≈ 2.7 V) to 1.7 V with the current of C/20 (1C = 1675 mAh g^{-1}) at room temperature using a Biologic VMP3 multichannel potentiostat.

Details of DSC, TGA, and Raman measurements can be found in Chapter 3.

4.2 Pyrene modification

The π-π interaction is a unique type of non-covalent interaction driven by van der Waals forces.[154] This interaction allows for the creation of highly uniform pyrene-HPC composites through the interaction between pyrene and the flat surfaces of HPC. Theoretically, various atoms or groups can be attached to a pyrene molecule via a substitution reaction.[155, 156] As a result, functionalized pyrene can be adsorbed onto the surface of porous carbon through π-π stacking, making its functional groups available for studying their effects on sulfur redox reactions.[157]

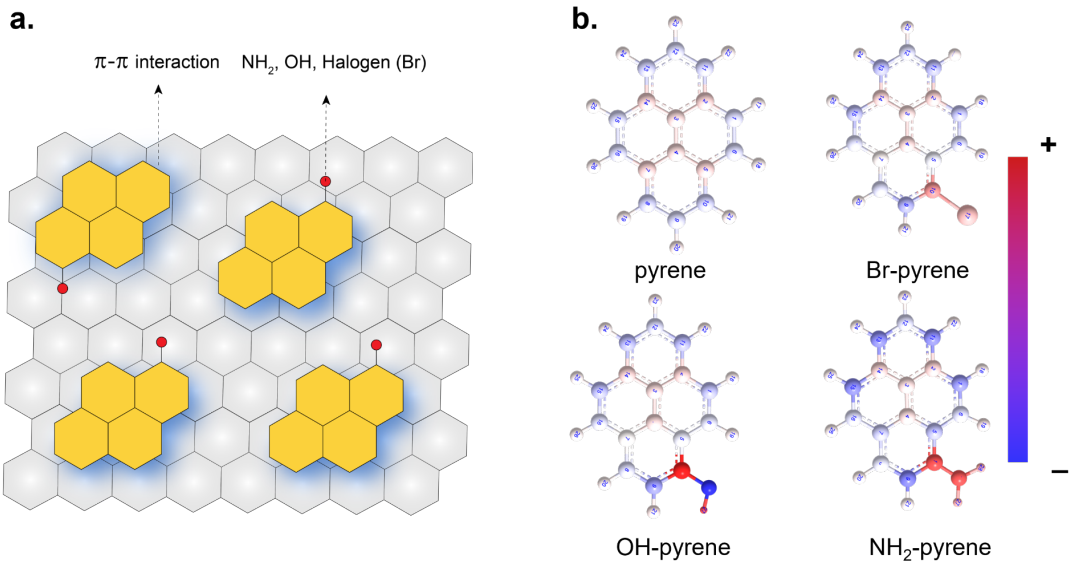

Figure 4-1 (a) The scheme of pyrene modification and introduced polar groups (b) Charge distribution of pyrene and functionalized pyrene molecules.

In this study, as shown in **Figure 4-1a**, pure pyrene and X-pyrene (X = Br, OH, and NH_2) were chosen to modify HPC. The symmetrical arrangement of fused benzene rings gives pyrene an even electron density distribution, making pure pyrene non-polar. **Figure 4-1b** illustrates the charge distribution of pyrene and its functionalized derivatives. The central carbon atoms in a non-polar pyrene molecule exhibit slight electronegativity, while the surrounding carbon atoms connected to hydrogen atoms show slight electropositivity due to carbon-hydrogen bonding. In the OH-pyrene molecule, the carbon atom connected to the hydroxyl group exhibits a positive charge due to the electronegative oxygen. The induction effect causes surrounding carbon atoms to show slight negativity. Unlike OH-pyrene, the lone pair electrons of the nitrogen atom in NH_2-pyrene prefer to form a p-π conjugation with the pyrene ring. Resonance influences cause surrounding carbon atoms to show more negativity than in OH-pyrene, reducing local charge accumulation.[158, 159] Hence, these non-electroneutral pyrenes were selected to study their effect on the sulfur reduction reaction and their ability to retain LiPS. Given that HPC contains carbon, nitrogen, and oxygen elements, Br-pyrene was selected as a modifier because it can be distinctly characterized by XPS and EDX, proving the effectiveness of surface adsorption and distribution.

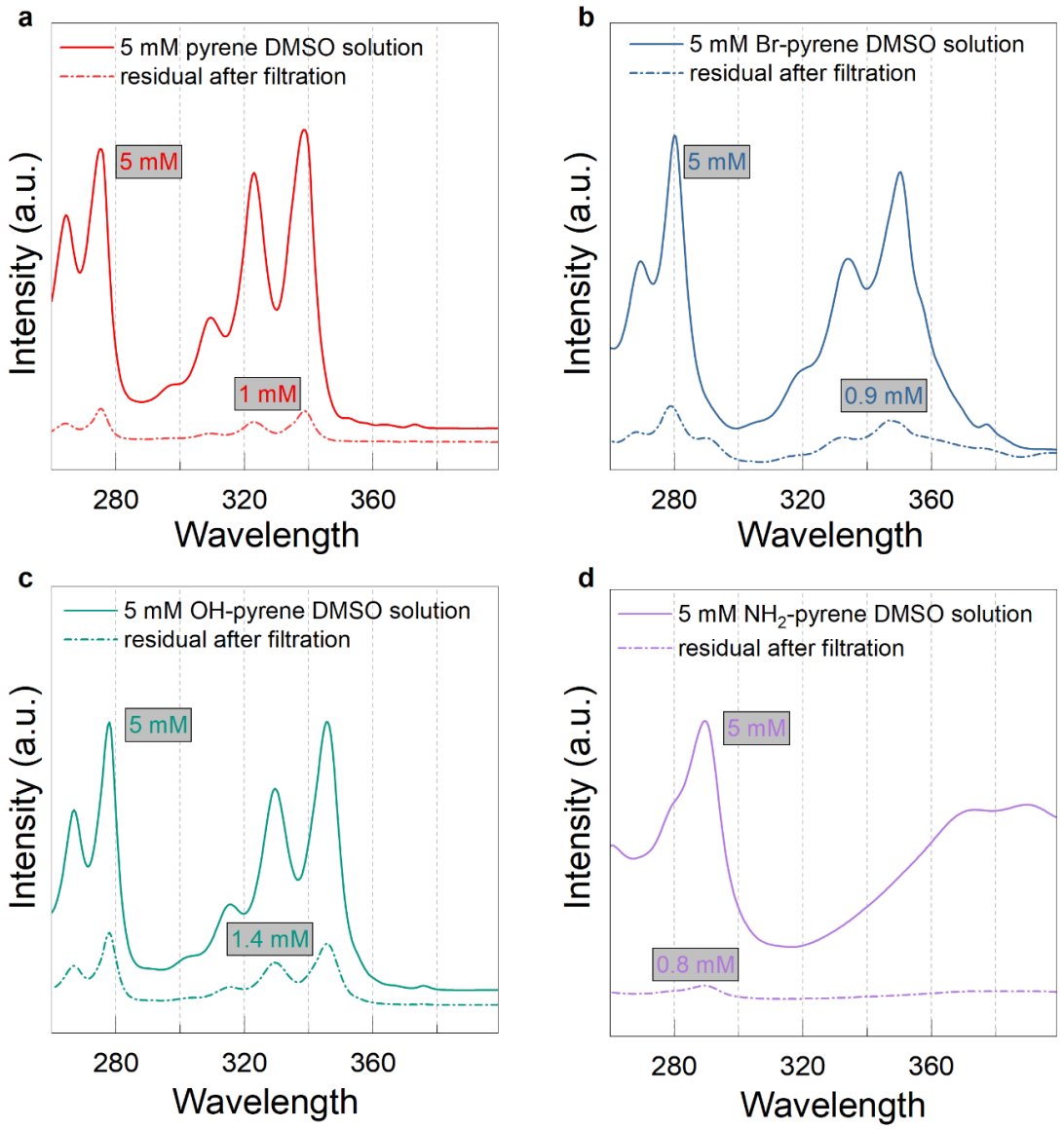

Figure 4-2 The UV-VIS results of the original pyrene DMSO solution and the filtrate.

The pore structure of synthesized HPC allows for the adsorption of pyrene molecules onto its large surface through π-π stacking interactions. The adsorption efficiency is validated by comparing the UV-VIS peak intensity of the adsorption filtrate with that of the original pyrene/DMSO solution. The concentration in the filtrate is approximately 1 mM for pyrene, 1.1 mM for Br-pyrene, 1.4 mM for OH-pyrene, and 0.8 mM for NH_2-pyrene, compared to the initial concentration of 5 mM before adsorption (**Figure 4-2**). Therefore, the adsorption efficiency of HPC for different pyrene compounds shows slight variations but remains above 70%. The EDX spectra and mapping results in **Figure 4-3** demonstrate the presence and uniform distribution of Br in Br-py-HPC. It can be reasonably inferred that other pyrene derivatives are also evenly dispersed on the carbon surface. Furthermore, the morphology of the pyrene-modified carbon particles is unchanged compared to

non-modified HPC (**Figure 4-4**).

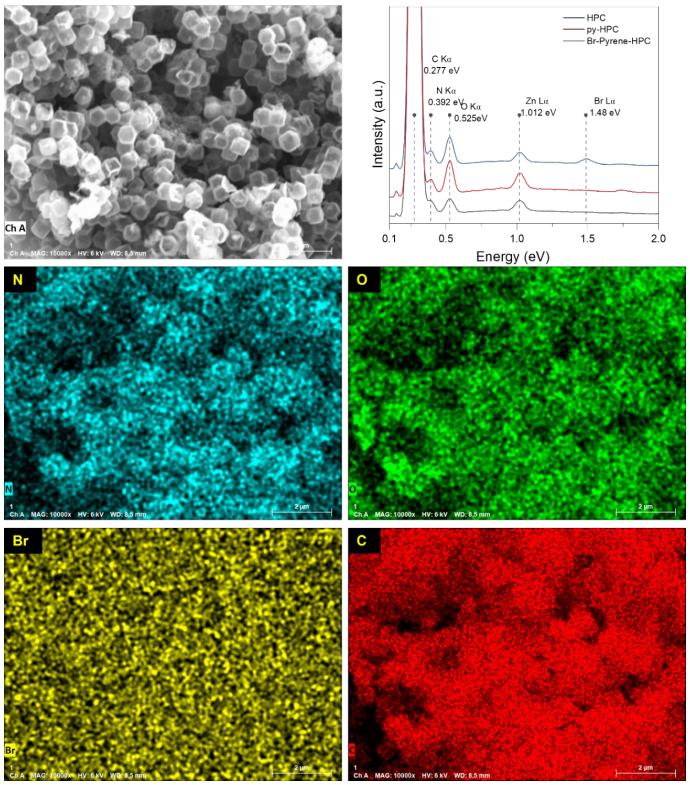

Figure 4-3 EDX spectra and mapping results of Br-HPC.

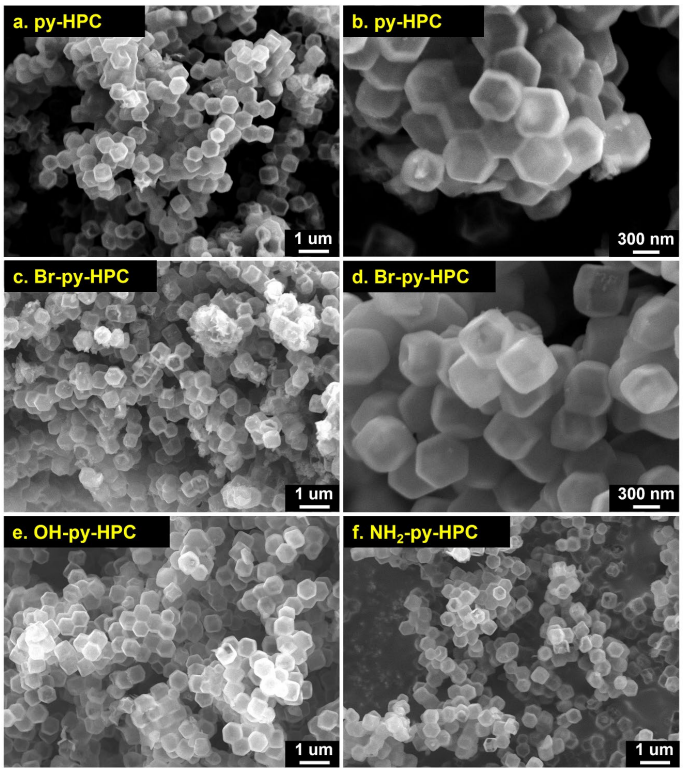

Figure 4-4 SEM images of py-HPC (a–b), Br-py-HPC (c–d), OH-py-HPC (e) and NH_2-py-HPC (f).

4.3 Surface properties of pyrene modified HPC

XPS was used to investigate the surface chemical makeup of the HPC carbon materials. As shown in **Figure 4-5a**, all samples, except Br-py-HPC which has an extra bromine peak, show three main peaks for carbon, oxygen, and nitrogen. The high-resolution Br 3d spectrum in **Figure 4-5b** reveals a doublet peak at 67.8 eV (3d 5/2) and 68.7 eV (3d 3/2), indicating the presence of the desired group introduced by X-pyrene. **Figure 4-5c** shows the C 1s peaks of all samples, which are deconvoluted into five peaks at 284.46, 285.06, 286.46, 288.86, and 290.76 eV. These peaks correspond to sp^2 hybridized carbon atoms (C–C), sp^3 hybridized carbon atoms (defect peak), C–O, C=O, and shake-up π–π* satellite peaks.[38] The proportions of these components are similar across all samples, indicating that the native carbon structure remains unchanged after pyrene modification. XPS also helps identify the introduced hydroxyl (OH) and amino (NH_2) groups, distinguishing them from the oxygen and nitrogen already present in HPC. The high-resolution N 1s spectra of both HPC and NH_2-py-HPC show two main nitrogen functional group peaks: pyridinic-N and pyrrolic-N at 398.2 and 399.2 eV, respectively.[130, 131] However, due to the small amount introduced by pyrene, there is no significant difference in the deconvoluted oxygen peaks between NH_2-py-HPC and HPC (**Figure 4-5d**). Similarly, no notable difference is observed in the deconvoluted oxygen peaks between OH-py-HPC and HPC (**Figure 4-5e**).

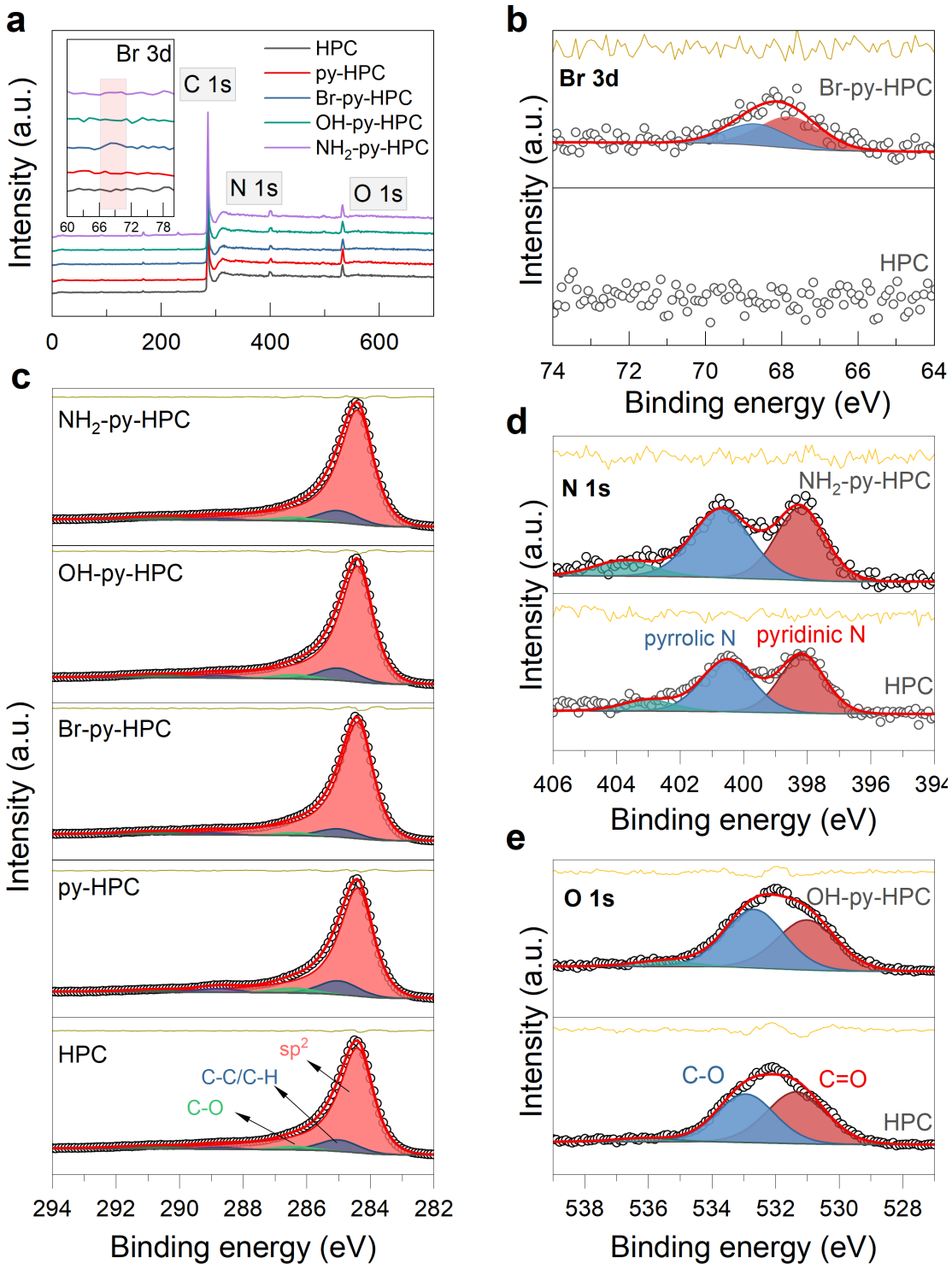

Figure 4-5 (a) Survey XPS of all carbon samples. (b) C 1s spectra of all carbon samples. (c) Br 3d spectra of HPC and Br-py-HPC. (d) N 1s spectra of NH_2-py-HPC. (e) O 1s spectra of OH-py-HPC and HPC.

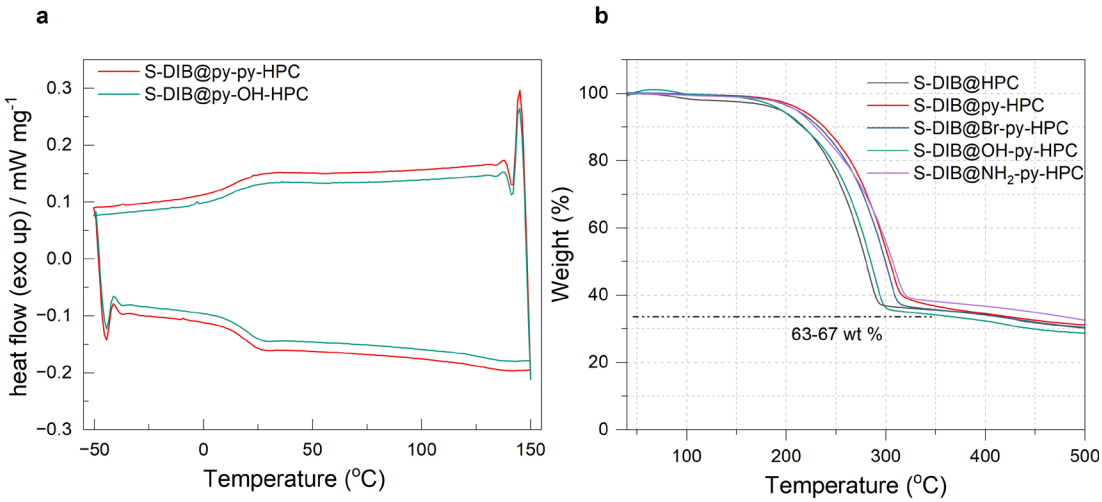

Figure 4-6 (a) DSC profiles showing the glass transition temperature around 15−20 °C for S-DIB@py-HPC and S-DIB@OH-py-HPC, indicating successful polymerization. (b) TGA profiles illustrating weight loss and sulfur content of approximately 65 wt% in the composites.

HPC and pyrene-modified HPC were used as reactors for the inverse vulcanization reaction with DIB. The successful synthesis of S-DIB is confirmed through DSC measurements, as shown in **Figure 4-6a**. DSC profiles of S-DIB@py-HPC and S-DIB@OH-py-HPC show no significant melting peaks but display a glass transition temperature around 15 °C. This indicates that all crystalline sulfur has been polymerized and linked by DIB and is uniformly distributed on the HPC and X-py-HPC.[67] The sulfur loading of all composites is approximately 65 wt% as determined by TGA results (**Figure 4-6b**).

4.4 The catalytic effect of polar groups on sulfur redox reactions

To evaluate how effective functionalized pyrenes are in reducing the shuttle effect and enhancing phase transitions in Li−S batteries, symmetrical cells using the same host materials for both the cathode and anode were assembled. In these cells, the oxidation of Li_2S_6 (dissolved in the electrolyte) to Li_2S on one electrode is balanced by its reduction on the opposite electrode.[160] This setup allows to analyze the catalytic activity of the pyrene modified electrodes, reflected by the peaks in the CV, and study their effect on LiPS oxidation and reduction. As illustrated in **Figure 4-7**, all electrodes show four distinct redox peaks in their CV profiles, representing the steps in the LiPS conversion process. Specifically, Peak A in the first cathodic scan corresponds to the reduction of Li_2S_6 to Li_2S/Li_2S_2 on the working electrode. Unlike py-HPC, OH-py-HPC and Br-py-HPC display a split Peak A, indicating different redox mechanisms under the influence of X-pyrene. During the reverse

anodic scan, Peak B corresponds to the oxidation of Li_2S/Li_2S_2 back to Li_2S_6. Peak C corresponds to the oxidation of Li_2S/Li_2S_2 to Li_2S_6 and sulfur on the working electrode. Peak D represents the reduction of sulfur on the working electrode to Li_2S_6.[161]

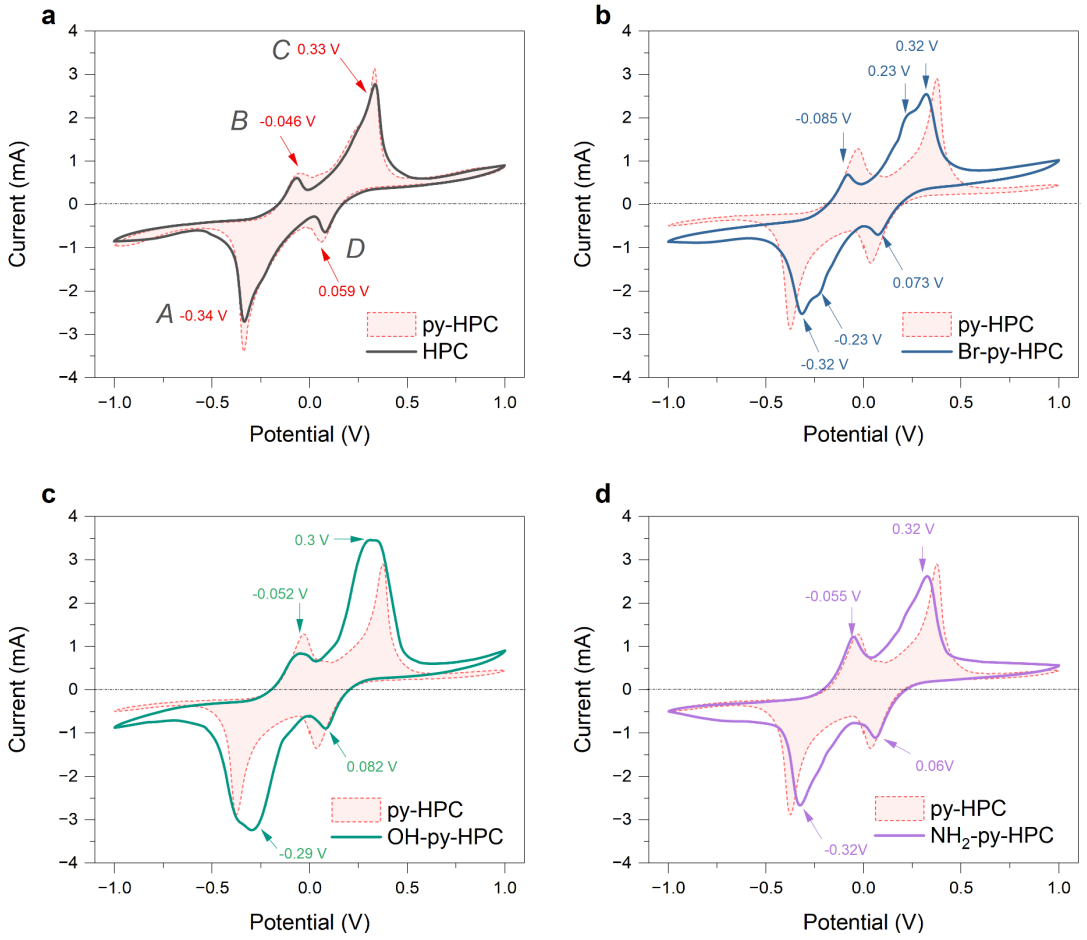

Figure 4-7 CV curves of symmetric batteries with Li_2S_6 dissolved in DOL/DME (v/v = 1/1) as electrolyte using HPC, Br-py-HPC, OH-py-HPC and NH_2-py-HPC as working and counter electrodes, with py-HPC as a reference.

Both OH-py-HPC and NH_2-py-HPC exhibit higher reduction potentials and lower oxidation potentials for LiPS compared to py-HPC and pure HPC, indicating that these functionalized pyrenes can facilitate LiPS conversion with lower polarization and faster kinetics. Notably, the OH-py-HPC electrode also shows the largest area of peak A, suggesting a significant catalytic effect on the precipitation of Li_2S_2/Li_2S. This catalytic effect is further investigated by the Li_2S/Li_2S_2 precipitation measurements using potentiostatic discharge/charge tests. The Li–S cells, utilizing an electrolyte of 0.25 mol L^{-1} Li_2S_8, underwent a discharge process to reach a voltage of 2.06 V under a constant current. Subsequently, they were discharged at a constant voltage of 2.05 V to promote the nucleation and growth of Li_2S. As shown in **Figure 4-8**, OH-py-HPC facilitates the Li_2S

precipitation with accumulated capacities as high as 172 mAh g^{-1}, slightly higher than NH_2-py-HPC, and greatly larger than for Br-py-HPC (149 mAh g^{-1}), py-HPC (108 mAh g^{-1}), and HPC (117 mAh g^{-1}). These findings align with the results obtained for symmetric cells, indicating that the functionalized pyrenes can enhance the nucleation and growth of Li_2S. There are two primary mathematical models for electrochemical deposition: the Bewick–Fleischman–Thirsk model, which describes two-dimensional (2D) growth, and the Scharifker–Hills model, which explains three-dimensional (3D) growth. Both models are categorized into progressive (P) type, characterized by a slow nucleation rate, and instantaneous (I) type, characterized by a high nucleation rate. The 2DI and 2DP models adhere to the 2D nucleation mechanism, where crystallite growth is controlled by the incorporation of nearby adatoms into the lattice. In contrast, the 3DI and 3DP models result in growth within a 3D hemispherical nucleus, with the growth rate governed by ion diffusion.

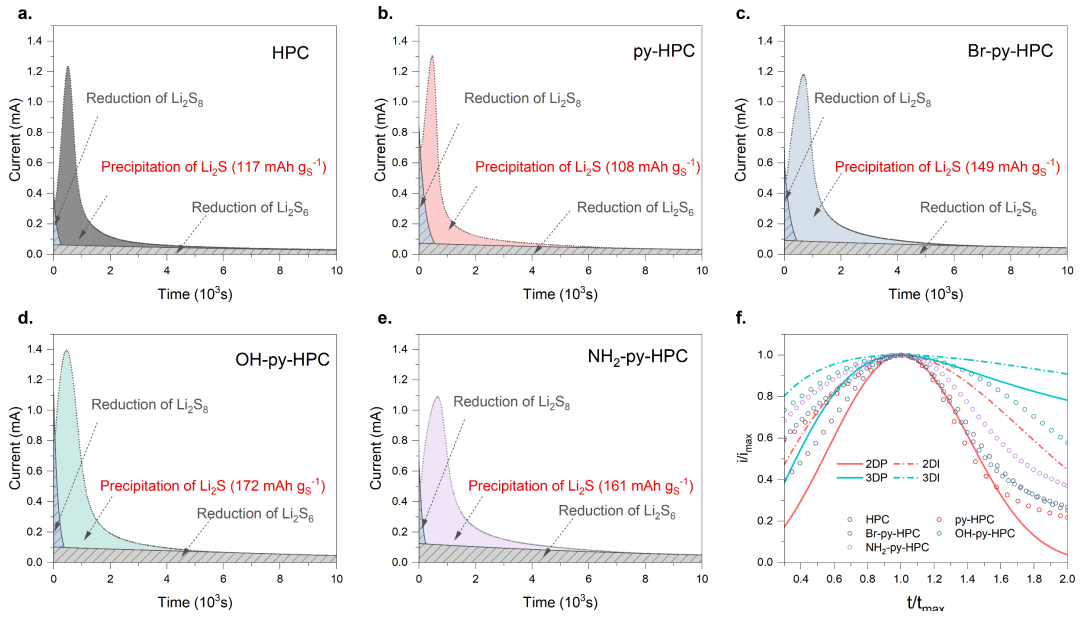

Figure 4-8 Li_2S precipitation profiles of HPC and pyrene modified HPC. Dimensionless transient (symbols) of different samples in comparison with theoretical 2D and 3D models (lines). (i_{max}: peak current; t_{max}: time needed to achieve the peak current)

Based on the fitting results for Li_2S nucleation behavior, when projected onto the dimensionless current–time transients, expressed as the relationship between i/i_{max} and t/t_{max} for each model, it is possible to determine the morphology of Li_2S formed on the various carbon substrates (**Figures 4-8f**). Li_2S growth on HPC, py-HPC and Br-HPC follows a 2DP model. In contrast, the Li_2S growth on OH-py-HPC exhibits a 2DI and 3DP hybrid model, while on NH_2-py-HPC it shows a 2DP and

2DI hybrid type, respectively. This transition indicates that the NH_2 groups can act as catalytic sites, promoting instantaneous nucleation and dense Li_2S growth. The rapid deposition of Li_2S on OH-py-HPC also ensures also ensures sufficient solubility in the electrolyte, enabling 3D growth.

To better understand deposition models of Li_2S and the role of the OH group in enhancing this process, *operando* XRD measurements were performed on py-S-DIB@py-HPC and S-DIB@OH-py-HPC cathodes (**Figures 4-9b** and **4-9e**). The deposition Li_2S model on the surface of py-HPC is typically 2DP while on OH-py-HPC, it is a combination of 2DI and 3DP. The discharge current was set to C/20 to ensure a comprehensive reaction, corresponding discharge curves are shown in **Figures 4-10a** and **4-10d**. Detailed spectra views focusing on diffraction angles between 6-8 degrees and 10-14 degrees are presented in **Figures 4-10c** and **4-10f**. In the first 15% of the depth of discharge (DOD), the S-DIB peak diminishes in both cathodes, indicating a quick conversion to LiPS. Differences between the cathodes become evident during Li_2S precipitation, with peaks at 7.2° and 11.8° corresponding to the (111) and (220) planes (ICSD−56023).[162] For S-DIB@OH-py-HPC, Li_2S is detected immediately at the start of the second discharge plateau. In contrast, the Li_2S peak in S-DIB@py-HPC appears gradually, becoming noticeable at 60% DOD. The more rapid Li_2S formation in S-DIB@OH-py-HPC is likely due to the catalytic effect of the polar group, facilitating the direct conversion of Li_2S_4 to Li_2S. Consequently, Li_2S is detected right after the second plateau. For S-DIB@py-HPC, Li_2S_4 first transitions to Li_2S_2 or a mixture of Li_2S_2/Li_2S, with Li_2S only appearing in the latter half of the discharge. This highlights the catalytic role of functionalized pyrenes in accelerating the liquid-solid transformation of LiPS, leading to a fast conversion to Li_2S.

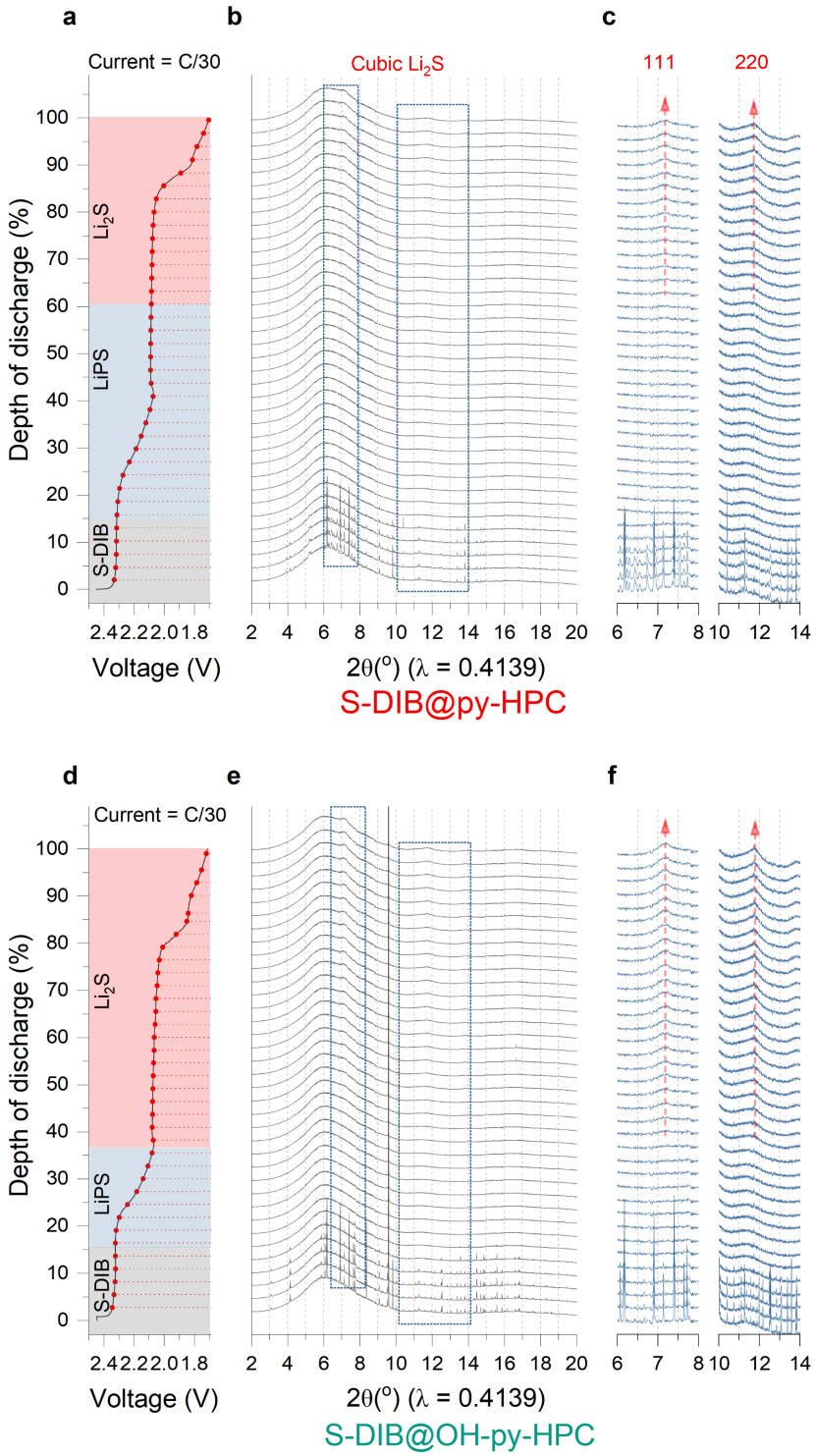

Figure 4-9 Discharging and XRD profiles of *operando* coin-cells assembled with (a-b) S-DIB@py-HPC, (d-e) S-DIB@OH-py-HPC as cathode.

4.5 Electrochemical performance

To highlight the benefits of the functionalized pyrene, electrochemical performance evaluations were conducted. **Figure 4-10** presents the CV profiles of S-DIB@py-HPC and S-DIB@X-py-HPC

at a scan rate of 0.02 mV s^{-1}. The electrodes exhibit two cathodic peaks at 2.32 and 2.055 V, which correspond to the reduction of elemental sulfur to soluble LiPS and its further reduction to solid Li_2S_2/Li_2S. During the subsequent anodic scan, a prominent peak at 2.34 V is observed, indicating the oxidation of solid Li_2S_2/Li_2S back to sulfur. Notably, S-DIB@OH-py-HPC and S-DIB@NH_2-py-HPC show the highest current response with minimal potential hysteresis, suggesting superior redox reaction kinetics.

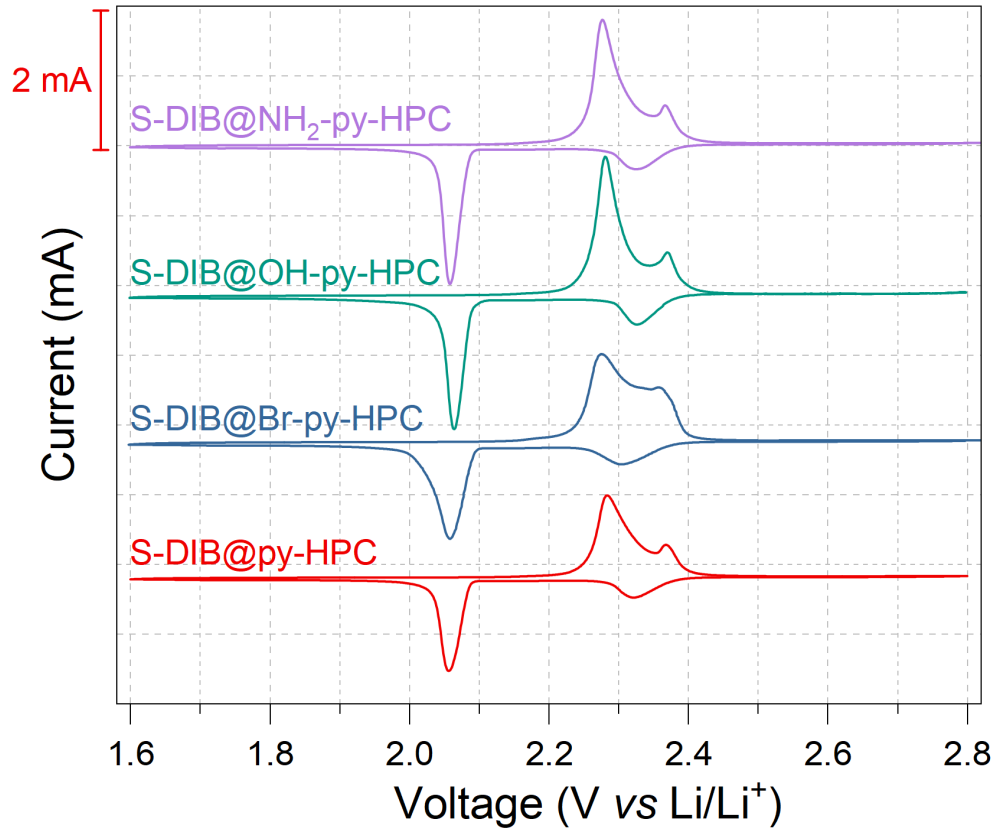

Figure 4-10 CV curves of S-DIB@py-HPC, S-DIB@Br-py-HPC, S-DIB@OH-py-HPC, and S-DIB@NH_2-py-HPC electrodes at scan rate of 0.02 mV/s.

To better understand the cathode kinetics of LiPS, GITT was used to study the polarization of the cathode redox reactions. The results are shown in **Figure 4-11**. The difference between the working voltage and the equilibrium voltage shows the degree of polarization (**Figure 4-12**). All samples show two distinct jumps in their overpotential profile. The larger, second jump is due to the nucleation and deposition of Li_2S, while the smaller, first jump is the overpotential needed to reduce long-chain LiPS to short-chain intermediates. These jumps, Q1 and Q2, correspond to the conversion of LiPS and the formation of insoluble Li_2S_2/Li_2S, respectively.[114, 115, 163, 164] This helps

in accurately determining their contributions to the overall capacity. Ideally, a Q2 ratio near 75% is achieve, indicating an almost complete conversion. The Q2 ratios for S-DIB@py-HPC, S-DIB@Br-py-HPC, S-DIB@OH-py-HPC, and S-DIB@NH_2-py-HPC are 65%, 69%, 71%, and 74%, respectively. The higher Q2 ratios in S-DIB@OH-py-HPC and S-DIB@NH_2-py-HPC suggest that polar groups can immobilize more LiPS and catalyze their conversion into Li_2S, confirming the results of the symmetric CV results.

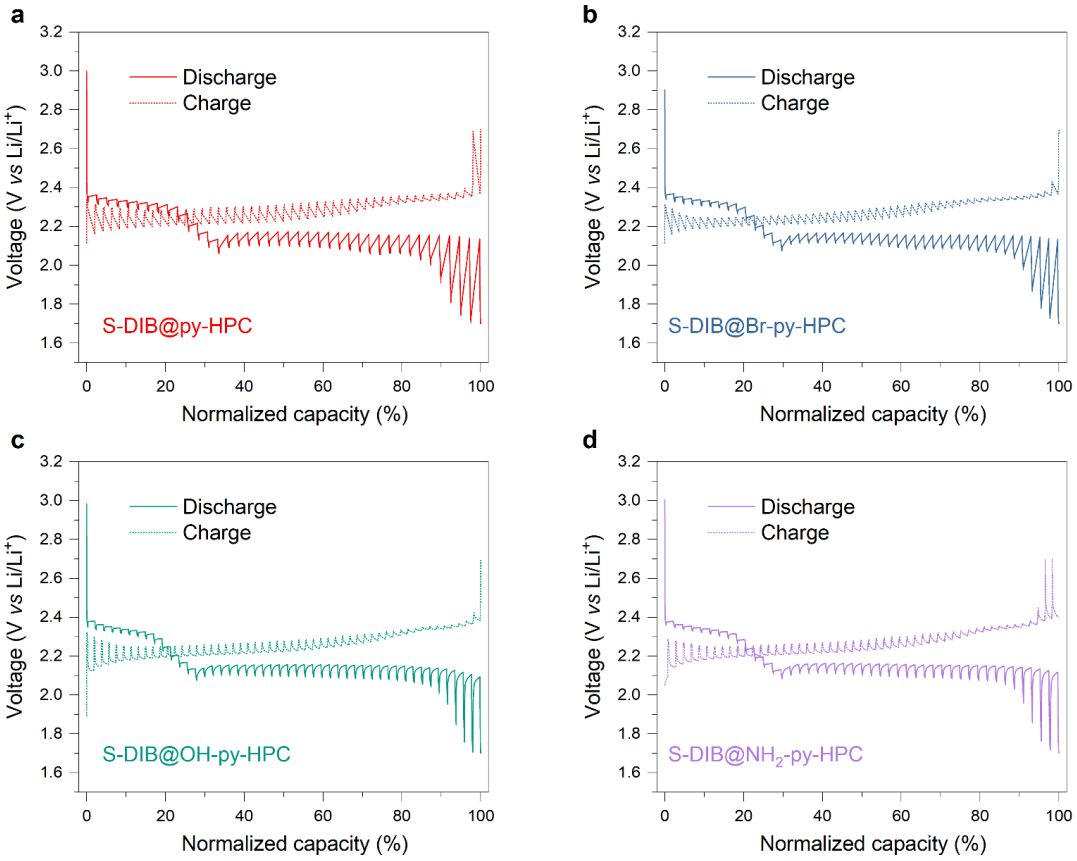

Figure 4-11 GITT results of S-DIB@HPC, S-DIB@py-HPC, S-DIB@Br-py-HPC, S-DIB@OH-py-HPC and S-DIB@NH_2-py-HPC.

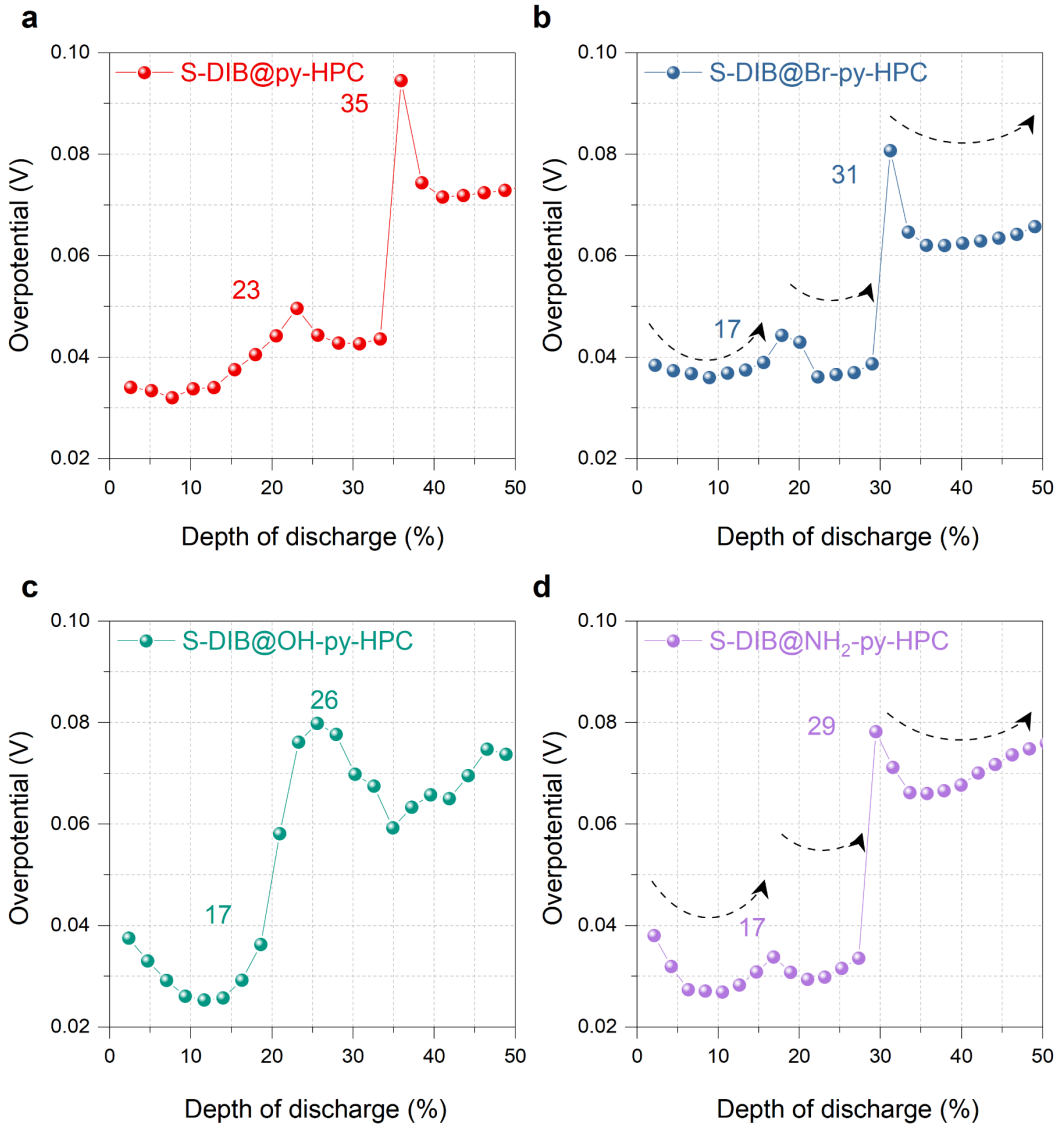

Figure 4-12 The overpotential results of the S-DIB@py-HPC, S-DIB@Br-py-HPC, S-DIB@OH-py-HPC, and S-DIB@NH2-py-HPC calculated from GITT.

Based on this analysis, S-DIB@OH-py-HPC and S-DIB@NH_2-py-HPC electrodes are expected to show superior capacity due to their stronger polar interfaces. To test this hypothesis, rate performance was evaluated under current densities from 0.1 C to 3 C, as shown in **Figure 4-13a**. Expectedly S-DIB@OH-py-HPC shows the highest initial discharge capacity of about 1251 mAh g^{-1} at 0.1 C. As the current density increases to 0.2, 0.5, 1, 2, and 3 C, capacities drop to 932, 880, 855, 752, and 600 mAh g^{-1}, respectively. These values are similar to those for S-DIB@NH_2-py-HPC and are significantly higher than other samples. When the discharge rate switches from 3 C to 0.1 C, a reversible capacity of 980 mAh g^{-1} is retained, indicating effective reversible electrode kinetics. The charge/discharge voltage profiles (**Figure 4-13b**) show that cathodes with OH and

NH_2 groups exhibit reduced polarization compared to other samples. Conversely, when some inherent defects in HPC are covered by pure pyrene, its capacity is slightly reduced compared to S-DIB@HPC.

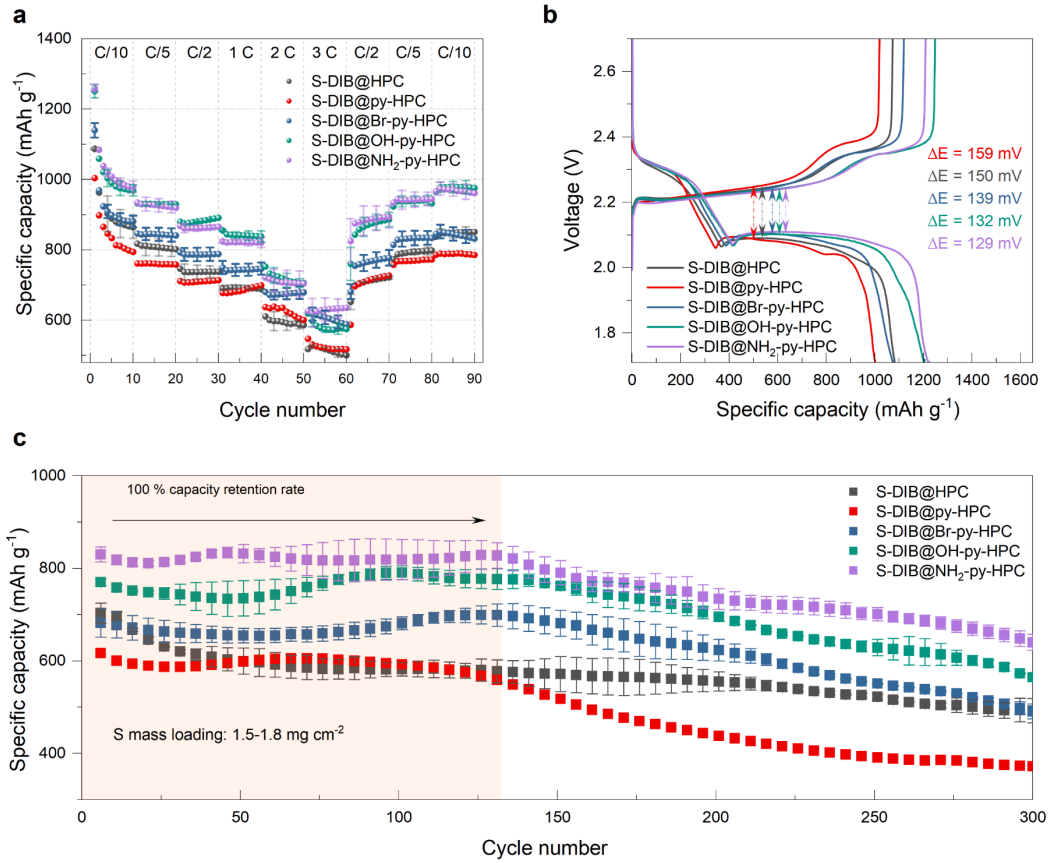

Figure 4-13 (a) Rate performance (b) The first discharge and charge curves and (c) cycling performance measured at 1 C of S-DIB@HPC S-DIB@py-HPC, S-DIB@Br-py-HPC, S-DIB@OH-py-HPC and S-DIB@NH_2-py-HPC.

To further explore long-term stability, cycling performance was measured at a high rate of 1 C (**Figure 4-13c**). The S-DIB@OH-py-HPC electrode shows a high initial specific capacity of around 829 mAh g^{-1}. After 300 charge/discharge cycles, its specific capacity remains at approximately 650 mAh g^{-1}, indicating a low capacity degradation of 0.071% per cycle and a coulombic efficiency of 95.4%. A reversible capacity of 600 mAh g^{-1} after 300 cycles is maintained for the S-DIB@OH-py-HPC electrode. Both S-DIB@NH_2-py-HPC and S-DIB@OH-py-HPC cathodes maintain higher capacities than S-DIB@HPC (400 mAh g^{-1}) and S-DIB@py-HPC electrodes (300 mAh g^{-1}). It is noteworthy that S-DIB@HPC shows a decreasing and then stable capacity decay trend, unlike S-DIB@X-py-HPC, whose capacity is largely stable for about 125 cycles before gradually declining. Surprisingly, the decay after about 125 is observed for all pyrene modified electrodes independent

of their functionalization. The exact origin of this phenomenon remains unclear. While the OH and NH_2 functionalized pyrenes, can partially suppress the shuttle effect in initial cycles due to a faster turnover of LiPS, this is not the case for the pure pyrene despite showing similar decay trend. Potentially pyrene molecules detach from the carbon surface during cycling, leading to a gradual decrease in capacity. However, if the detachment of pyrene molecules is responsible for the decay, it still remains unclear why this process has no effect on the capacity within the first 125 cycles.

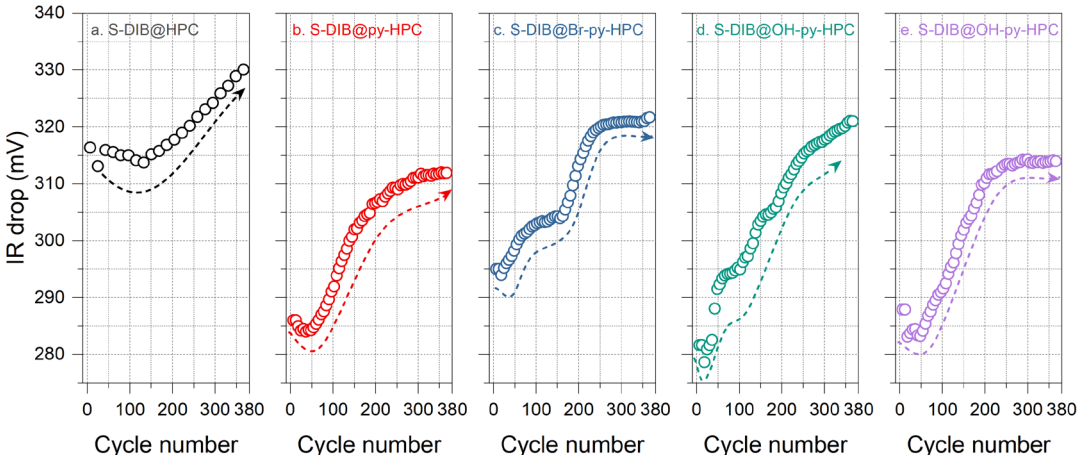

Figure 4-14 The voltage drops at the beginning of the discharge process.

In addition, a closer inspection of the capacity curve reveals that there is a more or less pronounced dip within the first 125 cycles. This may indicate, that an initial capacity loss process is compensated by a second process which helps to maintain a mostly stable capacity up to 125 cycles. This could be due to the gradual activation of initially inaccessible sulfur. However, this process does not fully explain, why the onset of the gradual decay occurs almost at the same cycle for all pyrene modified electrodes, despite their largely different initial capacities and electrode kinetics. To further elucidate the impact of pyrene on the cycling degradation trend, the initial iR drop during discharge was calculated and presented **Figure 4-14**. In line with the cycling decline trend, all pyrene-modified electrodes reach their minimum value at the 50th cycle, unlike HPC, which reaches it at the 150th cycle. After this point, the iR drop increases sharply with continued cycling.

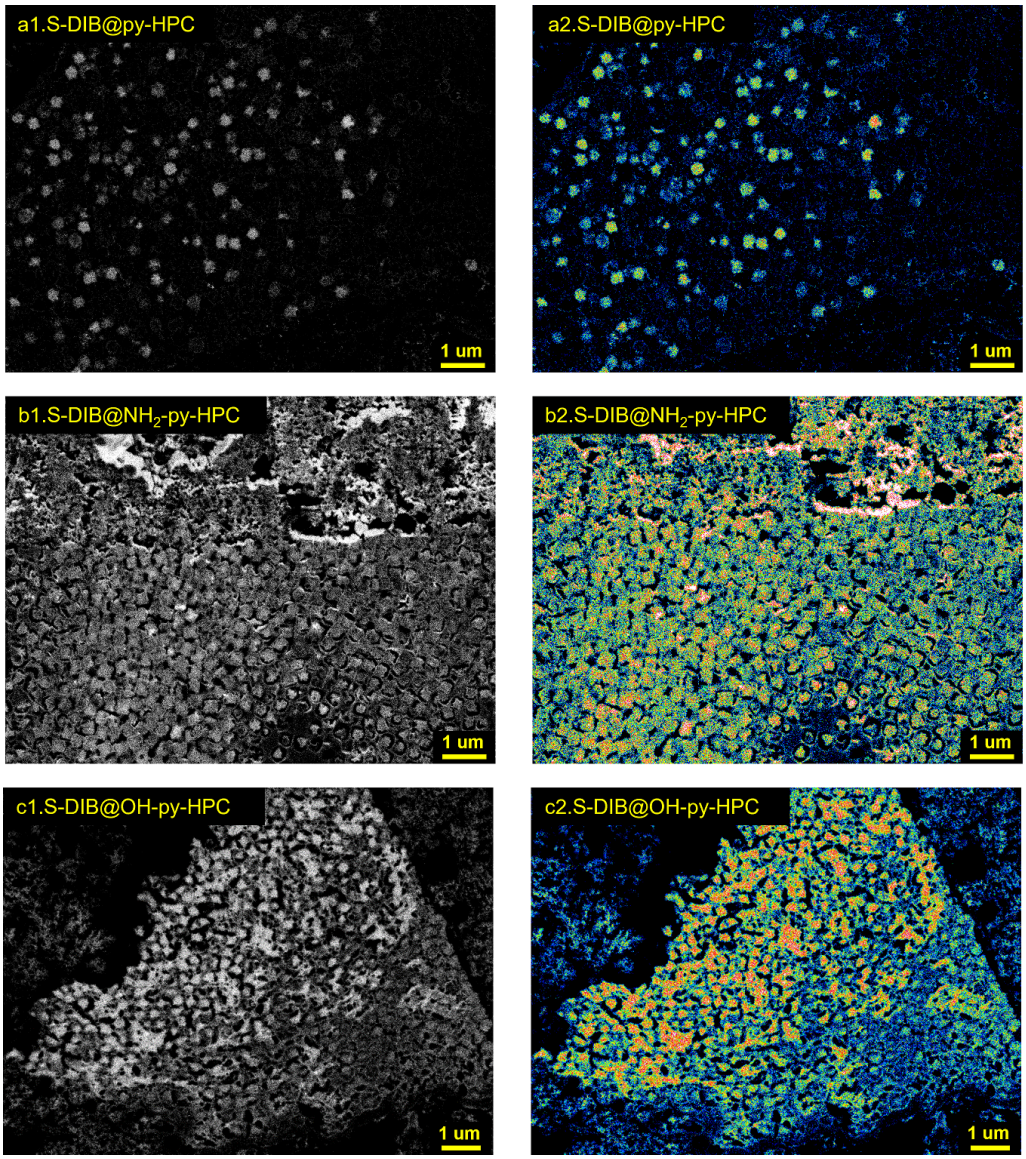

Figure 4-15 The cross-section view of S-DIB@py-HPC (a1), S-DIB@NH_2-py-HPC (b1) and S-DIB@OH-py-HPC (c1) after long cycling. (a2), (b2) and (c2) show corresponding heat-map processed images.

To examine the distribution of residual sulfur within the carbon pores, the electrode's cross-section after 300 cycles' cycling was characterized using EsB imaging, as explored in the previous chapter. Same parameters were used to obtain a clear sulfur distribution in the carbon matrix. **Figures 4-15** b2, and c2 show a substantial distribution of sulfur in NH_2-py-HPC and OH-py-HPC functionalized electrodes, whereas a significantly lower amount of sulfur is confined within the pores of py-HPC electrode. This confirms a much more pronounced shuttle effect caused by the sluggish sulfur redox kinetics associated with the weak polarity of py-HPC. The surface and cross-sectional morphologies of the cycled lithium anode against S-DIB@py-HPC, S-DIB@OH-py-HPC, and S-DIB@NH_2-py-HPC were characterized by SEM (**Figure 4-16**). Compared to the loose Li deposits with significant

cracks, the cycled Li metal anode paired with S-DIB@OH-py-HPC and S-DIB@NH2-py-HPC shows a dense and uniform Li deposition morphology. Additionally, the thickness of the deposited Li in S-DIB@OH-py-HPC and S-DIB@NH_2-py-HPC is 190 μm and 180 μm, respectively, which is considerably less than the 240 μm observed in S-DIB@py-HPC. This indicates that the introduced polar-group functionalized pyrene effectively mitigates LiPS side reactions and protects Li metal anodes in Li–S batteries by accelerating the conversion from LiPS to Li_2S.[19]

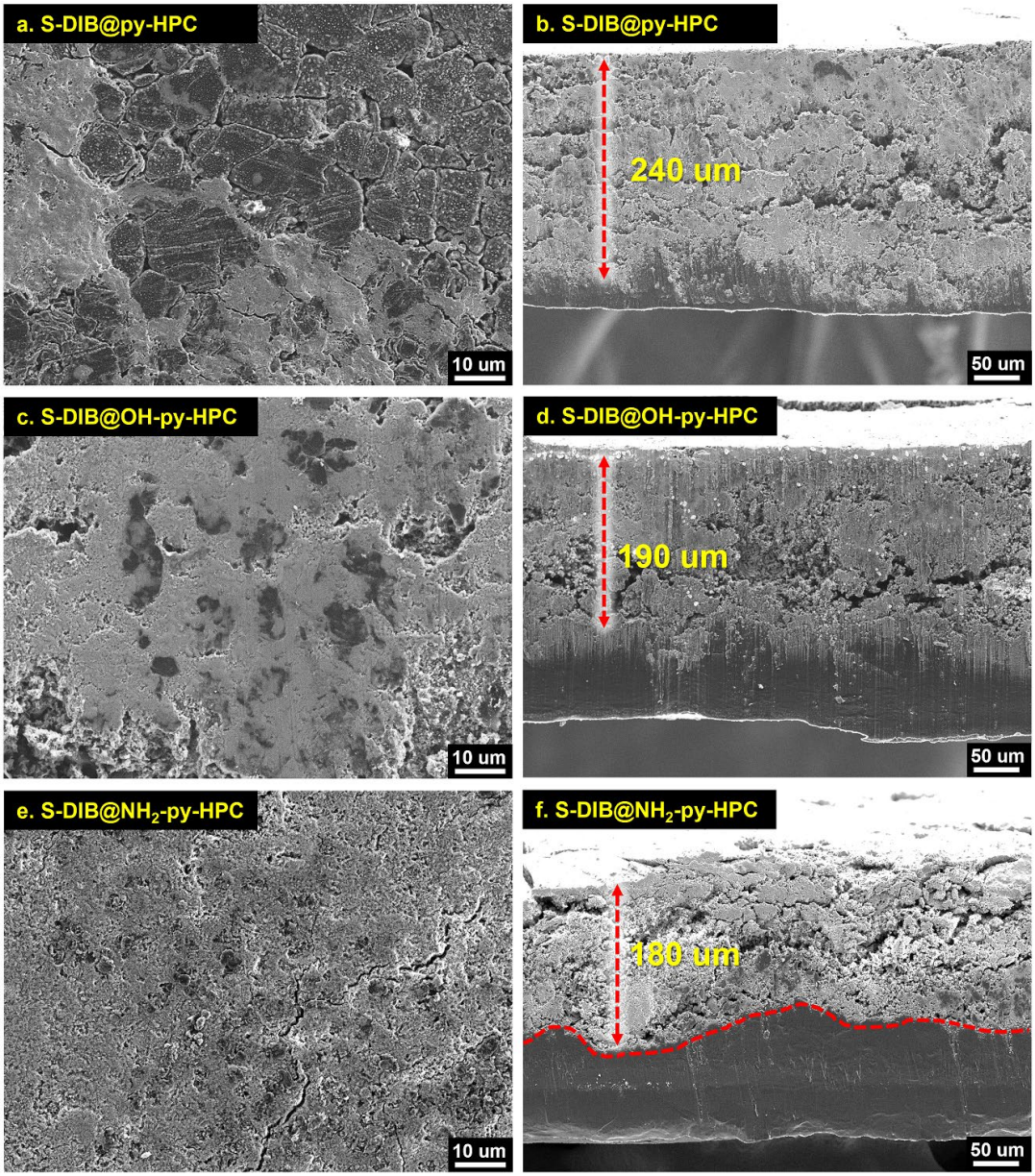

Figure 4-16 The surface morphology images of the Li anode after 300 cycles against: (a) S-DIB@py-HPC (b) S-DIB@OH-py-HPC (c) S-DIB@NH_2-py-HPC.

Additionally, the performance of the S-DIB@OH-py-HPC and S-DIB@NH_2-py-HPC cathodes with

high sulfur loading (3.5 mg and 3 mg S cm^{-2}, respectively) was evaluated in coin cells using a low electrolyte amount (E/S = 8 µL/mg S) to demonstrate their potential for practical Li–S batteries. These conditions closely mimic those required for real-world applications. As shown in Figure **4-1a**, the S-DIB@OH-py-HPC initially delivers a discharge capacity of 716 mAh g^{-1} at 0.2 C, maintaining a significant capacity of 603 mAh g^{-1} after 200 cycles. In contrast, the S-DIB@NH_2-py-HPC shows a higher initial capacity of 788 mAh g^{-1} but experiences a faster decline, reaching 590 mAh g^{-1} after 200 cycles (**Figure 4-17b**).

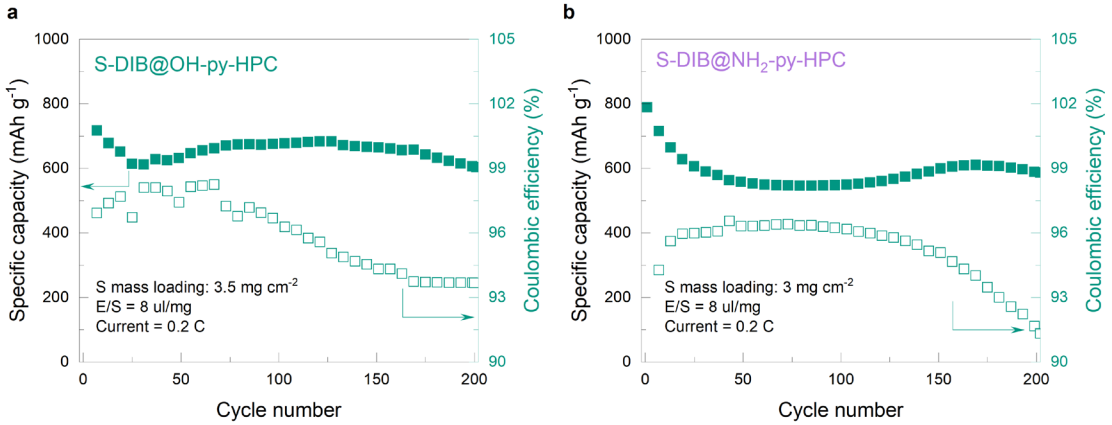

Figure 4-17 Cycling performance of the S-DIB@OH-py-HPC and S-DIB@NH_2-py-HPC electrode under high sulfur loading and lean electrolyte usage at C/5.

4.6 Conclusion

In this chapter, a feasible and non-destructive strategy has been proposed to modify HPC with functionalized pyrene. This strategy utilized the rich pore structure of HPC to enable efficient adsorption of pyrene while preserving its structure and surface properties after the adsorption process. Due to the polar groups and the non-electroneutrality of the X-pyrene molecules on the carbon surface, the modified HPC can enhance the redox kinetics of LiPS and promote the precipitation of Li_2S. The Li_2S precipitation process were investigated in detail using operando XRD. The S-DIB@OH-py-HPC and S-DIB@NH_2-py-HPC cathodes both demonstrate a higher initial discharge capacity of 1250 mAh g^{-1} at 0.1 C and more stable cycling compared to non-functionalized S-DIB@HPC electrode. Good capacity retention of 86% after 200 cycles at 0.2 C was also obtained for S-DIB@OH-py-HPC cathodes, with a high sulfur loading of 3.5 mg cm^{-1} and a low electrolyte usage of 8 µL/mg S. The effectiveness of LiPS retention due to functionalized

pyrenes was further confirmed by EsB imaging of sulfur distribution in the electrodes after cycling.

5 Summary and Outlook

5.1 Summary and conclusions

In summary, the ZIF-8 derived hollow porous carbon, with its numerous internal pores, acts as an efficient reactor for the IV reaction, resulting in a sulfur-rich polymer/carbon composite ideal for Li–S battery cathodes. This method is more time-efficient compared to the melt diffusion technique for creating sulfur/carbon composites. The evenly distributed sulfur-rich polymer within the carbon matrix helps to physically and chemically mitigate the shuttle effect, thereby enhancing cycling stability. The EsB detector is instrumental in distinguishing intermediates during discharge and charge processes, visualizing their distribution within the electrode. EsB imaging offers valuable insights into the kinetics of sulfur redox reactions, active material loss, and electrode degradation. Furthermore, functionalized pyrenes can effectively modify the carbon surface, promoting Li_2S precipitation and improving sulfur utilization. Their interaction with LiPS further helps further to confine the shuttle effect and enhance cycling stability.

5.2 Outlook on future research possibilities

Due to the solubility of LiPS in the electrolyte, unlike other battery systems, the amount of electrolyte used in Li–S batteries have a direct impact on their rate performance and cycling stability. This thesis finds that the higher the electrolyte dosage, the more obvious the shuttle effect is, which leads to a rapid decline in performance in the first serval cycles. Lower electrolyte dosages complicate the Li_2S precipitation step, especially at higher discharge/charge currents. A battery system with less electrolyte helps improve the energy density. Future cathode development should focus on sulfur-carbon composites with high electrical conductivity, capable of achieving faster lithium-ion diffusion and sulfur redox processes under lean electrolyte conditions.

The EsB technique, as demonstrated in this work, effectively distinguishes sulfur distribution in the electrode before and after lithiation. The potential applications of this technique are broad, including characterizing hard carbon and hard carbon post-sodium embedding in sodium-ion batteries, as well as analyzing silicon sphere distribution and volume expansion during de/lithiation. Given its precision in working distance studies, combining this technique with cross-section acquisition

systems like GATAN ion polishing or FIB holds promise for characterizing charging and discharging principles and conducting failure analysis of various battery electrodes.

Bibliography

[1] Li, G.; Chen, Z.; Lu, J., *Chem* **2018**, *4* (1), 3-7, DOI: 10.1016/j.chempr.2017.12.012

[2] Sun, J.; Wang, T.; Gao, Y.; Pan, Z.; Hu, R., et al., *InfoMat* **2022**, *4* (9), e12359, DOI: 10.1002/inf2.12359

[3] Manthiram, A.; Fu, Y.; Chung, S.-H.; Zu, C.; Su, Y.-S., *Chem. Rev.* **2014**, *114* (23), 11751-11787, DOI: 10.1021/cr500062v

[4] Shao, Q.; Zhu, S.; Chen, J., *Nano Res.* **2023**, *16* (6), 8097-8138, DOI: 10.1007/s12274-022-5227-0

[5] Lu, Y.-C.; He, Q.; Gasteiger, H. A., *J. Phys. Chem. C* **2014**, *118* (11), 5733-5741, DOI: 10.1021/jp500382s

[6] Wang, Q.; Zheng, J.; Walter, E.; Pan, H.; Lv, D., et al., *J. Electrochem. Soc.* **2015**, *162* (3), A474-A478, DOI: 10.1149/2.0851503jes

[7] Lang, S.; Yu, S.-H.; Feng, X.; Krumov, M. R.; Abruña, H. D., *Nat. Commun.* **2022**, *13* (1), 4811, DOI: 10.1038/s41467-022-32139-w

[8] Waluś, S.; Barchasz, C.; Bouchet, R.; Leprêtre, J. C.; Colin, J. F., et al., *Adv. Energy Mater.* **2015**, *5* (16), 1500165, DOI: 10.1002/aenm.201500165

[9] Barchasz, C.; Molton, F.; Duboc, C.; Lepretre, J. C.; Patoux, S., et al., *Anal.Chem.* **2012**, *84* (9), 3973-3980, DOI: 10.1021/ac2032244

[10] Andersen, A.; Rajput, N. N.; Han, K. S.; Pan, H.; Govind, N., et al., *Chem. Mater.* **2019**, *31* (7), 2308-2319, DOI: 10.1021/acs.chemmater.8b03944

[11] Park, C.; Ronneburg, A.; Risse, S.; Ballauff, M.; Kanduč, M., et al., *J. Phys. Chem. C* **2019**, *123* (16), 10167-10177, DOI: 10.1021/acs.jpcc.8b10175

[12] Song, Y.-W.; Shen, L.; Li, X.-Y.; Zhao, C.-X.; Zhou, J., et al., *Nat. Chem. Eng.* **2024**, DOI: 10.1038/s44286-024-00115-4

[13] Zhou, S.; Shi, J.; Liu, S.; Li, G.; Pei, F., et al., *Nature* **2023**, *621* (7977), 75-81, DOI: 10.1038/s41586-023-06326-8

[14] Lee, B. J.; Kang, T. H.; Lee, H. Y.; Samdani, J. S.; Jung, Y., et al., *Adv. Energy Mater.* **2020**, *10* (22), 1903934, DOI: 10.1002/aenm.201903934

[15] Guo, J.; Pei, H.; Dou, Y.; Zhao, S.; Shao, G., et al., *Adv. Funct. Mater.* **2021**, *31* (18), 2010499, DOI: 10.1002/adfm.202010499

[16] Zhang, B.; Wu, J.; Gu, J.; Li, S.; Yan, T., et al., *ACS Energy Lett.* **2021**, *6* (2), 537-546, DOI: 10.1021/acsenergylett.0c02527

[17] Li, J.; Gao, L.; Pan, F.; Gong, C.; Sun, L., et al., *Nanomicro Lett.* **2023**, *16* (1), 12, DOI: 10.1007/s40820-023-01223-1

[18] Drvarič Talian, S.; Bobnar, J.; Moškon, J.; Dominko, R.; Gaberšček, M., *Electrochim. Acta.* **2020**, *354*, 136696, DOI: 10.1016/j.electacta.2020.136696

[19] Zou, K.; Zhou, T.; Chen, Y.; Xiong, X.; Jing, W., et al., *Adv. Energy Mater.* **2022**, *12* (18), 2103981, DOI: 10.1002/aenm.202103981

[20] Fan, Q.; Jiang, J.; Zhang, S.; Zhou, T.; Pang, W. K., et al., *Adv. Energy Mater.* **2021**, *11* (32), 2100957, DOI: 10.1002/aenm.202100957

[21] Luo, Y.; Fang, Z.; Duan, S.; Wu, H.; Liu, H., et al., *Angew. Chem. Int. Ed.* **2023**, *62* (11), e202215802, DOI: 10.1002/anie.202215802

[22] Xu, Z. L.; Huang, J. Q.; Chong, W. G.; Qin, X.; Wang, X., et al., *Adv. Energy Mater.* **2017**, *7* (9), 1602078, DOI: 10.1002/aenm.201602078

[23] Waluś, S.; Offer, G.; Hunt, I.; Patel, Y.; Stockley, T., et al., *Energy Storage Materials* **2018**, *10*, 233-245, DOI: 10.1016/j.ensm.2017.05.017

[24] Shaibani, M.; Mirshekarloo, M. S.; Singh, R.; Easton, C. D.; Cooray, M. C. D., et al., *Sci. Adv.* **2020**, *6* (1), eaay2757, DOI: 10.1126/sciadv.aay2757

[25] Zhao, M.; Chen, X.; Li, X.-Y.; Li, B.-Q.; Huang, J.-Q., *Adv. Mater.* **2021**, *33* (13), 2007298, DOI: 10.1002/adma.202007298

[26] Hou, L.; Zhang, X.; Yao, N.; Chen, X.; Li, B., et al., *Chem* **2022**, *8* (4), 1083-1098, DOI: 10.1016/j.chempr.2021.12.023

[27] Razaq, R.; Din, M. M. U.; Småbråten, D. R.; Eyupoglu, V.; Janakiram, S., et al., *Adv. Energy Mater.* **2023**, *14* (3), DOI: 10.1002/aenm.202302897

[28] Li, P.; Lv, H.; Li, Z.; Meng, X.; Lin, Z., et al., *Adv. Mater.* **2021**, *33* (17), 2007803, DOI: 10.1002/adma.202007803

[29] Bi, C.-X.; Yao, N.; Li, X.-Y.; Zhang, Q.-K.; Chen, X., et al., *Adv. Mater.* **2024**, 2411197, DOI: 10.1002/adma.202411197

[30] Zhang, G.; Peng, H.-J.; Zhao, C.-Z.; Chen, X.; Zhao, L.-D., et al., *Angew. Chem. Int. Ed.* **2018**, *57* (51), 16732-16736, DOI: 10.1002/anie.201810132

[31] Meyer, B., *Chem. Rev.* **1976**, *76* (3), 367-388, DOI: 10.1021/cr60301a003

[32] Ji, X.; Lee, K. T.; Nazar, L. F., *Nat. Mater.* **2009**, *8* (6), 500-506, DOI: 10.1038/nmat2460

[33] Li, Z.; Yuan, L.; Yi, Z.; Sun, Y.; Liu, Y., et al., *Adv. Energy Mater.* **2013**, *4* (7), 1301473, DOI: 10.1002/aenm.201301473

[34] Schuster, J.; He, G.; Mandlmeier, B.; Yim, T.; Lee, K. T., et al., *Angew. Chem. Int. Ed.* **2012**, *51* (15), 3591-3595, DOI: 10.1002/anie.201107817

[35] Zhang, F.; Liu, X.; Yang, M.; Cao, X.; Huang, X., et al., *Nano Energy* **2020**, *69*, DOI: 10.1016/j.nanoen.2019.104443

[36] Hou, J.; Tu, X.; Wu, X.; Shen, M.; Wang, X., et al., *Chem. Eng. J.* **2020**, *401*, 126141, DOI: 10.1016/j.cej.2020.126141

[37] Strubel, P.; Thieme, S.; Biemelt, T.; Helmer, A.; Oschatz, M., et al., *Adv. Funct. Mater.* **2014**, *25* (2), 287-297, DOI: 10.1002/adfm.201402768

[38] Guan, L.; Hu, H.; Li, L.; Pan, Y.; Zhu, Y., et al., *ACS Nano* **2020**, *14* (5), 6222-6231, DOI: 10.1021/acsnano.0c02294

[39] Miao, X.; Sun, D.; Zhou, X.; Lei, Z., *Chem. Eng. J.* **2019**, *364*, 208-216, DOI: 10.1016/j.cej.2019.01.158

[40] Ummethala, R.; Fritzsche, M.; Jaumann, T.; Balach, J.; Oswald, S., et al., *Energy Storage Materials* **2018**, *10*, 206-215, DOI: 10.1016/j.ensm.2017.04.004

[41] Zhao, Y.; Wu, W.; Li, J.; Xu, Z.; Guan, L., *Adv. Mater.* **2014**, *26* (30), 5113-5118, DOI: 10.1002/adma.201401191

[42] Zhang, Y.; Li, G.; Wang, J.; Luo, D.; Sun, Z., et al., *Adv. Energy Mater.* **2021**, *11* (26), 2100497, DOI: 10.1002/aenm.202100497

[43] Sun, Y.; Wang, H.; Wei, W.; Zheng, Y.; Tao, L., et al., *ACS Nano* **2021**, *15* (1), 1652-1665, DOI: 10.1021/acsnano.0c09290

[44] Xu, H.; Jiang, Q.; Zhang, B.; Chen, C.; Lin, Z., *Adv. Mater.* **2020**, *32* (7), 1906357, DOI: 10.1002/adma.201906357

[45] Zhou, G.; Paek, E.; Hwang, G. S.; Manthiram, A., *Adv. Energy Mater.* **2015**, *6* (2), 1501335, DOI: 10.1002/aenm.201501355

[46] Cai, W.; Song, Y.; Fang, Y.; Wang, W.; Yu, S., et al., *Nano Res.* **2020**, *13* (12), 3315-3320, DOI: 10.1007/s12274-020-3009-0

[47] Tian, L.; Zhang, Z.; Liu, S.; Li, G.; Gao, X., *Energy & Environmental Materials* **2021**, *5* (2), 645-654, DOI: 10.1002/eem2.12215

[48] Ji, L.; Wang, X.; Jia, Y.; Hu, Q.; Duan, L., et al., *Adv. Funct. Mater.* **2020**, *30* (28), 1910533, DOI: 10.1002/adfm.201910533

[49] Ren, J.; Song, Z.; Zhou, X.; Chai, Y.; Lu, X., et al., *ChemElectroChem* **2019**, *6* (13), 3410-3419, DOI: 10.1002/celc.201900744

[50] Sun, Q.; Fang, X.; Weng, W.; Deng, J.; Chen, P., et al., *Angew. Chem. Int. Ed.* **2015**, *54* (36), 10539-10544, DOI: 10.1002/anie.201504514

[51] Peng, H. J.; Huang, J. Q.; Zhao, M. Q.; Zhang, Q.; Cheng, X. B., et al., *Adv. Funct. Mater.* **2014**, *24* (19), 2772-2781, DOI: 10.1002/adfm.201303296

[52] Cai, J.; Wu, C.; Yang, S.; Zhu, Y.; Shen, P. K., et al., *ACS Appl. Mater. Interfaces.* **2017**, *9* (39), 33876-33886, DOI: 10.1021/acsami.7b09808

[53] Freund, R.; Zaremba, O.; Arnauts, G.; Ameloot, R.; Skorupskii, G., et al., *Angew. Chem. Int. Ed.* **2021**, *60* (45), 23975-24001, DOI: 10.1002/anie.202106259

[54] Shi, Y.; Feng, D.; Ahmad, S.; Liu, L.; Tang, J., *Chem. Eng. J.* **2023**, *454*, 140244, DOI: 10.1016/j.cej.2022.140244

[55] Barrio, J.; Volokh, M.; Shalom, M., *J. Mater. Chem. A* **2020**, *8* (22), 11075-11116, DOI: 10.1039/d0ta01973a

[56] Wang, R.; Yang, J.; Chen, X.; Zhao, Y.; Zhao, W., et al., *Adv. Energy Mater.* **2020**, *10* (9), DOI: 10.1002/aenm.201903550

[57] Xiao, F.; Yang, X.; Wang, H.; Xu, J.; Liu, Y., et al., *Adv. Energy Mater.* **2020**, *10* (23), 2000931, DOI: 10.1002/aenm.202000931

[58] Du, Z.; Chen, X.; Hu, W.; Chuang, C.; Xie, S., et al., *J. Am. Chem. Soc.* **2019**, *141* (9), 3977-3985, DOI: 10.1021/jacs.8b12973

[59] Zhang, Q.; Zhang, X.; Lei, D.; Qiao, S.; Wang, Q., et al., *ACS Appl. Mater. Interfaces.* **2023**, *15* (12), 15377-15386, DOI: 10.1021/acsami.2c21903

[60] Liu, G.; Feng, K.; Cui, H.; Li, J.; Liu, Y., et al., *Chem. Eng. J.* **2020**, *381*, 122652, DOI: 10.1016/j.cej.2019.122652

[61] Wang, Z. Y.; Wang, L.; Liu, S.; Li, G. R.; Gao, X. P., *Adv. Funct. Mater.* **2019**, *29* (23), DOI: 10.1002/adfm.201901051

[62] Jin, J.; Cai, W.; Cai, J.; Shao, Y.; Song, Y., et al., *J. Mater. Chem. A* **2020**, *8* (6), 3027-3034, DOI: 10.1039/c9ta13046b

[63] Chen, Y.; Zhang, W.; Zhou, D.; Tian, H.; Su, D., et al., *ACS Nano* **2019**, *13* (4), 4731-4741, DOI: 10.1021/acsnano.9b01079

[64] Zhang, Q.; Huang, Q.; Hao, S.-M.; Deng, S.; He, Q., et al., *Adv. Sci.* **2022**, *9* (2), 2103798, DOI: 10.1002/advs.202103798

[65] Wu, D.; Liu, J.; Chen, J.; Li, H.; Cao, R., et al., *J. Mater. Chem. A* **2021**, *9* (9), 5497-5506, DOI: 10.1039/d0ta12110j

[66] Greer, S. C., *J. Phys. Chem. B* **1998**, *102* (28), 5413-5422, DOI: 10.1021/jp981592z

[67] Chung, W. J.; Griebel, J. J.; Kim, E. T.; Yoon, H.; Simmonds, A. G., et al., *Nat. Chem.* **2013**, *5* (6), 518-524, DOI: 10.1038/nchem.1624

[68] Simmonds, A. G.; Griebel, J. J.; Park, J.; Kim, K. R.; Chung, W. J., et al., *ACS Macro Lett.* **2014**, *3* (3), 229-232, DOI: 10.1021/mz400649w

[69] Zeng, Q.; Li, X.; Gong, W.; Guo, S.; Ouyang, Y., et al., *Adv. Energy Mater.* **2022**, *12*, 2104074, DOI: 10.1002/aenm.202104074

[70] Kang, H.; Kim, H.; Park, M. J., *Adv. Energy Mater.* **2018**, *8* (32), 1802423, DOI: 10.1002/aenm.201802423

[71] Dirlam, P. T.; Simmonds, A. G.; Kleine, T. S.; Nguyen, N. A.; Anderson, L. E., et al., *RSC Adv.* **2015**, *5* (31), 24718-24722, DOI: 10.1039/c5ra01188d

[72] Sun, Z.; Xiao, M.; Wang, S.; Han, D.; Song, S., et al., *J. Mater. Chem. A* **2014**, *2* (24), 9280-9286, DOI: 10.1039/c4ta00779d

[73] Kim, H.; Lee, J.; Ahn, H.; Kim, O.; Park, M. J., *Nat. Commun.* **2015**, *6*, 7278, DOI: 10.1038/ncomms8278

[74] Oschmann, B.; Park, J.; Kim, C.; Char, K.; Sung, Y.-E., et al., *Chem. Mater.* **2015**, *27* (20), 7011-7017, DOI: 10.1021/acs.chemmater.5b02317

[75] Chang, A.; Wu, Q.; Du, X.; Chen, S.; Shen, J., et al., *Chemical Communications* **2016**, *52* (24), 4525-4528, DOI: 10.1039/c6cc00489j

[76] Je, S. H.; Hwang, T. H.; Talapaneni, S. N.; Buyukcakir, O.; Kim, H. J., et al., *ACS Energy Lett.* **2016**, *1* (3), 566-572, DOI: 10.1021/acsenergylett.6b00245

[77] Talapaneni, S. N.; Hwang, T. H.; Je, S. H.; Buyukcakir, O.; Choi, J. W., et al., *Angew. Chem. Int. Ed.* **2016**, *55* (9), 3106-3111, DOI: 10.1002/anie.201511553

[78] Zhang, T.; Hu, F.; Shao, W.; Liu, S.; Peng, H., et al., *ACS Nano* **2021**, *15* (9), 15027-15038, DOI: 10.1021/acsnano.1c05330

[79] Zhao, L.; Qiu, F.; Deng, X.; Huang, Y.; Li, Y., et al., *ACS Appl. Energy Mater.* **2022**, *5* (6), 7617-7626, DOI: 10.1021/acsaem.2c00866

[80] Wang, H.; Zhang, B.; Dop, R.; Yan, P.; Neale, A. R., et al., *J. Power Sources* **2022**, *545*, 231921, DOI: 10.1016/j.jpowsour.2022.231921

[81] Liu, X.; Lu, Y.; Zeng, Q.; Chen, P.; Li, Z., et al., *ChemSusChem* **2020**, *13* (4), 715-723, DOI: 10.1002/cssc.201903122

[82] Zeng, S.; Li, L.; Xie, L.; Zhao, D.; Wang, N., et al., *ChemSusChem* **2017**, *10* (17), 3378-3386, DOI: 10.1002/cssc.201700913

[83] Shen, K.; Mei, H.; Li, B.; Ding, J.; Yang, S., *Adv. Energy Mater.* **2018**, *8* (4), 1701527, DOI: 10.1002/aenm.201701527

[84] Chang, C.-H.; Manthiram, A., *ACS Energy Lett.* **2017**, *3* (1), 72-77, DOI: 10.1021/acsenergylett.7b01031

[85] Park, J.; Kim, E. T.; Kim, C.; Pyun, J.; Jang, H. S., et al., *Adv. Energy Mater.* **2017**, *7* (19), 1700074, DOI: 10.1002/aenm.201700074

[86] Wang, Y.; Luo, Z.; Zhou, J.; Fan, X.; Zhang, J., et al., *ACS Appl. Polym. Mater.* **2022**, *4* (2), 939-949, DOI: 10.1021/acsapm.1c01398

[87] Hu, G.; Sun, Z.; Shi, C.; Fang, R.; Chen, J., et al., *Adv. Mater.* **2017**, *29* (11), 1603835, DOI: 10.1002/adma.201603835

[88] Wu, F.; Chen, S.; Srot, V.; Huang, Y.; Sinha, S. K., et al., *Adv. Mater.* **2018**, *30* (13), 1706643, DOI: 10.1002/adma.201706643

[89] Xu, N.; Qian, T.; Liu, X.; Liu, J.; Chen, Y., et al., *Nano Lett.* **2017**, *17* (1), 538-543, DOI: 10.1021/acs.nanolett.6b04610

[90] Xue, L.; Li, Y.; Hu, A.; Zhou, M.; Chen, W., et al., *Small Structures* **2022**, *3* (3), 2100170, DOI: 10.1002/sstr.202100170

[91] Geng, C.; Qu, W.; Han, Z.; Wang, L.; Lv, W., et al., *Adv. Energy Mater.* **2023**, *13* (15), 2204246, DOI: 10.1002/aenm.202204246

[92] Sun, R.; Bai, Y.; Bai, Z.; Peng, L.; Luo, M., et al., *Adv. Energy Mater.* **2022**, *12* (12), 2102739, DOI: 10.1002/aenm.202102739

[93] Luo, C.; Liang, X.; Sun, Y.; Lv, W.; Sun, Y., et al., *Energy Storage Materials* **2020**, *33*, 290-297, DOI: 10.1016/j.ensm.2020.08.033

[94] Ni, L.; Gu, J.; Jiang, X.; Xu, H.; Wu, Z., et al., *Angew. Chem. Int. Ed.* **2023**, *62* (36), e202306528, DOI: 10.1002/anie.202306528

[95] He, Q.; Freiberg, A. T. S.; Patel, M. U. M.; Qian, S.; Gasteiger, H. A., *J. Electrochem. Soc.* **2020**, *167* (8), DOI: 10.1149/1945-7111/ab8645

[96] He, X.; Liu, Z.; Gao, G.; Liu, X.; Swietoslawski, M., et al., *J. Energy Chem.* **2021**, *59*, 1-8, DOI: 10.1016/j.jechem.2020.10.002

[97] Pan, W.; Yamamoto, K.; Matsunaga, T.; Watanabe, T.; Kumar, M., et al., *Batter. Supercaps* **2023**, *7* (1), e202300427, DOI: 10.1002/batt.202300427

[98] Cuisinier, M.; Cabelguen, P.-E.; Evers, S.; He, G.; Kolbeck, M., et al., *J. Phys. Chem. Lett.* **2013**, *4* (19), 3227-3232, DOI: 10.1021/jz401763d

[99] Kavcic, M.; Petric, M.; Rajh, A.; Isakovic, K.; Vizintin, A., et al., *ACS Appl. Energy Mater.* **2021**, *4* (3), 2357-2364, DOI: 10.1021/acsaem.0c02878

[100] Zhong, Y.; Wang, Q.; Bak, S.-M.; Hwang, S.; Du, Y., et al., *J. Am. Chem. Soc.* **2023**, *145* (13), 7390-7396, DOI: 10.1021/jacs.2c13776

[101] Scafuri, A.; Berthelot, R.; Pirnat, K.; Vizintin, A.; Bitenc, J., et al., *Chem. Mater.* **2020**, *32* (19), 8266-8275, DOI: 10.1021/acs.chemmater.0c02074

[102] Robba, A.; Barchasz, C.; Bucar, K.; Petric, M.; Zitnik, M., et al., *J. Phys. Chem. Lett.* **2020**, *11* (14), 5446-5450, DOI: 10.1021/acs.jpclett.0c01120

[103] Thangavel, N. K.; Mahankali, K.; Arava, L. M. R., *J. Electrochem. Soc.* **2022**, *169* (6), DOI: 10.1149/1945-7111/ac70ff

[104] Tan, C.; Kok, M. D. R.; Daemi, S. R.; Brett, D. J. L.; Shearing, P. R., *Phys Chem Chem Phys* **2019**, *21* (8), 4145-4154, DOI: 10.1039/c8cp04763d

[105] Dorai, A.; Kawamura, J.; Omata, T., *Electrochem. Commun.* **2022**, *141*, 107360, DOI: 10.1016/j.elecom.2022.107360

[106] Abe, M.; Kaneko, F.; Ishiguro, N.; Kubo, T.; Chujo, F., et al., *J. Phys. Chem. C* **2022**, *126* (33), 14047-14057, DOI: 10.1021/acs.jpcc.2c02795

[107] Yu, S.-H.; Huang, X.; Schwarz, K.; Huang, R.; Arias, T. A., et al., *Energy Environ. Sci.* **2018**, *11* (1), 202-210, DOI: 10.1039/C7EE02874A

[108] Bradbury, R.; Dewald, G. F.; Kraft, M. A.; Arlt, T.; Kardjilov, N., et al., *Adv. Energy Mater.* **2023**, *13* (17), 202203426, DOI: 10.1002/aenm.202203426

[109] Xu, R.; Xiang, J.; Feng, J.; Lu, X.; Hao, Z., et al., *Energy Storage Materials* **2020**, *31*, 164-171, DOI: 10.1016/j.ensm.2020.06.011

[110] Huang, X.; Wang, Z.; Knibbe, R.; Luo, B.; Ahad, S. A., et al., *Energy Technol.* **2019**, *7* (8), 1801001, DOI: 10.1002/ente.201801001

[111] Liu, R.; Wei, Z.; Peng, L.; Zhang, L.; Zohar, A., et al., *Nature* **2024**, *626* (7997), 98-104, DOI: 10.1038/s41586-023-06918-4

[112] Li, L.; Ma, Z.; Li, Y., *Carbon* **2022**, *197*, 200-208, DOI: 10.1016/j.carbon.2022.06.036

[113] Carbone, L.; Coneglian, T.; Gobet, M.; Munoz, S.; Devany, M., et al., *J. Power Sources* **2018**, *377*, 26-35, DOI: 10.1016/j.jpowsour.2017.11.079

[114] Li, Z.; Hou, L.-P.; Yao, N.; Li, X.-Y.; Chen, Z.-X., et al., *Angew. Chem. Int. Ed.* **2023**, *62* (43), e202309968, DOI: 10.1002/anie.202309968

[115] Lama, F. L.; Marangon, V.; Caballero, A.; Morales, J.; Hassoun, J., *ChemSusChem* **2023**, *16* (6), e202202095, DOI: 10.1002/cssc.202202095

[116] Schuepfer, D. B.; Badaczewski, F.; Guerra-Castro, J. M.; Hofmann, D. M.; Heiliger, C., et al., *Carbon* **2020**, *161*, 359-372, DOI: 10.1016/j.carbon.2019.12.094

[117] Zhang, P.; Fan, J.; Wang, Y.; Dang, Y.; Heumann, S., et al., *Carbon* **2024**, *222*, 118998, DOI: 10.1016/j.carbon.2024.118998

[118] Vizintin, A.; Lozinšek, M.; Chellappan, R. K.; Foix, D.; Krajnc, A., et al., *Chem. Mater.* **2015**, *27* (20), 7070-7081, DOI: 10.1021/acs.chemmater.5b02906

[119] Fitch, S. D. S.; Moehl, G. E.; Meddings, N.; Fop, S.; Soule, S., et al., *ACS Appl. Mater. Interfaces.* **2023**, *15* (33), 39198-39210, DOI: 10.1021/acsami.3c04897

[120] Zhou, W.; Apkarian, R. P.; Wang, Z.; Joy, D., **2007**, 1-40,

[121] Nohl, J. F.; Farr, N. T. H.; Sun, Y.; Hughes, G. M.; Cussen, S. A., et al., *Micron* **2022**, *156*, 103234, DOI: 10.1016/j.micron.2022.103234

[122] Homede, E.; Abo Jabal, M.; Manor, O., *Adv. Funct. Mater.* **2020**, *30* (51), 2005486, DOI: 10.1002/adfm.202005486

[123] Garitagoitia Cid, A.; Rosenkranz, R.; Zschech, E., *Adv. Eng. Mater.* **2016**, *18* (2), 185-193, DOI: 10.1002/adem.201500161

[124] Kim, M.; Xin, R.; Earnshaw, J.; Tang, J.; Hill, J. P., et al., *Nat. Protoc.* **2022**, *17* (12), 2990-3027, DOI: 10.1038/s41596-022-00718-2

[125] Bustamante, E. L.; Fernandez, J. L.; Zamaro, J. M., *J. Colloid Interface Sci.* **2014**, *424*, 37-43, DOI: 10.1016/j.jcis.2014.03.014

[126] Schejn, A.; Balan, L.; Falk, V.; Aranda, L.; Medjahdi, G., et al., *CrystEngComm* **2014**, *16* (21), 4493-4500, DOI: 10.1039/c3ce42485e

[127] Lee, Y.-R.; Jang, M.-S.; Cho, H.-Y.; Kwon, H.-J.; Kim, S., et al., *Chem. Eng. J.* **2015**, *271*, 276-280, DOI: 10.1016/j.cej.2015.02.094

[128] Wang, Q.; Ina, T.; Chen, W.-T.; Shang, L.; Sun, F., et al., *Science Bulletin* **2020**, *65* (20), 1743-1751, DOI: 10.1016/j.scib.2020.06.020

[129] Xiao, J.-D.; Wang, Q.-N.; Feng, Z.-D.; Tang, S.; Liu, Y., et al., *J. Catal.* **2022**, *406*, 165-173, DOI: 10.1016/j.jcat.2021.12.033

[130] Wang, B.; Wang, L.; Ding, D.; Zhai, Y.; Wang, F., et al., *Adv. Mater.* **2022**, *34* (50), 2204403, DOI: 10.1002/adma.202204403

[131] Chen, Y.; Xi, B.; Huang, M.; Shi, L.; Huang, S., et al., *Adv. Mater.* **2022**, *34* (7), 2108621, DOI: 10.1002/adma.202108621

[132] Rafie, A.; Pereira, R.; Shamsabadi, A. A.; Kalra, V., *J. Phys. Chem. C* **2022**, *126* (30), 12327-12338, DOI: 10.1021/acs.jpcc.1c09124

[133] Yan, P.; Zhao, W.; McBride, F.; Cai, D.; Dale, J., et al., *Nat. Commun.* **2022**, *13* (1), 4824, DOI: 10.1038/s41467-022-32344-7

[134] Li, L.; Nam, J. S.; Kim, M. S.; Wang, Y.; Jiang, S., et al., *Adv. Energy Mater.* **2023**, *13* (36), 2302139, DOI: 10.1002/aenm.202302139

[135] Chen, P.; Wu, Z.; Guo, T.; Zhou, Y.; Liu, M., et al., *Adv. Mater.* **2021**, *33* (9), 2007549, DOI: 10.1002/adma.202007549

[136] Xu, W.; Lang, S.; Wang, K.; Zeng, R.; Li, H., et al., *Sci. Adv.* **2023**, *9* (33), eadi5108, DOI: 10.1126/sciadv.adi5108

[137] Patel, M. U. M.; Arcon, I.; Aquilanti, G.; Stievano, L.; Mali, G., et al., *Chemphyschem* **2014**, *15* (5), 894-904, DOI: 10.1002/cphc.201300972

[138] Hoefling, A.; Nguyen, D. T.; Partovi-Azar, P.; Sebastiani, D.; Theato, P., et al., *Chem. Mater.* **2018**, *30* (9), 2915-2923, DOI: 10.1021/acs.chemmater.7b05105

[139] Zhang, Y.; Liu, J.; Wang, J.; Zhao, Y.; Luo, D., et al., *Angew. Chem. Int. Ed.* **2021**, *60* (51), 26826-26833, DOI: 10.1002/anie.202108882

[140] Ogihara, N.; Kawauchi, S.; Okuda, C.; Itou, Y.; Takeuchi, Y., et al., *J. Electrochem. Soc.* **2012**, *159* (7), A1034-A1039, DOI: 10.1149/2.057207jes

[141] Waluś, S.; Barchasz, C.; Bouchet, R.; Alloin, F., *Electrochim. Acta.* **2020**, *359*, 136944, DOI: 10.1016/j.electacta.2020.136944

[142] Cañas, N. A.; Hirose, K.; Pascucci, B.; Wagner, N.; Friedrich, K. A., et al., *Electrochim. Acta.* **2013**, *97*, 42-51, DOI: 10.1016/j.electacta.2013.02.101

[143] Peng, H.-J.; Zhang, Q., *Angew. Chem. Int. Ed.* **2015**, *54* (38), 11018-11020, DOI: 10.1002/anie.201505444

[144] Li, S.; Mou, T.; Ren, G.; Warzywoda, J.; Wang, B., et al., *ACS Energy Lett.* **2016**, *1* (2), 481-489, DOI: 10.1021/acsenergylett.6b00182

[145] Jang, P. G.; Suh, K. S.; Park, M.; Kim, J. K.; Kim, W. N., et al., *J. Appl. Polym. Sci.* **2007**, *106* (1), 110-116, DOI: 10.1002/app.26564

[146] Avilés, F.; Cauich-Rodríguez, J. V.; Moo-Tah, L.; May-Pat, A.; Vargas-Coronado, R., *Carbon* **2009**, *47* (13), 2970-2975, DOI: 10.1016/j.carbon.2009.06.044

[147] Mendez-Linan, J. I.; Ortiz-Ortega, E.; Jimenez-Moreno, M. F.; Mendivil-Palma, M. I.; Martínez-Guerra, E., et al., *Carbon* **2020**, *169*, 32-44, DOI: 10.1016/j.carbon.2020.06.085

[148] Zaldivar, R. J.; Nokes, J. P.; Adams, P. M.; Hammoud, K.; Kim, H. I., *Carbon* **2012**, *50* (8), 2966-2975, DOI: 10.1016/j.carbon.2012.02.079

[149] Cao, M.; Fu, A.; Wang, Z.; Liu, J.; Kong, N., et al., *J. Phys. Chem. C* **2014**, *118* (5), 2650-2659, DOI: 10.1021/jp411979x

[150] Guo, Y.; Xu, L.; Liu, H.; Li, Y.; Che, C.-M., et al., *Adv. Mater.* **2015**, *27* (6), 985-1013, DOI: 10.1002/adma.201403846

[151] Huang, L.; Hu, J.; Ji, Y.; Streb, C.; Song, Y.-F., *Chem. Eur. J.* **2015**, *21* (51), 18799-18804, DOI: 10.1002/chem.201501907

[152] Simmons, T. J.; Bult, J.; Hashim, D. P.; Linhardt, R. J.; Ajayan, P. M., *ACS Nano* **2009**, *3* (4), 865-870, DOI: 10.1021/nn800860m

[153] Bauer, M.; Konnerth, P.; Radinger, H.; Pfeifer, K.; Joshi, Y., et al., *Nano Select* **2023**, *4* (4), 278-287, DOI: 10.1002/nano.202200149

[154] Zhang, H.; Fang, Y.; Yang, F.; Liu, X.; Lu, X., *Energy Environ. Sci.* **2020**, *13* (8), 2515-2523, DOI: 10.1039/d0ee01723j

[155] Crawford, A. G.; Dwyer, A. D.; Liu, Z.; Steffen, A.; Beeby, A., et al., *J. Am. Chem. Soc.* **2011**, *133* (34), 13349-13362, DOI: 10.1021/ja2006862

[156] Lu, Q.; Kole, G. K.; Friedrich, A.; Muller-Buschbaum, K.; Liu, Z., et al., *J. Org. Chem.* **2020**, *85* (6), 4256-4266, DOI: 10.1021/acs.joc.9b03421

[157] Zhen, X. V.; Swanson, E. G.; Nelson, J. T.; Zhang, Y.; Su, Q., et al., *ACS Appl. Nano Mater.* **2018**, *1* (6), 2718-2726, DOI: 10.1021/acsanm.8b00420

[158] Niko, Y.; Kawauchi, S.; Otsu, S.; Tokumaru, K.; Konishi, G.-i., *J. Org. Chem.* **2013**, *78* (7), 3196-3207, DOI: 10.1021/jo400128c

[159] Stasyuk, O. A.; Szatylowicz, H.; Krygowski, T. M.; Fonseca Guerra, C., *Phys. Chem. Chem. Phys.* **2016**, *18* (17), 11624-11633, DOI: 10.1039/c5cp07483e

[160] Lin, H.; Zhang, S.; Zhang, T.; Ye, H.; Yao, Q., et al., *Adv. Energy Mater.* **2018**, *8* (30), 1801868, DOI: 10.1002/aenm.201801868

[161] Yan, R.; Zhao, Z.; Zhu, R.; Wu, M.; Liu, X., et al., *Angew. Chem. Int. Ed.* **2024**, *63* (25), e202404019, DOI: 10.1002/anie.202404019

[162] Wang, J.; Zhang, X.; Wang, X.; Liu, J.; Li, S., et al., *Adv. Energy Mater.* **2024**, 2402072, DOI: 10.1002/aenm.202402072

[163] Zhao, Y.; Zhang, J.; Guo, J., *ACS Appl. Mater. Interface.* **2021**, *13* (27), 31749-31755, DOI: 10.1021/acsami.1c08615

[164] Zhang, K.; Li, X.; Yang, Y.; Chen, Z.; Ma, L., et al., *Adv. Funct. Mater.* **2022**, *33* (11), 2212759, DOI: 10.1002/adfm.202212759

Appendix A: Original discharge/charge curves

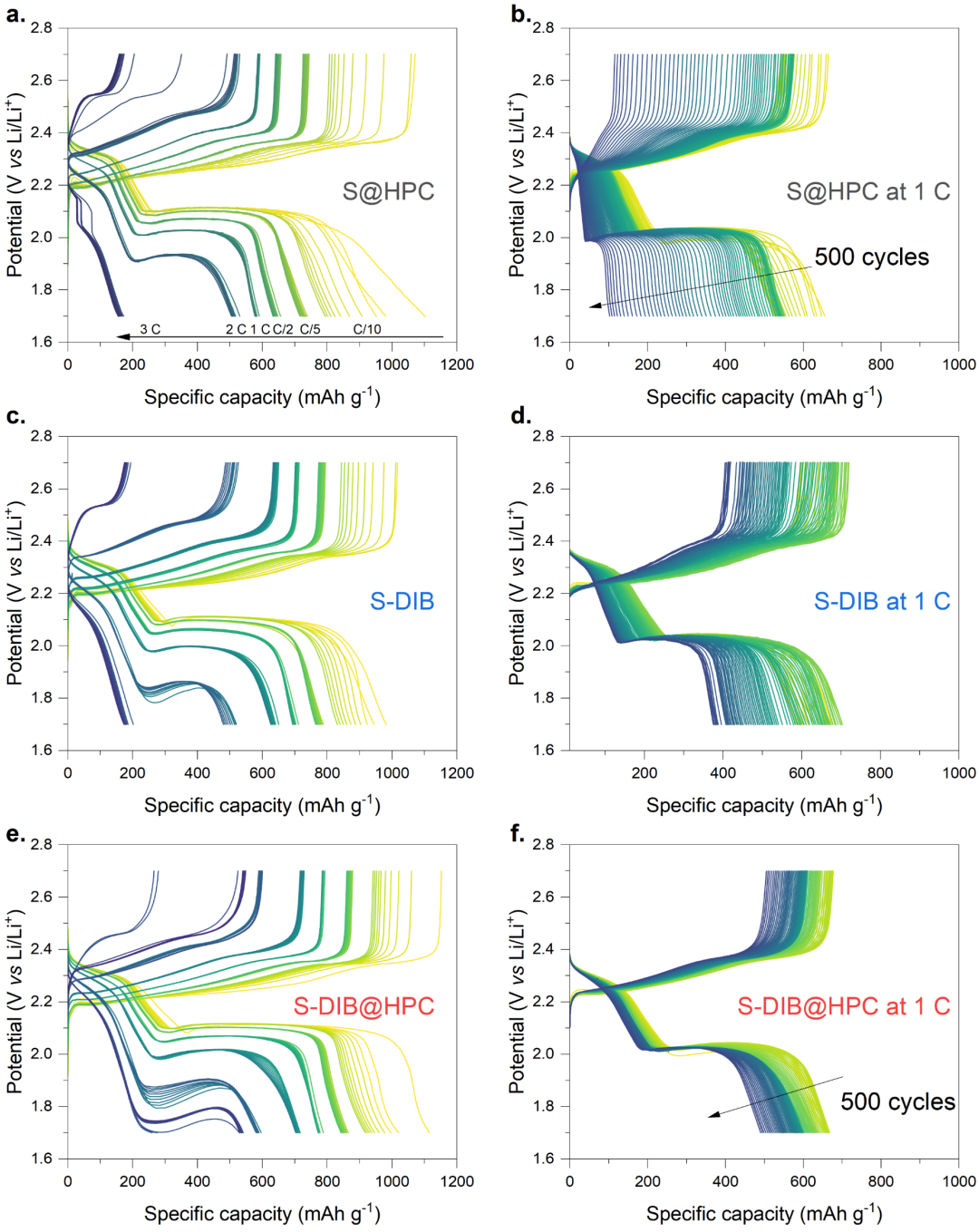

Figure **A1** C-rate and cycling discharge/charge curves of S@HPC, S-DIB and S-DIB@HPC, corresponding to results shown in Figure 3-8 and Figure 3-11.

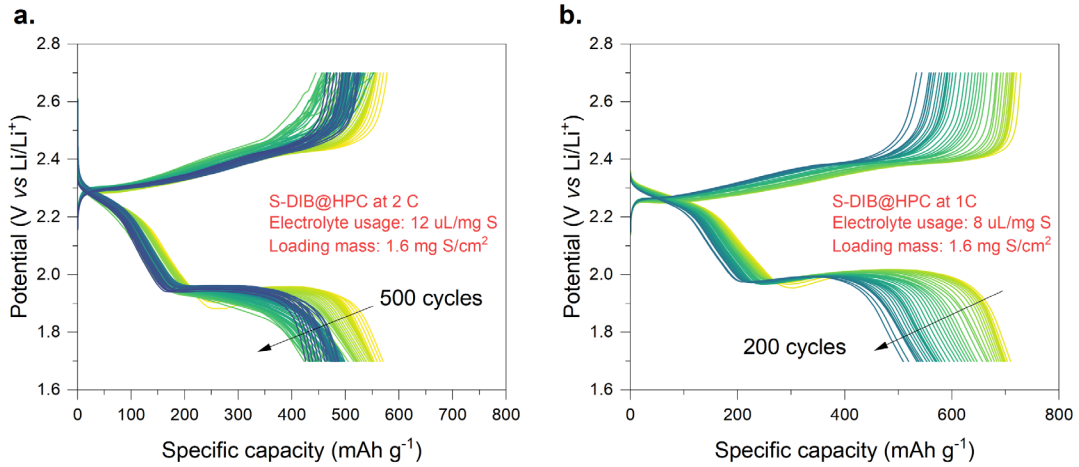

Figure **A2** Cycling discharge/charge curves of S-DIB@HPC, corresponding to results shown in Figure 3-11.

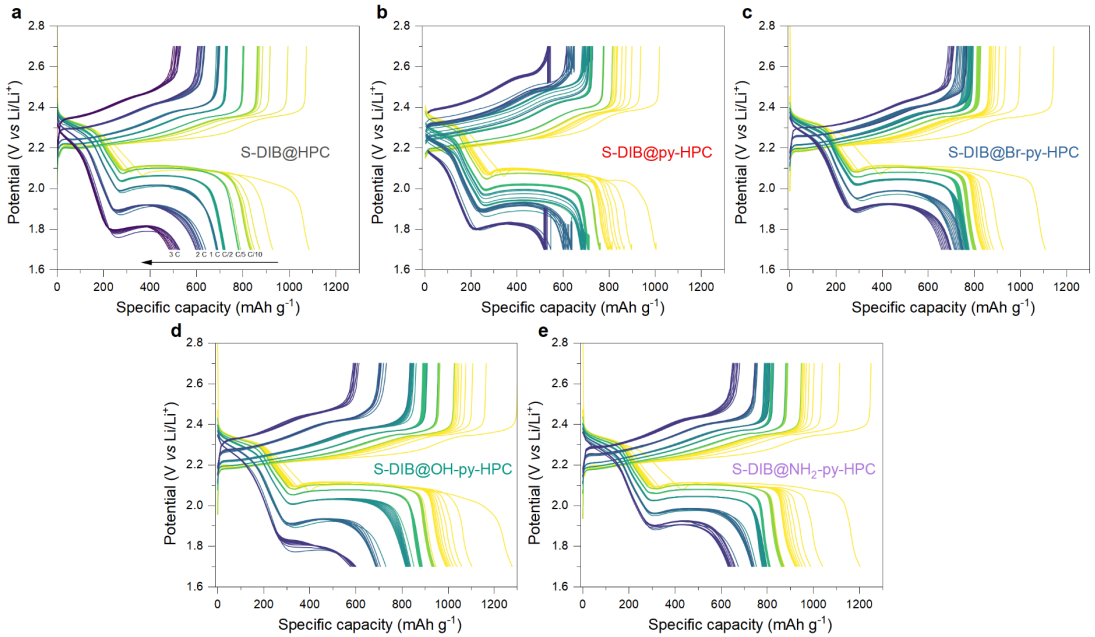

Figure **A3** C-rate discharge/charge curves of S-DIB@HPC, S-DIB@py-HPC, S-DIB@Br-py-HPC, S-DIB@OH-py-HPC, and S-DIB@NH_2-py-HPC, corresponding to results shown in 4-15.

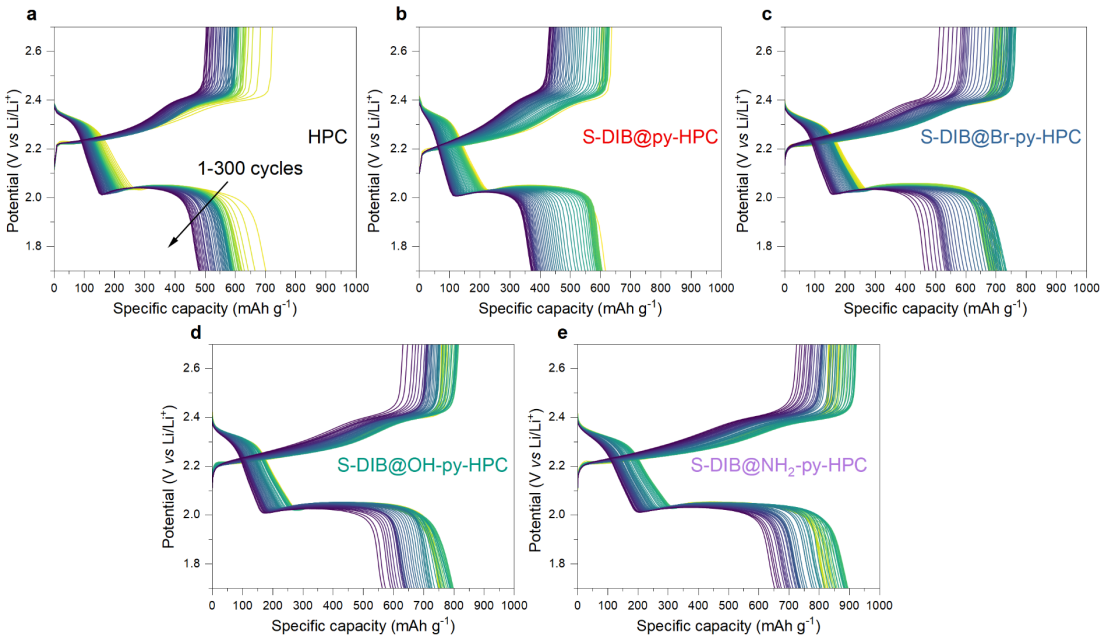

Figure **A4** Cycling discharge/charge curves of S-DIB@HPC, S-DIB@py-HPC, S-DIB@Br-py-HPC, S-DIB@OH-py-HPC, and S-DIB@NH_2-py-HPC, corresponding to results shown in Figure 4-14 and 4-15.

Appendix B: Publications

Publications during PhD study:

B. Deng, F. Scheiba*, A. Zuo, S. Indris, H. Li, H. Radinger, A. Grimm, C. Njel, Sulfur Distribution Analysis in Lithium−Sulfur Cathode via Confined Inverse Vulcanization in Carbon Frameworks., Adv. Energy Mater. 2024, 2402996. DOI: 10.1002/aenm.202402996

B. Deng, F. Scheiba, Pyrene Funtionlized Hollow Porous Carbon/S-DIB Composite as a Cathode for Lithium-Sulfur Batteries., 2024 Meet. Abstr. MA2024-01 808, DOI: 10.1149/MA2024-017808mtgabs

X. Bai, M. Sun, J. Yang, **B. Deng**, K. Yang, B. Huang, W. Hu, X, Pu, Eutectic-electrolyte Enabled Zinc Metal Batteries towards Wide Temperature and Voltage Windows. Energy Environ. Sci. 2024, 17(19), 7330-7341. DOI:10.1039/D4EE02816C

Anlage 5b

Versicherung gemäß § 13 Absatz 2 Satz 2 Ziffer 5 der Promotionsordnung des Karlsruher Instituts für Technologie (KIT) für die KIT-Fakultät für Chemie und Biowissenschaften

1. Einen erheblichen Verstoß gegen die Grundsätze guter wissenschaftlicher Praxis habe ich bislang nicht begangen.

2. Es gab bisher keine Promotionseignungsprüfung oder gleichwertige Prüfung an einer Universität oder dieser gleichgestellten Hochschule, an der ich erfolglos teilgenommen habe.

3. Diesem Promotionsverfahren gingen keine anderen Promotionsverfahren voran und ich bin in keinen weiteren Promotionsverfahren Kandidat/-in.

5. Ein entgeltliches Vertragsverhältnis, das eine gewerbliche Promotionsberatung zum Gegen-stand hat und zur Unselbstständigkeit zumindest einer Promotionsleistung führen kann, besteht bzw. bestand nicht.

6. Die „Regeln zur Sicherung guter wissenschaftlicher Praxis am Karlsruher Institut für Technologie (KIT)“ habe ich beachtet.

7. In die Dissertation wurden Vorveröffentlichungen einbezogen, bei denen ich im Rahmen einer Mitautorenschaft jeweils einen signifikanten Teil selbstständig erbracht habe. Eine Aufstellung mit den Angaben:

Autoren/Autorinnen:

Titel der Vorveröffentlichung:

Veröffentlicht in:

Ausführliche Darlegung des selbstständig erbrachten, signifikanten Beitrages der Vorveröffentlichung oder der zur Veröffentlichung eingereichten Arbeit:

ist dieser Erklärung beigefügt. Die Aufstellung ist Bestandteil dieser Erklärung.

8. Die Dissertation oder Teile davon wurden nicht bei einer anderen Fakultät als Dissertation eingereicht.

9. Die Richtigkeit der vorstehenden Erklärungen bestätige ich.

Ort und Datum Unterschrift

Manuscript 1 (Results and Discussion in Chapter 3)

Authors: Bijian Deng, Frieder Scheiba, Anhao Zuo, Sylvio Indris, Hang Li, Hannes Radinger, Alexander Grimm, Christian Njel

Publication title: Sulfur Distribution Analysis in Lithium−Sulfur Cathode via Confined Inverse Vulcanization in Carbon Frameworks

Published in: Advanced Energy Materials, 2024, DOI: 10.1002/aenm.202402996

The co-authors listed in Table 1 were involved in the implementation and evaluation of some measurements.

Table 1: Statement of co-author contributions

Co-authors	**Contributions**
Frieder Scheiba	Supervise the work
Anhao Zuo	Impedance results simulation
Sylvio Indris and Hang Li	NMR spectroscopy measurements
Hannes Radinger	Polish the manuscript writing
Alexander Grimm	DSC measurements
Christian Njel	XPS measurements

Description of the contribution made independently:

Practical work:

This publication reports on the synthesis of the sulfur-rich polymer/porous carbon composite and explores its electrochemical behaviors. All syntheses were finished by me.

Measurements:

All electrochemical measurements and SEM images were conducted by me. The *operando* Raman spectra were conducted by me. Hang Li and Sylvio Indris carried out the NMR spectroscopy measurement. Alexander Grimm measured DSC. Christian Njel helped obtain XPS results.

Creating the manuscript:

The idea of the publication was conceived after discussing with Frieder Scheiba. The manuscript was written by me and revised by Frieder Scheiba and Hannes Radinger.

Manuscript 2 (Results and Discussion in Chapter4)

Authors: Bijian Deng, Frieder Scheiba, Felix Bauer, Hao Liu, Alexander Grimm

Title: The Funtionlized Pyrene Introduced on Hollow Porous Carbon By π-π Absorption Enables Fast Sulfur Redox Kinetics (To submit)

The co-authors listed in Table 2 were involved in the implementation and evaluation of some measurements.

Table 2: Statement of co-author contributions

Co-authors	**Contributions**
Frieder Scheiba	Supervise the work
Felix Bauer	XPS measurements
Hao Liu	Synchrotron X-ray Diffraction
Alexander Grimm	DSC measurements

Description of the contribution made independently:

Practical work:

This manuscript reports on the synthesis sulfur-rich polymer/pyrene-modified porous carbon composite and explores its electrochemical behaviors. All materials and samples for characterizations were prepared by me and measured by co-authors

Measurements:

All electrochemical measurements and SEM images were conducted by me. The *operando* synchrotron XRD were conducted by Hao Liu. Felix Bauer carried out the XPS measurement. Alexander Grimm measured DSC.

Creating the manuscript:

The idea of the publication was conceived after discussing with Frieder Scheiba. The manuscript was written by me and revised by Frieder Scheiba.

Acknowledgement

First and foremost, I offer my heartfelt thanks to Prof. Helmut Ehrenberg for providing the specialized laboratory conditions and resources essential for my research. Your guidance and support have been instrumental in the completion of this work.

I am also deeply grateful to my group leader, Dr. Frieder Scheiba, for supervising all my experiments, discussing experimental results with me, and helping me improve my English writing. Thank you for organizing weekly group meetings that foster a warm and collaborative atmosphere in group. Your guidance and support have been crucial to my graduation. I would also like to thank my group members, who worked and persevered alongside me: Hannes Radinger, Marina Bauer, Felix Bauer, Marius Ast, Codruta Aurelia Vlaic, and Philip Richter.

I am indebted to Liuda Mereacre for her indispensable assistance with laboratory skills. Without her help, I would not have been able to complete my experiments. My sincere thanks to Udo Geckle for his invaluable technical assistance with the SEM and to Vanessa Trouillet for her kind help with XPS measurements and daily support. I also appreciate Almut Kriese for her exceptional administrative organization.

I would like to thank my colleagues who contributed to my research and friends who supported me in life: Dr. Fabian Jeschull, Cedric Müller, Yury Panasenko, Mattes Renner, Dr. Ramon Zimmermanns, Dr. Arseniy Bokov, Dr. Hang Li, Hao Liu, Anhao Zuo, Kun Tang, and Dr. Jiali Peng.

I would like to express my deepest attitude to Xue Bai. Her love, patience, and understanding have been my constant source of strength. Thank her for believing in me, even when I doubted myself, and for always being there to lift my spirits.

Finally, I am eternally grateful to my parents for their endless love and support. Their guidance, sacrifices, and unwavering belief in my abilities have been the foundation upon which I have built my academic and personal achievements.

Thank you all, once again!

Declaration

Ich versichere hiermit, dass ich die vorliegende Dissertation selbständig und ohne unzulässige fremde Hilfe erbracht habe. Ich habe keine anderen als die angegeben Quellen und Hilfsmittel benutzt, sowie wörtliche und sinngemäße Zitate kenntlich gemacht. Die Dissertation wurde bisher an keiner anderen Hochschule oder Universität eingereicht.

Karlsruhe, den 25. Oct. 2024

M. Sc. Bijian Deng

I hereby declare that I have made this work independently and used no other than the specified sources and tools, as well as, whether verbatim or with regards to content, indicated all citations as such and I have paid attention to the statute of the Karlsruhe Institute of Technology (KIT) in the current version to ensure good scientific practice.

Karlsruhe, den 25. Oct. 2024

M. Sc. Bijian Deng